This is a pre-print version of the article published in: Coordination Chemistry Reviews,

Volume 479, 2023, 215005,ISSN 0010-8545,

https://doi.org/10.1016/j.ccr.2022.215005.

(https://www.sciencedirect.com/science/article/pii/S0010854522006002)

Zirconium Immune-Complexes for PET Molecular Imaging: Current Status and Prospects

Laura Melendez-Alafort[1,*], Guillermina Ferro-Flores[2], Laura De Nardo[3], Blanca Ocampo-García[2] and Cristina Bolzati[4,*]

[1] Immunology and Molecular Oncology Unit, Veneto Institute of Oncology IOV-IRCCS, Via Gattamelata 64, 35138 Padova, Italy.

[2] Department of Radioactive Materials, Instituto Nacional de Investigaciones Nucleares, Ocoyoacac, 52750, Mexico;

[3] Department of Physics and Astronomy, University of Padova, Via Marzolo 8, 35131 Padova, Italy;

[4] Institute of Condensed Matter Chemistry and Technologies for Energy ICMATE-CNR, Corso Stati Uniti, 4, I- 35127 Padova, Italy;

* Correspondence: laura.melendezalafort@iov.veneto.it; cristina.bolzati@cnr.it

Abstract: Diagnostic molecular images, obtained by positron emission tomography (PET), have successfully functioned as sensitive tools for detecting and monitoring the treatment of different diseases, mainly cancer. However, cancer proteomics has shown that the expression of specific molecular targets is dynamic, transforming nuclear molecular imaging techniques from purely diagnostic to procedures aimed at the prognosis of the disease for precise treatment selection. Of all pure PET radionuclides, zirconium-89 is the only one with a sufficient half-life ($t_{1/2}$ = 3.27 d) to be useful for the labeling of antibodies, antibody fragments, cells, and nanoparticles. Therefore, the routine use of ^{89}Zr-immunoPET is expected to help determine the prognosis and benefit of immunotherapies in cancer patients, such as anti-FAP, anti-CD44, anti-VEGF, anti-EGFR, anti-TGF-β, anti-PSMA, anti-STEAP1, anti-HER2/3, and/or anti-PD-L1. For this purpose, the stable coordination of zirconium to bifunctional chelators is essential to form efficient radioimmunoconjugates with molecular targeting capabilities, which, combined with high PET resolution and sensitivity, could offer the most advanced tool for cancer prognosis, treatment definition and follow-up. In this manuscript, recent achievements concerning the coordination chemistry of zirconium (IV) to different chelators, the different molecular targets identified using immunoPET, the drug delivery systems based on ^{89}Zr-antibody-drug conjugates/nanoparticles, and cell tracking with ^{89}Zr, are reviewed and discussed.

Keywords: zirconium-89; radiochemistry; bifuncional chelator; immunoPET; Nanoparticles, Cell traking.

Summary

1. Introduction

2. Physical Characteristics of ^{89}Zr

3. Production methods

4. Coordination Chemistry of ^{89}Zr

4.1. Fundamentals

4.2. Zirconium(IV) Chelators

4.2.1 Polyazacarboxylate chelators

4.2.2 Hydroxamate-based DFO analogs

4.2.3 Other hydroxamate derivatives

4.2.4 Hyroxypyridinone (HOPO)-based Chelators

4.3. Radiosynthesis

5. ^{89}Zr-ImmunoPET studies

5.1. HER2 targeting

5.2. EGFR targeting

5.3. HER3 targeting

5.4. VEGF targeting

5.5. CD20 targeting

5.6. CD44 targeting

5.7. TGF-β targeting

5.8. PSMA targeting

5.9. STEAP1 targeting

5.10. Mesothelin targeting

5.11. PD-1 and PD-L1 targeting

5.12. CA19-9 targeting

5.13. CAIX targeting

5.14. FAP targeting

6. Antibody-drug conjugates

7. ^{89}Zr-nanoparticles

8. Cell tracking with ^{89}Zr

8.1. Labeling of non-genetic engineering cells

8.2. Labeling of genetic engineering cells

9. Perspectives and conclusions

1. Introduction

Non-invasive molecular imaging has become a useful and essential tool to assist the physicians in the diagnosis and management of some diseases [1, 2]. Two techniques are used to achieve nuclear molecular

imaging, single-photon emission computed tomography (SPECT) and positron emission tomography (PET). Both procedures offer good sensitivity at the nanomolar scale, without any depth limit in soft tissues [3]. However, in clinical practice, it is preferred to use PET over SPECT, whenever possible, due to its greater sensitivity, which provides images with higher resolution and contrast [4].

The development of hybrid PET/CT scanners and the increasing availability of radionuclides, such as ^{11}C, ^{13}N, ^{15}O, ^{18}F and ^{68}Ga, have driven the use of PET images for cancer diagnosis in the last 20 years [5]. Nevertheless, the short half-life of all these radionuclides limits the use of PET imaging to small molecules with rapid metabolism and makes radiolabeling protocols challenging [6]. To label large biological molecules with a slow biodistribution profile, such as monoclonal antibodies (mAbs), cells or multifunctional drug delivery systems, it is necessary to use radionuclides with a longer half-life that matches the time required for these molecules to reach targets useful for PET imaging [7, 8].^{89}Zr has been considered the best radionuclide to study these large biomolecules, due to its half-life ($t_{1/2}$ = 3.27 d) and low positron energy [9, 10], which is why more than 700 papers, reporting macromolecules or cells labeled with ^{89}Zr, have been published in the last 15 years.

The purpose of this paper is to summarize recent achievements in ^{89}Zr-radiochemistry and imaging research. The works including the radionuclide production, the development of bifunctional chelators for $^{89}Zr^{4+}$ and their coordination chemistry with respect to the stability properties and pharmacokinetics of chelates, are also revised and discussed. Moreover, attention was paid to the different trends in the field embracing ^{89}Zr-immunoPET imaging and ^{89}Zr-based imaging, which exploit delivery systems other than antibodies such as nanoparticles and live cells.

2. Physical Characteristics of ^{89}Zr

^{89}Zr decays by positron emission (23%) and electron capture (77%) to ^{89m}Y ($t_{1/2}$ = 16 s), which de-excites through the emission of a high-energy γ-ray (909 keV), and the rest to several excited levels of ^{89}Y, followed by emission of photons , and into the same metastable level ^{89m}Y. The ^{89}Zr β^+ energy values (maximum/average 902/396 keV) are intermediate, between those of low-energy β^+ emitters, such as ^{18}F and ^{64}Cu (maximum/average energy 633/250 keV and 653/217 keV, respectively), and those of high energy, such as ^{86}Y, ^{124}I, ^{68}Ga and ^{44}Sc (maximum/average energy 3141/665, 2138/819, 1900/829 and 1474/631 keV, respectively) (Figure 1) [11].Therefore, compared to other β^+-emitter radionuclides with similar half-life, such as ^{86}Y ($t_{1/2}$ = 14.74 h) and ^{124}I ($t_{1/2}$ = 4.1760 d), ^{89}Zr allows PET imaging with better spatial resolution, being the intrinsic spatial resolution loss of the order of 1.0 mm, comparable to that of ^{18}F (0.7 mm) [12]. Moreover, both ^{86}Y and ^{124}I emit prompt gamma rays, which coincide with positron decay, causing spurious coincidences, blurring the PET image, and producing quantification errors. The 909-keV γ-ray from ^{89}Zr decay, besides having an energy far from the annihilation peak, does not coincide with the PET signal, emitted due to the de-excitation of ^{89m}Y, which is characterized by a long half-life (16 s), compared to the typical coincidence timing window of PET systems. Consequently, ^{89}Zr can be classified as a pure PET radioisotope, as in the case of ^{11}C, ^{13}N, ^{15}O and ^{18}F [13] and allows the acquisition of high-resolution PET images [14].

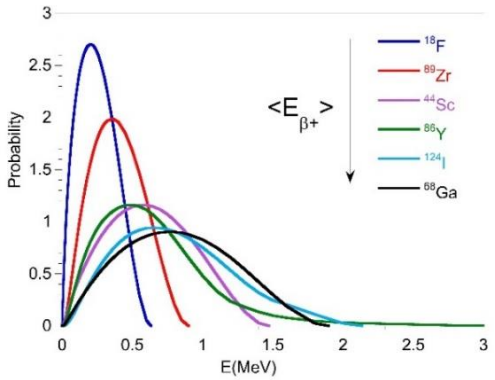

Figure 1. Energy distribution of positrons emitted by different radionuclides, normalized to one β^+ particle.

The low branching ratio for the β^+ decay of ^{89}Zr is the same as that of ^{124}I (23%) and slightly lower than that of ^{86}Y (32%), as can be seen in the decay schemes displayed in Figure 2. Although the presence of the γ-ray at 909 keV affects the absorbed dose, limiting the amount of activity that can be administered to patients, the total energy emitted per decay (1.26 MeV/nt) is lower than ^{124}I (1.3075 MeV/nt) and ^{86}Y (3.7956 MeV/nt). However, while ^{86}Y and ^{124}I can already be used in tandem with radiotherapeutic agents such as ^{90}Y and ^{131}I, for personalized treatment planning or real-time therapy monitoring (theranostics), the possible therapeutic counterparts of ^{89}Zr, such as the β-emitters ^{97}Zr ($t_{1/2}$ ~ 16.74 h) and ^{95}Zr ($t_{1/2}$ ~ 64.0 d), have not yet been explored.

3. Production methods

Recently, the International Atomic Energy Agency (IAEA) started a Coordinated Research Project focused on "Production of ^{89}Zirconium and the Development of ^{89}Zr-Radiopharmaceuticals", with the main objective of improving the ^{89}Zr production steps (target design and manufacturing, separation and purification methods), quality control protocols and radiopharmaceutical development [15].

Different nuclear reactions involving proton (p), deuteron (d), alpha (α) and neutron (n) impacts on ^{89}Y (p or d), ^{nat}Sr (α), and ^{90}Zr (n), respectively, have been suggested for ^{89}Zr production. The α energy range suitable to produce ^{89}Zr through ^{nat}Sr irradiation appears to be 20-8.5 MeV because it gives 0.9 MBq/μA·h as integral yield, and limits the co-production of radionuclide impurities [16]. Radionuclidic impurities produced in this energy range, by the end of irradiation, will be ^{88}Zr (0.56%) and ^{86}Zr (0.73%). However, due to the different half-lives of the two radioisotopes, while the contribution of ^{86}Zr ($t_{1/2}$=16.5 h) will rapidly decrease with post-irradiation time, that of ^{88}Zr ($t_{1/2}$=2001 h, decaying to ^{88}Y, $t_{1/2}$=2544 h) will increase, reaching levels too high for medical application. To better exploit the ^{nat}Sr(α,xn)^{89}Zr excitation function, the energy range 47-35 MeV has also been evaluated by theoretical calculations, providing an estimated yield of about 15 MBq/μAh, but also demonstrating a non-negligible production of isotopic impurities [17].

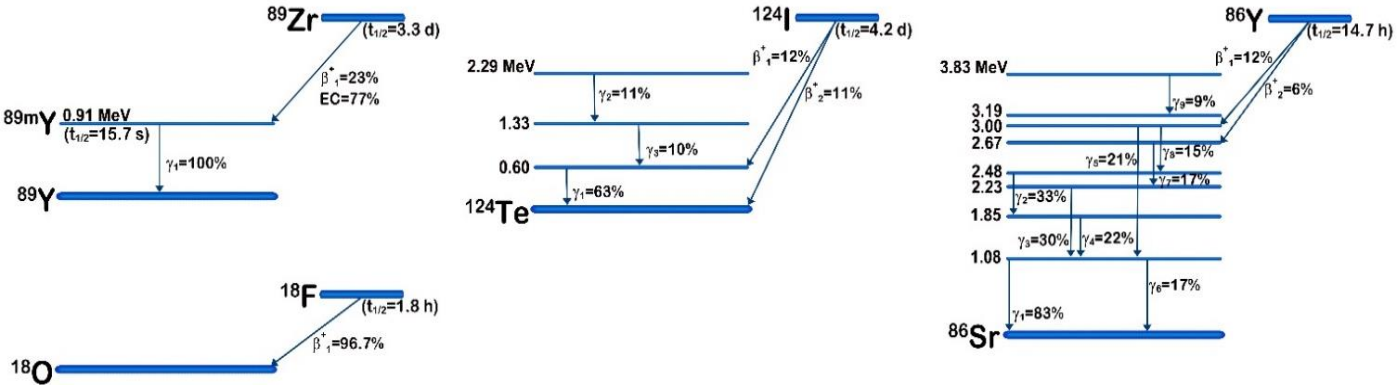

Figure 2. Simplified radioactive decay schemes for ^{89}Zr, ^{18}F, ^{124}I and ^{86}Y. Only radiations with an abundance higher than 5% were considered.

The ^{90}Zr(n,2n)^{89}Zr reaction also appears not suitable for medical application, since the maximum cross-section occurs at about 20 MeV, but the high-energy neutron beam intensity, obtained as secondary particles, will be low, producing ^{89}Zr with low specific activity [17].

Because of the higher rate of production with a lower level of impurities and a lower energy beam requirement, ^{89}Zr is usually obtained using accelerators, via the bombardment with deuterons or protons of ^{89}Y, i.e., ^{89}Y(p,n)^{89}Zr and ^{89}Y(d,2n)^{89}Zr. One of the main advantages of these production routes is that, being 100% the natural isotopic abundance of ^{89}Y, the yttrium target preparation and post-irradiation processing could be performed by avoiding complicated and expensive enrichment operations and recycling processes. Experimental data concerning both reactions [^{89}Y(d,2n)^{89}Zr and ^{89}Y(p,n)^{89}Zr] have been evaluated by the IAEA, under a Coordinated Research Project (CRP) [18]. The selected and recommended cross sections are available on the IAEA website [19]. A different evaluation procedure of the same reactions was also performed by Amjed *et al*. [20], including an estimation of the level of the^{88}Zr impurity.

The ^{89}Y(p,n)^{89}Zr nuclear reaction has a threshold at about 4 MeV and there is a broad peak in the energy range 11-16 MeV. As the threshold energy values for the formation of radioactive impurity ^{88}Zr occurs at about 13 MeV [21, 22], and the best proton energy for maximum yield is in the range of 14-9 MeV with limited radioisotopic contaminants, available to a large number of medical cyclotrons. The calculated integral yield in this energy range is 58 MBq/μA·h, according to Omara *et al*. [22], while Amjed *et al*. [20] estimated 63 MBq/μA·h with a 0.36% contribution of the radioisotopic impurity ^{88}Zr. The same authors evaluated an integral yield of 50.4 MBq/μAh, in the energy range of 13-9 MeV, where 100% pure ^{89}Zr would be obtained.

The threshold energy for the ^{89}Y(*d*,2n)^{89}Zr reaction is about 6 MeV, while to produce the long-lived ^{88}Zr, formed by the ^{89}Y(*d*,3n) channel, the energy is of 15.5 MeV [23]. According to Amjed *et al*., pure ^{89}Zr can be obtained with a yield of 74 MBq/μAh for a *d* energy of 17 MeV and the yield can be increased up to 122 MBq/μAh in the energy window of 30-17 MeV, but with 3% of ^{88}Zr impurity [20]. The 67-MBq/μAh yield obtained by Zweit *et al.* [24], in high-current production runs. performed over the d energy range of 16-7 MeV, agrees with the theoretical value, while the experimental yield of 58±5 MBq/μAh, obtained at 13 MeV deuterons by Tang *et al.*[25].

Analyzing the results of the two production routes, the production rate of ^{89}Zr, by proton beam, is expected to be higher than that by deuteron beam, in the low-energy region, but lower beyond 22 MeV [20]. The $^{89}Y(p,n)^{89}Zr$ reaction is therefore the method of choice for low-energy medical cyclotrons, while the use of deuteron beams could provide an advantage in terms of activity production if high-energy cyclotrons are available.

The high-current p irradiation of yttrium solid targets has already been extensively employed to produce ^{89}Zr in GBq amounts, with practical yields slightly lower than the theoretical values, as expected, since medical cyclotrons use liquid and gaseous targets; nowadays, some attempts are underway to produce ^{89}Zr through liquid targets. Yttrium solid targets have been prepared using foils, pressed powders, electrodeposition and sputtered material [26]. Among the most common solid target preparation methods, Y foils are largely adopted due to their ease of use, despite the superior heat transfer characteristics of sputtered Y targets [27, 28], allowing higher beam current irradiations. As sputtered targets also suffer from high cost and standardization issues, an alternative type of cyclotron solid target has recently been developed by tightly binding a metallic Y disc with a niobium backing plate, using the Spark Plasma Sintering (SPS) technique [29]. Despite the production yields and the radioimpurity profile of the final ^{89}Zr obtained after the dissolution and purification processes of SPS-made targets, these were comparable to foil target results; the former having the advantage of easier processing and handling for purification steps post-irradiation. Besides, no damage was observed on the SPS-made targets, even after irradiation at 60 μA, suggesting the possibility of manufacturing thicker targets, capable of withstanding higher proton current irradiation, in order to increase the radionuclide yield.

Liquid targets provide advantages in terms of target processing and cost [30, 31], but the obtained yield of ^{89}Zr is lower compared to solid targets, although both the yield and purity are sufficient for local use [32]. The use of liquid targets for radiometal production causes extremely high in-target pressure, even at low beam current, caused by the formation of H_2 and O_2 gases, due to the radiolysis of water. The effects of solution composition on in-target chemistry during ^{89}Zr production, from natural, isotopically-pure ^{89}Y salts, have been studied [33] and ^{89}Zr production conditions and purification methods using liquid targets have been summarized by Pandey *et al*. [31].

An alternative method of producing ^{89}Zr, via photonuclear reactions using 55-MeV bremsstrahlung irradiation from natural niobium and natural molybdenum samples, was also proposed [34]. Produced yields are significantly lower than the $^{89}Y(p,n)^{89}Zr$ reaction yield, but with an insignificant contribution to total activity due to the ^{88}Zr impurity.

4 Coordination Chemistry of ^{89}Zr

4.1. Fundamentals

Zirconium is a group 4 transition metal with a wide range of applications, including nuclear medicine. In aqueous solutions, zirconium exists mainly in the +4 oxidation state, although less common oxidation states (+1, +2, +3) have also been reported. The Zr^{+4} cation, with its $[Kr]4d^0$ electronic configuration, is a highly

charged ion that forms complexes with variable coordination geometries and coordination numbers (CN), ranging from 4 to 12, although complexes with high CN are ideal [35, 36]. Zr^{+4} usually forms six- and octa-coordinated complexes; the latter, with dodecahedral or square antiprismatic geometries. Coordination species with lower CN usually need additional ligands to reach an octa-coordinated environment, making the metal complex vulnerable to hydrolysis and polymerization reactions [36], thus forming polynuclear entities (e.g., dimers, trimers and tetramers) that are joined by hydroxo- or oxo-donor groups [35].

Due to its high charge and small ionic size, Zr^{+4} is considered a hard Lewis acid, with a strong affinity for hard Lewis bases that contain anionic oxygen or nitrogen donors, and very occasionally with sulfur donors [37]. Therefore, polydentate ligands, characterized by anionic oxygen donors, are preferred.

As for all radiometal-based targeting agents, a suitable BFCA must be carefully chosen to attach the ^{89}Zr radioisotope to the targeting molecule. A large number of articles and comprehensive reviews focused on the design and synthesis of high-affinity zirconium chelators for antibody coupling have been reported [6, 38-42]. Of note, many of the proposed chelators were initially investigated for the complexation with other trivalent radiometal ions or as actinide sequestration agents.

Either way, the thermodynamic stability and kinetic inertness of the metal-chelator complex are among the most important factors that must be considered as they determine the selectivity of the metal toward the chelator and consequently its potential application in the radiopharmaceutical field. Above all, the kinetic stability of the coordination complex with regard to the loss of the metal ion from the chelator is deemed the main factor that affects the *in vivo* pharmacokinetics of a radiolabeled compound. Other important aspects that contribute to stability and selectivity toward specific metal-ion chelation *in vivo* are coordination number, redox stability, protonation constants, counterion bounding, transchelation of radiometal to metal-bounding proteins, and metabolic stability. Specific enzyme-mediated reactions must also be considered because they can alter the chemical structure of the complex, resulting in a reduction in its kinetic and thermodynamic stability.

For optimal stability, the coordinating atoms of the ligand should embrace the geometry enforced by the metal, fulfilling the requirements of metal coordination thus preventing the challenge from extraneous ligands [43]. Therefore, octa-coordinating chelators are preferred over six-coordinating ones (*vide infra*). Stable coordination of radioactive $^{89}Zr^{4+}$ in an aqueous milieu is also of crucial importance when developing ^{89}Zr-tagged proteins.

4.2. Zirconium(IV) Chelators

Structures of the most commonly used high-denticity acyclic and cyclic ^{89}Zr chelators, along with their coordinating atom sets, are shown in the following subsections. In principle, such ligands are particularly effective in generating robust complexes because of their high-denticity (chelate effect). When a preorganized binding pocket is offered, the entropic cost of complexation may be readily accessible with a raised effect on the inertness of the metal complex. This effect is particularly evident for macrocyclic chelators, although their rigid structure makes them more kinetically inert compared to their acyclic

counterpart, thus high ligand amounts, extended reaction time, and heating are necessary for optimal radiochemical yield. In contrast, acyclic chelators can be rapidly radiolabeled even at room temperature (RT) because of the high bound rotation freedom in their free form. The outcome of such freedom is the high entropic cost of complexation that leads to reduced stability with respect to macrocycles.

4.2.1 Polyazacarboxylate chelators. The structures of acyclic and cyclic ^{89}Zr polyazacarboxylate chelators used in radiopharmaceutical applications are shown in Figure 3.

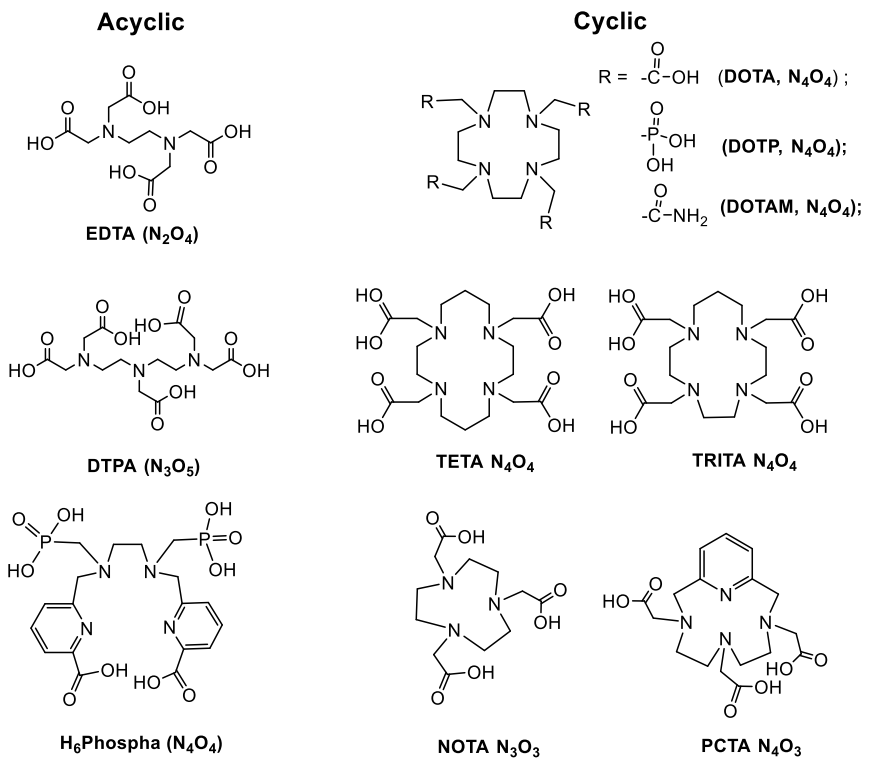

Figure 3. Structures of acyclic and cyclic ^{89}Zr polyazacarboxylate chelators used in radiopharmaceutical applications.

Zr^{+4} strongly prefers polyanionic hard donor chelators, as proved by the stability constants of its complexes with the acyclic polyazacarboxylate chelators EDTA and DTPA (log K_{ML} = 27.7, 29.4 and 35.8, 36.9 respectively). X-ray data of both complexes displayed a total coordination number of 8 in a dodecahedron arrangement (Figure 4).

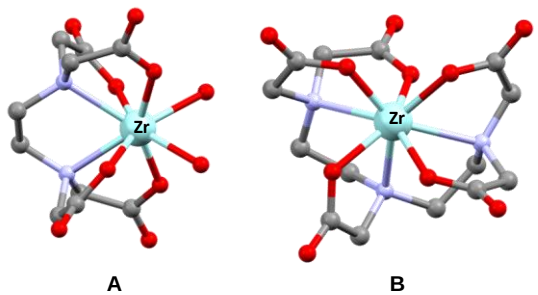

Figure 4. Crystal structures of Zr-EDTA (A) and Zr-DTPA (B)

Specifically, the geometry of Zr-EDTA is a distorted dodecahedron composed of the N_2O_4 six-dentate chelator (two nitrogen atoms of ethylenediamine and four oxygen atoms of the carboxyl groups) and two oxygen-bound water molecules to complete the metal coordination sphere [44]. DTPA is fully octa-dentate (N_3O_5) in its Zr^{+4} embracing [45]. However, EDTA and DTPA were not very successful in chelating $^{89}Zr^{+4}$; unstable radiocompounds with negligible radiochemical yield (RCY) were obtained.

Orvig *et al.* investigated another series of acyclic polyazacarboxylate chelators to which H_6Phospha belongs (Figure 3) [42]. Radiolabeling of H_6phospa-trastuzumab with $^{89}Zr^{+4}$ in phosphate buffered saline (PBS; pH 7.4) revealed poor radiometal incorporation (<12%) even after 18 h of incubation at both RT and 37 °C.

Tetraazamacrocycles, such as DOTA and its derivatives, were also tested as Zr^{+4} chelators. DOTA is an N_4O_4 octa-dentate ligand, so in principle it does not fit well with the high oxophilic demand of the hard Zr^{+4} ion. Despite the initial observation of the failure to form stable Zr^{+4} complexes, recent studies by Pandya *et al.* clearly proved the ability of DOTA and its two derivatives (DOTP, which contains phosphonate pendant groups and DOTAM comprising hydroxamate pendant groups) (Figure 3) to produce very stable ^{89}Zr-labeled compounds with high yield [46]. X-ray diffraction data of Zr-DOTA complex show a compressed square antiprismatic geometry, all four nitrogen atoms of the macrocycle and the acetate pendant groups contribute to Zr^{4+} coordination to meet the requirement of an octa-coordinated complex. The structure in Figure 5 displays that the metal is completely caged in the DOTA scaffold; this could be the key for the relation between the structure of the complex and its unexpected performance both *in vitro* and *in vivo.*

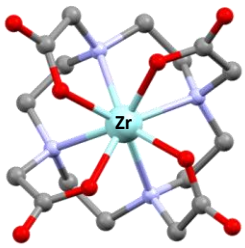

Figure 5. Crystal structure of Zr-DOTA

Compared to acyclic ligands, these macrocycles required heating at 90 °C for a prolonged reaction time to give the radiocomplexes in satisfactory yields. This demand represents an important limitation in the context of labeling temperature-sensitive molecules. Radioactive analogs prepared using standard procedures based on ^{89}Zr-oxalate precursor resulted in low radiochemical yields, probably because of the competition between the macrocycle ligand and the oxalates in solution. In contrast, the usage of $^{89}ZrCl_4$ as the starting material allowed quantitative complexation of the chelators, suggesting that differences in reactivity are probably determined by the ^{89}Zr-species present in solution. $^{89}ZrCl_4$ readily undergoes aquation in solution to generate multiple μ-hydroxo-and μ-oxo-bridged species. However, when $^{89}ZrCl_4$ is mixed with a buffered solution of the macrocycle, in the absence of a competing oxalate ligand, the formation of the ^{89}Zr-complex is favored over the formation of ^{89}Zr-OH species.

Notably, comprehensive stability studies of these ^{89}Zr-DOTA-based complexes demonstrated their remarkable stability, which outperformed all competitors, including the gold standard DFO. On the basis of

EDTA challenge studies, the order of the complexes stability is ^{89}Zr-DOTA >> ^{89}Zr-DOTP > ^{89}Zr-DOTAM > ^{89}Zr-DFO. However, the elevated temperature needed for complexation ^{89}Zr-DOTA is an important limitation for immunoPET applications.

Lately, Pandya *et al.* also described the synthesis and complete characterization of four Zr-complex with polyazamacrocycle chelators: Zr-TETA (TETA= 1,4,8,11-tetraazacyclotetradecane-1,4,8,11-tetraacetic acid), Zr-TRITA (TRITA= 2,2′,2″,2‴-(1,4,7,10-tetraazacyclotridecane-1,4,7,10-tetrayl) tetraacetic acid)), Zr-PCTA (PCTA=3,6,9,15-tetraazabicyclo[9.3.1]pentadeca-1(15),11,13-triene-3,6,9-triacetic acid), and Zr-NOTA (NOTA= 2,2’,2”-(triazacyclononane-1,4,7-triyl)-triacetic acid) (Figure 3) [47]. The crystal structure of Zr-chelates resulting from the TRITA, PCTA, and NOTA ligands has also been reported. X-ray analysis data give a further indication that Zr^{4+} prefers an octa-coordinated ligand environment. In fact, when the chelator is unable to provide eight coordinating units, binuclear complexes are formed to saturate the metal coordination sphere (Figure 6).

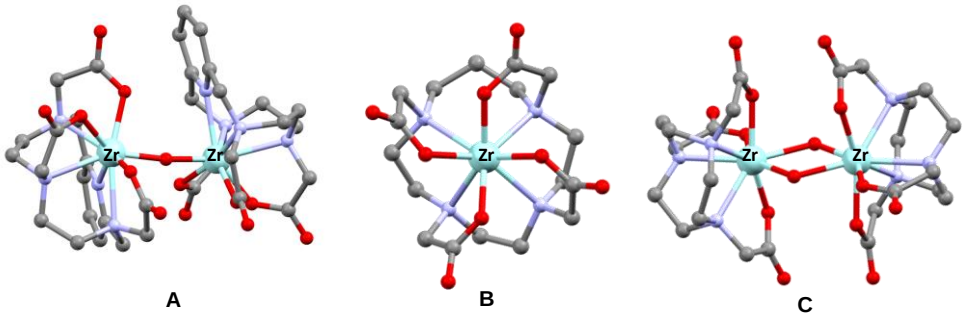

Figure 6. Crystal structure of Zr-TRITA (A), Zr-PCTA (B), and Zr-NOTA (C)

$^{89}ZrCl_4$ was used as a precursor for the radiosynthesis of the Zr-complex with polyazamacrocycle chelators, the labeling conditions are reported in the following. ^{89}Zr-PCTA and ^{89}Zr-NOTA were quantitatively obtained under mild conditions (60 min 37 °C), showing robust stability *in vitro* and *in vivo* behavior. In contrast, ^{89}Zr-TRITA was achieved only under forcing conditions (120 min 99 °C), and revealed poor stability. The preparation of ^{89}Zr-TETA could not be accomplished, despite repeated attempts using conventional and microwave-assisted strategies.

Imaging studies of ^{89}Zr-PCTA and ^{89}Zr-NOTA in healthy mice revealed that both compounds presented rapid distribution and clearance from the blood and liver within the first 60 min, as well as rapid renal excretion. Considering that polyazamacrocycles can chelate a range of radionuclides for imaging and therapy, the authors concluded that their utilization in immunoPET imaging may lead to new strategies for developing theranostic agents [47].

*4.2.2 Hydroxamate-based DFO analogs***.** Deferoxamine B (DFO) is a hexadentate acyclic siderophore that contains three hydroxamic acid groups suitable for metal coordination and a terminal primary amine group, which is useful as an anchor site for biomolecule conjugation (Figure 7). The rationale for the use of this chelator for Zr^{4+} lies in the preference of the metal for hard anionic donor groups and its ability to coordinate monohydroxamate ligands. Currently, DFO is the most widely used chelator for ^{89}Zr-immunoPET. Methods used for random and site-specific bioconjugation of DFO-based BFCA to antibodies and their derivatives

have been fully described in two recent reviews [41, 48]. Despite its wide use, which makes it the gold standard for ^{89}Zr-immunoPET, this ligand cannot completely satisfy the eight coordination sites of Zr^{4+} because it is a hexadentate chelator. Several reports have demonstrated insufficient *in vivo* stability of ^{89}Zr-DFO bioconjugates, because radiometal dissociation of Zr-DFO leads to the accumulation of free ^{89}Zr in bone (ID/g 10-15% at 6 d *p.i.*).

There is no crystal structure of Zr-DFO, although density functional theory (DFT) studies predicted that the metal is coordinated with the three hydroxamate groups of DFO and that the metal coordination sphere is completed by two hydroxide ligands $[Zr(DFO)(OH)_2]$ rather than two water molecules $[Zr(DFO)(OH_2)_2]^{2+}$ [49-51]. Consequently, the highly oxophilic Zr^{4+}cation is stabilized by the coordination of eight oxygen atoms. These results stimulated the rapid development of a series of high-denticity chelators based on DFO. The first, an octadentate chelator with four hydroxamic acid groups, named DFO* (Figure 7) was prepared by Patra *et al.* [52]. The eight oxygen donor atoms are intrinsically present in the DFO* structure; therefore, it can accommodate the metal to give an octa-coordinated complex according to DFT calculations.

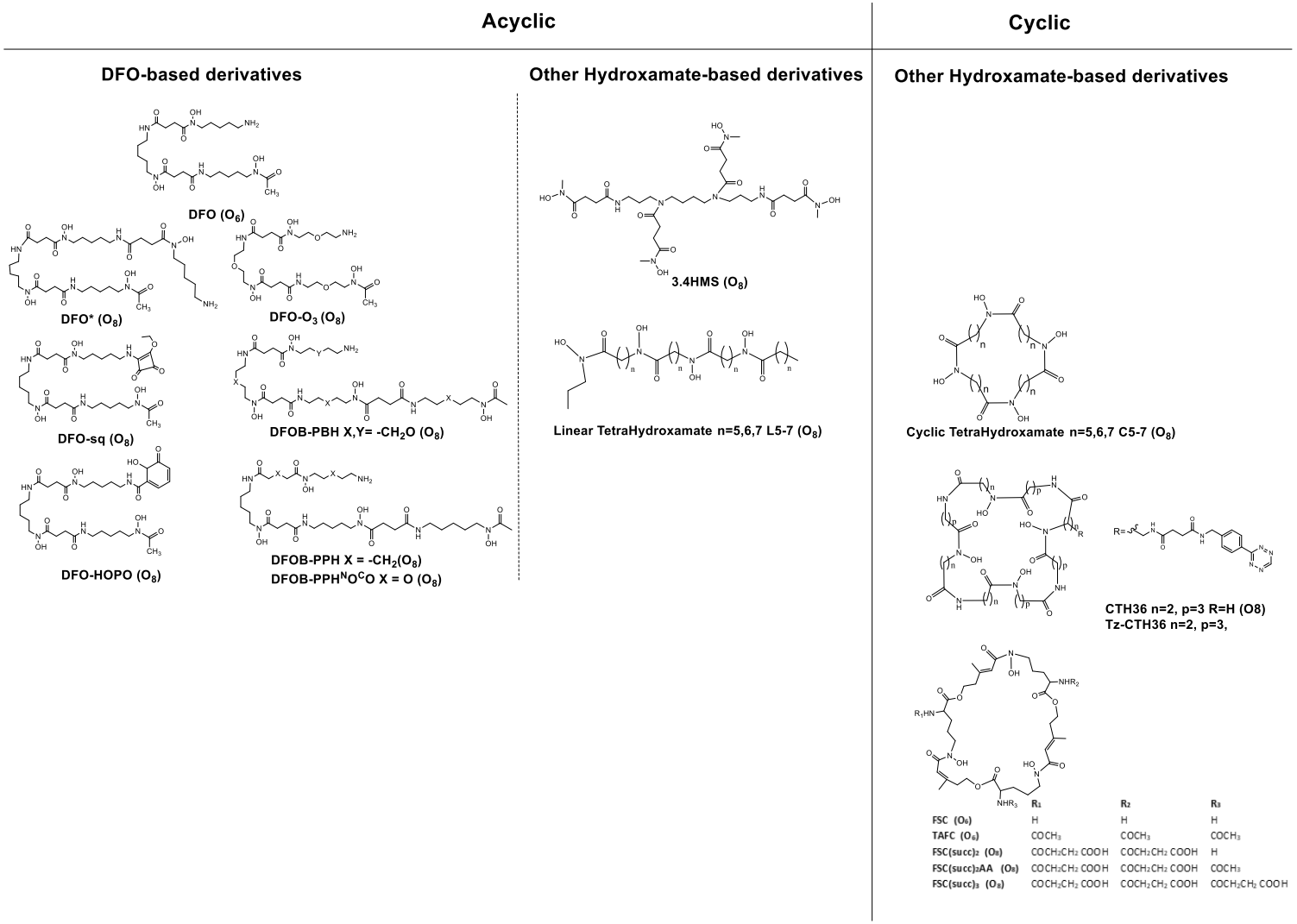

Figure 7. Structures of acyclic and cyclic ^{89}Zr Polyazacarboxylate chelators used in radiopharmaceutical applications

^{89}Zr-DFO* was accessible in high yield under mild reaction conditions within 2 h of incubation at RT and exhibited inertness to transchelation when challenged with DFO, as well as superior *in vivo* properties. ^{89}Zr-DFO* showed lower uptake in bone, liver, and spleen 6 d p.i. than DFO. Recently, Cho *et al.* conjugated DFO* and DFO to the human IgG (hIgG) and to the antibody-drug conjugate trastuzumab-emtansine (T-DM1) to compare the *in vitro* stability and the *in vivo* PET imaging of both chelators after ^{89}Zr-labeling [53]. All complexes were obtained with high radiochemical purity (RCP; in the range 90-91%). ^{89}Zr-DFO*-hIgG was stable in human plasma or under challenge reactions with EDTA (0.1 mM), while challenge with DFO (0.1 mM) produced a loss of ^{89}Zr (26 %) after 5 d. In contrast challenge of ^{89}Zr-DFO-hIgG with DFO* (0.1 mM) brought up to 77% of ^{89}Zr release after 5 d. ^{89}Zr-DFO*-T-DM1 maintained high affinity for HER2 receptors present in SK-BR-3 (Kd = 2.2 nM) and SK-OV-3 (Kd =1.9 nM) cells. Biodistribution studies of ^{89}Zr-DFO*-T-DM1 in mice showed significantly lower uptake in non-target tissues such as bone, liver, kidneys, and spleen than those of ^{89}Zr-DFO-T-DM1. The uptake of ^{89}Zr-DFO*-T-DM1 and ^{89}Zr-DFO-T-DM1 in SK-OV-3 tumors was moderate (5.0 %ID/g and 6.3 %ID/g, respectively). Therefore, the author concluded that the conjugation of DFO* to T-DM1 provides a more stable chelation of ^{89}Zr and, consequently, better imaging properties [53].

The DFO* scaffold was modified with oxygen atoms by the Codd and Gasser groups [54-56].The Cood group used cultures of Streptomyces pilosus to develop a bioengineering route to synthesize the DFO derivative with three oxygen atoms in its backbone, DFO-O3 (Figure 7) [54]. DFO-O3 backbone was then chemically extended with an additional hydroxamate group to generate more soluble derivatives of octadentate DFO*, DFOB-PBH. Nevertheless, the combination of bioengineering and chemical synthesis yielded only small amounts of chelators [54]. Gasser *et al.* prepared by solid-phase syntheses a very similar octadentate DFO* derivative with four oxygen atoms in its backbone and called oxo-DFO* (Figure 7) [56]. ^{89}Zr-tagging of oxo-DFO* was performed efficiently at neutral pH and RT within 2 h of incubation (Table 1), suitable conditions for temperature-sensitive molecules [55]. In this proof-of-concept study, the authors also presented the *in vitro* stability of ^{89}Zr-oxoDFO* and compared it with those of less water-soluble ^{89}Zr-DFO* and DFO. Results showed that both the octa-coordinated ^{89}Zr-oxoDFO* and ^{89}Zr-DFO* outperformed the six-coordinated ^{89}Zr-DFO [55], however, *in vivo* data were not reported.

Linear tetrameric hydroxamic acid ligands were prepared by Brown *et al.* as a potential BFCA for immunological $^{89}Zr^{4+}$ PET imaging conjugating PPH (5-[(5-aminopentyl)(hydroxy) amino]-5-oxopentanoic acid) or PPH^{N}O^{C}O (2-(2-((2-(2-aminoethoxy)ethyl)(hydroxy)amino)-2-oxoethoxy)acetic acid) to desferrioxamine B (Figure 7) [57]. DFOB-PPH and DFOB-PPH^{N}O^{C}O were compared with DFO* and DFO in challenge experiments with the Fe^{3+} metal ion and EDTA chelator. Results showed that tetrameric DFO*, DFOB-PPH, and DFOB-PPH^{N}O^{C}O displayed a marked preference for Zr^{4+} over Fe^{3+}. The initial formation rates of the Zr-DFOB-PPH and Zr-DFOB-PPH^{N}O^{C}O complexes were higher than that of Zr-DFO*, which could reflect a superior match between the Zr^{4+} ionic radius and the increased volume of the coordination sphere provided by the two DFO derivatives. In the presence of excess EDTA, Zr-DFOB-PPH^{N}O^{C}O dissociated faster than Zr-DFO* and Zr-DFOB-PPH, suggesting that any beneficial increase in water solubility conferred by the presence of ether -oxygen atoms in the chelator is counterbalanced by a reduction in complex stability. Outer-sphere solvation of the ether-oxygen atoms in Zr-DFOB-PPHNOCO may

increase the entropic contribution to the dissociation of the complex [24]. Based on this pilot investigation, the authors identified DFOB-PPH as a ligand with a conceivable use for ^{89}Zr-immunoPET imaging [57].

Donnelly's group proposed a squaramide (Sq) ester derivative of DFO, where two oxygen atoms on the Sq dione backbone were expected to complete the metal coordination sphere (NC=8) (Figure 7) [58]. Even if there is no evidence of octa-coordination, ^{89}Zr-labeled DFO-Sq conjugates produce complexes that are more stable versus ligand exchange reactions than the corresponding DFO derivatives. The same group appended DFO-Sq to Tyr^{3}-octreotide (DFOSq-TIDE) and Tyr^{3}-octreotate (DFOSq-TATE) and labeled them with ^{68}Ga or ^{89}Zr at RT (RCY> 95% in 30min) [59]. All four agents showed good tumor uptake in an AR42J xenograft model expressing SSTR2 and produced good quality PET images.

Chomet *et al.* reported a head-to-head comparison of DFO* and DFO chelators to select the best candidate for clinical immunoPET [60]. In this study cetuximab and trastuzumab antibodies were tagged with ^{89}Zr *via* DFO-NCS, DFO*-NCS, DFOSq or DFO*Sq to compare their *in vitro* stability after incubation in serum (37 °C, 7 days), in formulation solution (24 h), and in the presence of an excess of exchanging chelators such as EDTA, DFO, and DFO*. Besides, the ^{89}Zr-DFO* and ^{89}Zr-DFO chelate's stability towards challenging metals was assessed by using a panel of endogenous metal cations selected for their coordination capacity for DFO. Outcomes of this study again highlight the superiority of octadentate ligands for Zn^{4+} and give an important contribution to the understanding of the complexation behavior of the Sq group. However, ^{89}Zr-DFO* derived conjugates always resulted in higher stability compared to their DFO counterparts, while ^{89}Zr-DFO-NCS-mAb and ^{89}Zr-DFOSq-mAb showed comparable stability. The difference in the stability features of DFOSq and DFO* derivatives supports the suspect that the Sq group is not involved in coordination with the metal ion or does not have the same bond strength as the hydroxamate ligands. Biodistribution studies of ^{89}Zr-antibody conjugates performed in two different xenograft tumor models (HER2 and EGFR-expressing), showed similar tumor uptake for all conjugates, but lower bone uptake for DFO* cetuximab and trastuzumab conjugates. Lower bone uptake of DFO* conjugates was also confirmed with an intratibial (BT-474) model of bone metastasis, where DFO* conjugates demonstrated superior detection of tumor-specific signal and much better tumor-to-background contrast than DFO conjugates. Therefore, the authors concluded that DFO* was more performing both *in vitro* and *in vivo* than the clinical gold standard DFO, irrespective of the linker used (NCS and Sq) [60]. These results corroborate the data obtained by Berg *et al.* in a previous comparative investigation, in which total-body imaging of rhesus monkeys was performed, up to 30 days after the administration of a ^{89}Zr-tagged humanized mAb specific to herpes simplex viral glycoprotein D [61]. Labeling was achieved via DFO-NCS, DFO*-NCS, DFOSq or DFO*Sq, to evaluate and compare their pharmacokinetics. Authors found that Zr-DFO* and DFO*Sq complexes showed markedly lower bone uptake at 30 days p.i. compared to their DFO counterparts [61].

DFO-HOPO is another DFO-based octadentate chelator that was initially developed as a sequestering agent for treating plutonium (IV) poisoning [62]. DFO-HOPO contains three hydroxamic acid groups from DFO and one hydroxypyridinone group (Figure 7) [63]. Allot *et al.* used the non-radioactive ^{nat}Zr-DFO-HOPO complex to confirm the coordination of the metal ion by the chelator by spectrometric and spectroscopic analyses. Additionally, DFT calculations were performed to verify the steric and electronic ability of DFO-

HOPO to generate a Zr^{+4} octadentate chelate. In accordance with the lower-energy conformation, the optimized geometry presents a metal center coordinated to eight oxygen atoms of the chelator. Like in the case of ^{89}Zr-DFO*, the enhanced coordination ability exerted by the octadentate chelator improved the stability of ^{89}Zr-DFO-HOPO compared to ^{89}Zr-DFO [63]. Therefore, the DFO-HOPO chelator showed good potential for the future development of biomolecules labeled with ^{89}Zr.

4.2.3 Other hydroxamate derivatives. Guérin *et al.* reported a new branched acyclic N-hydroxy-N-methyl succiamide-based chelator (4HMS in Figure 7) with eight O donor atoms for $^{89}Zr^{+4}$ complexation. Radiolabeling efficiency, stability, and *in vivo* performance of ^{89}Zr-4HMS were assessed and compared with ^{89}Zr-DFO [64] ^{89}Zr-4HMS was obtained at pH 7 and RT in 5-10 min with a molar activity 3 times higher than that of ^{89}Zr-DFO. *In vitro* studies demonstrated that ^{89}Zr-4HMS was stable against transmetalation and transchelation. Additionally, *in vivo* studies demonstrated that the complex was cleared from most tissues in 24 h and that at this time the uptake of kidney, liver, bone, and spleen was significantly low. These features make 4HMS a promising chelator for the development of ^{89}Zr-RPs.

To combine the kinetic inertness of the macrocyclic structure with the need to have eight oxygen donor atoms, Guérard has designed and tested a series of cyclic (C5-7) and acyclic (L5-7) tetrahydroxamic acid chelators suitable for generating octa-coordinated Zr-complexes [65, 66] (Figure 7). In this study, the length of the carbon chain between each coordinating unit (from 5 to 7 carbon atoms) was changed to vary the pre-organization of the ligand, thus finding the optimal ring size that gives Zr-complexes thermodynamically stabile and kinetically inertness. Macrocycles comprising 28, 32, or 36 atoms (C5-7) were designed and compared with their corresponding linear counterparts (L5-7), assessing the impact of the macrocyclic effect on the stabilization of the compounds. The larger ligands C7, L7, and L6 were found to provide excellent complexation capabilities (> 99% complexation after 120 min at 20 °C). The corresponding ^{89}Zr-complexes were characterized by excellent stability and inertness properties. Both linear and cyclic chelates with a 7-term length spacer were more stable than ^{89}Zr-DFO. As expected, better results were achieved with the cyclic C7 chelator (36 atom ring) compared to its linear counterpart L7.

Supported by the results of Guérard, Seibold *et al.* designed a new macrocyclic based on important assumptions, so the ligand: 1) must include four hydroxamate coordinating units, to fully satisfy the coordination requirements of the highly oxophilic Zr^{4+}; 2) should be cyclic to exploit the macrocyclic effect; 3) should be rotationally symmetric to allow the formation of a symmetrical complex, reducing isomerism; 4) should be hydrophilic and 5) should possess a chelator cavity (ring) size that fits the radius of the central metal ion to maximize the complex stabilities. The results of computational studies indicated that the ring must contain at least 36 atoms. Therefore, authors developed a four-hydroxamate-containing chelator, CTH36, for the stable complexation of Zr^{4+} (Figure 7) [67]. CTH36 was efficiently labeled at RT, within 30-60 min, under mild reaction conditions and the ^{89}Zr-CTH36 coordination compound was stable to challenge with EDTA at neutral pH.

Zhai *et al.* investigated in parallel the properties of a cyclic natural siderophore with three hydroxamate units, fusarinine C (FSC), initially studied for ^{68}Ga-labeling and its triacetylate derivative (TAFC) (Figure 7) [68]. The authors assumed that FSC could be a good option for ^{89}Zr-labeling with chelating properties similar those of DFO but with potentially higher stability because of its cyclic structure. Labeling of DFO

and TAFC was carried out efficiently at RT and neutral pH by incubation with ^{89}Zr-oxalate and a very small amount of chelators. Despite the presence of only six coordinated atoms, ^{89}Zr-FSC/TAFC possesses excellent stability and inertness compared to ^{89}Zr-DFO, supporting the added value of the cyclic structures *vs* the linear one. The higher ^{89}Zr-TAFC stability was confirmed by a competition study, in which ^{89}Zr-DFO completely transchelated within 1 h, in the presence of 1000-fold molar excess of TAFC. In contrast, 40% of ^{89}Zr-TAFC was intact after 7 days of incubation in a 1000-fold molar excess of DFO. FSC presents three secondary amino groups that can be used as anchor sites for targeting vectors and generate trimeric structures. This feature is a limitation in immunoPET, where conjugation to the BFCA of a single antibody is preferred. To overcome this drawback and improve the coordination properties of FSC-based chelators, FSCs were modified by introducing additional carboxyl groups to saturate the 8-coordination position of Zr^{4+} and embed functionalities for the conjugation to one targeting vector, indicated as FSC(succ)$_2$, FSC(succ)$_2$AA, FSC(succ)$_3$ in Figure 7 [69]. The complexation with $^{Nat}ZrCl_4$ was promptly achieved, resulting in high purity ^{nat}Zr-FSC(succ)$_2$AA and ^{Nat}Zr-FSC(succ)$_3$ complexes with 1:1 stoichiometry as determined by ESI-MS spectroscopy. ^{89}Zr-complexes were efficiently prepared under mild conditions from ^{89}Zr-Ox$_2$ and their chemicalphysical properties and stability were compared with those of the prototype ^{89}Zr-TAFC and the gold standard ^{89}Zr-DFO. The radiocompounds displayed high PBS and human serum (HS) stabilities and low protein-bound activity over a period of 7 days. Acid dissociation and transchelation studies revealed different *in vitro* stabilities, in the order: ^{89}Zr-FSC(succ)$_3$ > ^{89}Zr-TAFC > ^{89}Zr-FSC(succ)$_2$AA >> ^{89}Zr-DFO. The superior stability of the TAFC- and FSC-containing complexes with respect to ^{89}Zr-DFO is due to the macrocyclic structure. Moreover, the increased stability of ^{89}Zr-FSC(succ)$_3$ over its ^{89}Zr-analogs was attributed to its higher coordination number and better geometrical arrangement. The lower stability of ^{89}Zr-FSC(succ)$_2$AA compared to ^{89}Zr-FSC(succ)$_3$ could be due to the loss of the symmetrical structure. However, the successful synthesis and promising results obtained with ^{89}Zr-FSC(succ)$_2$AA highlight the potential of FSC(succ)$_2$ as a monovalent chelator for conjugation to targeting molecules such as mAbs [69].

Very recently, two new semi-rigid chelators based on the seven-membered heterocycle 6-ammino-1,4-diazepane scaffold were added to the series of hydroxamate derivatives (Figure 8) [70, 71]. These chelators are characterized by a backbone that includes two nitrogens that belong to the macrocyclic diazepam scaffold and one exocyclic nitrogen, which are coupled with hydroxamate-containing side chains. The N-methyl-hydroxamate groups were maintained as donor groups to efficiently coordinate the metal ion. These hybrid structures combine the advantages of linear and cyclic systems, allowing for fast radiolabeling under mild conditions and high stability of the complex. This kind of chelator was previously investigated for the complexation of other trivalent radiometal ions.

Klasen *et al*. described the development of the Hy3ADA5 chelator (5-(6-(4-(5-(6-(4-(benzyloxy)(methyl)amino)-4-oxobutanaamido)-1.4-bis(4-((benzyloxy)(methyl)amino)-4-oxobutanoy1)1,4diazepan-6-yl)pentanoic acid and two additional bifunctional derivatives that carry a Sq or p-isothiocyanatophenyl active groups for protein conjugation and the *in vitro* evaluation of the corresponding ^{89}Zr-tagged chelates (Figure 8) [70]. Hy3ADA provides high RCY (>90%) after 60 min at RT, an extension of the incubation time to 90 min under the same conditions was necessary for Hy3ADA5-

Sq and Hy3ADA5-NCS to achieve high RCY. Both ^{89}Zr-Hy3ADA5 and ^{89}Zr-Hy3ADA5-Sq showed good stability after 7 days of incubation in PBS and HS. ^{89}Zr-Hy3ADA5-NCS was less stable, 77% of the complex was degraded 24 h after incubation in HS. Hy3ADA5 chelators were compared with DFO mesylate, DFO-Sq, DFO-NCS, and DFO*-NCS under identical conditions. Stability studies in PBS disclosed no measurable release of radiometal from DFO chelates, but after incubation in HS ^{89}Zr-DFO-Sq revealed slight instability and ^{89}Zr-DFO remained stable.

Hy3ADA5-Sq and Hy3ADA5-NCS were also conjugated to the model antibody bevacizumab to study the stability of the immunoconjugates. Constructs were radiolabeled under mild conditions, and the RCY of the corresponding ^{89}Zr-labeled immunoconjugates ranged from 82 to 89%; consequently, size exclusion chromatography purification was necessary to remove unbound radiometal before further *in vitro* investigations. Under identical reaction conditions, the linear analogs DFO-Sq-mAb and DFO-NCS-mAb showed superior ^{89}Zr-labeling properties providing fast and high-performance complexation of the radiometal. All investigated radio-immunoconjugates, based both on Hy3ADA5 and DFO, did not show significant loss of radiometal within the 7 days either in the formulation medium and in HS. However, *in vivo* studies were not reported [70].

Russelli *et al.* designed and developed two other new hexadentate chelators based on the 6-amino-1,4-diazepine scaffold, named AAZTHAS and AAZTHAG, for ^{89}Zr-labeling and PET-imaging. Their aim was to improve the rigidity of the ^{89}Zr-chelate using N-methyl-N-(hydroxyl)succinamide or N-methyl-N-(hydroxyl)glutaramide pendant group attached to the cyclic structure (Figure 8) [71]. *In vitro* studies demonstrated that AAZTHAG was the best chelating agent for ^{89}Zr, exhibiting a stability of 86% after 72 h of incubation in HS. The complex was also highly stable *in vivo,* and only low uptake of free ^{89}Zr was found in bones and kidneys. A functionalized version of AAZTHAG, activated with a reactive ester group, was prepared and combined to trastuzumab as evidence of its conjugation to molecules of medical interest. The final ^{89}Zr-radioconstruc proved to be stable in different solutions for at least 4 days. However, no *in vivo* studies in animal models have been reported.

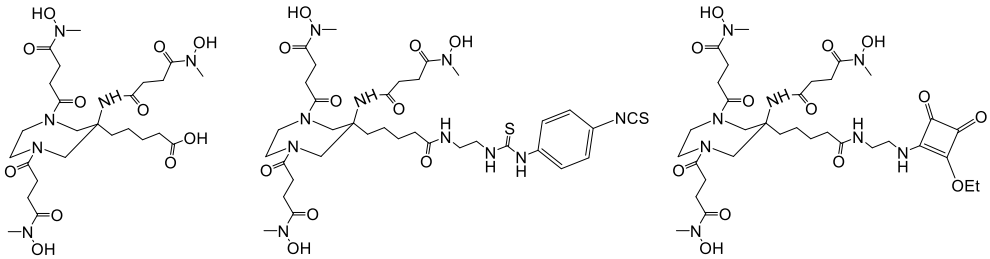

Hy$_3$ADA^5 (N$_3$O$_3$) **Hy$_3$ADA^5-p-Ph-NCS (N$_3$O$_3$)** **Hy$_3$ADA^5-Sq (N$_3$O$_3$)**

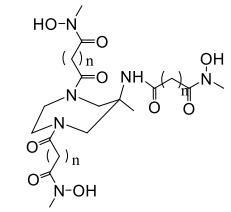

AAZTHAS (n=2); AAZTHAG (n=3) (N$_3$O$_3$)

Figure 8. Structures of ^{89}Zr semi-rigid chelators based on the 6-amino-1,4-diazepane framework used in radiopharmaceutical applications.

4.2.4 Hyroxypyridinone (HOPO)-based Chelators Over the past years, fruitful research by Raymond *et al.* has resulted in the development of a library of rationally designed ligands consisting of multidentate hydroxpyridinoate, hydroxyisopthalamide, terepthalamide and catecholate coordinating units, as actinide sequestration agents [72] and numerous attempts have been made to adapt them for Zr^{+4} radiochemistry.

Deri *et al.* proposed a linear chelator composed of four hydroxypyridinone groups (HOPO) to chelate the Zr^{4+}, as an alternative to hydroxamate-based ligands [73-75]. HOPO is an octadentate ligand made up of a speramine scaffold coupled with four hydroxypyridinone units, thus offering eight oxygen donors for Zr^{4+} metal binding (Figure 9). The crystal structure of Zr-HOPO confirmed the formation of a neutral specie in a dodecahedral geometry, in which the central metal is coordinated to eight oxygen atoms from the four 1.2-HOPO groups, (Figure 10). The radiosynthesis of ^{89}Zr-HOPO was efficiently conducted in water at RT and neutral pH. Incubation times depended on the concentration of the ligand; low concentrations required extended reaction times (60 min). ^{89}Zr-HOPO shows superior stability than ^{89}Zr-DFO, demonstrating remarkable resistance to transchelation, over 7 days, to 100-fold excess of EDTA in various pH values, and to competition with an excess (10-fold) of different metal ions at physiological pH and 37 °C [74].

Ma *et al.* reported the use of tripodal chelators, originally planned for ^{68}Ga-radiolabeling. These are a tris(hydroxpyridinone) ligand containing 1,6-dimethyl-3-hydroxpyridin-4-one chelating units, designed as CP256 or THP, and its bifunctional analog, YM103, characterized by a maleimide group, useful for site-specific conjugation of antibodies through available active cysteine residues (Figure 9) [76]. Both CP256 and the conjugated YM103-trastuzumab were labeled with ^{89}Zr with high yield and specific activity. ^{89}Zr-CP256 proved to be stable *in vitro* and *in vivo;* nevertheless, the corresponding ^{89}Zr-YM103-trastuzumab was much less robust, and upon *in vivo* administration a significant increase in radioactivity accumulation in bone tissues was detected compared to ^{89}Zr-DFO-trastuzumab as a reference. These results led the authors to conclude that the tripodal configuration of the hydroxypiridinone units in CP256 and YM103 chelator was not optimal for $^{89}Zr^{4+}$ stabilization.

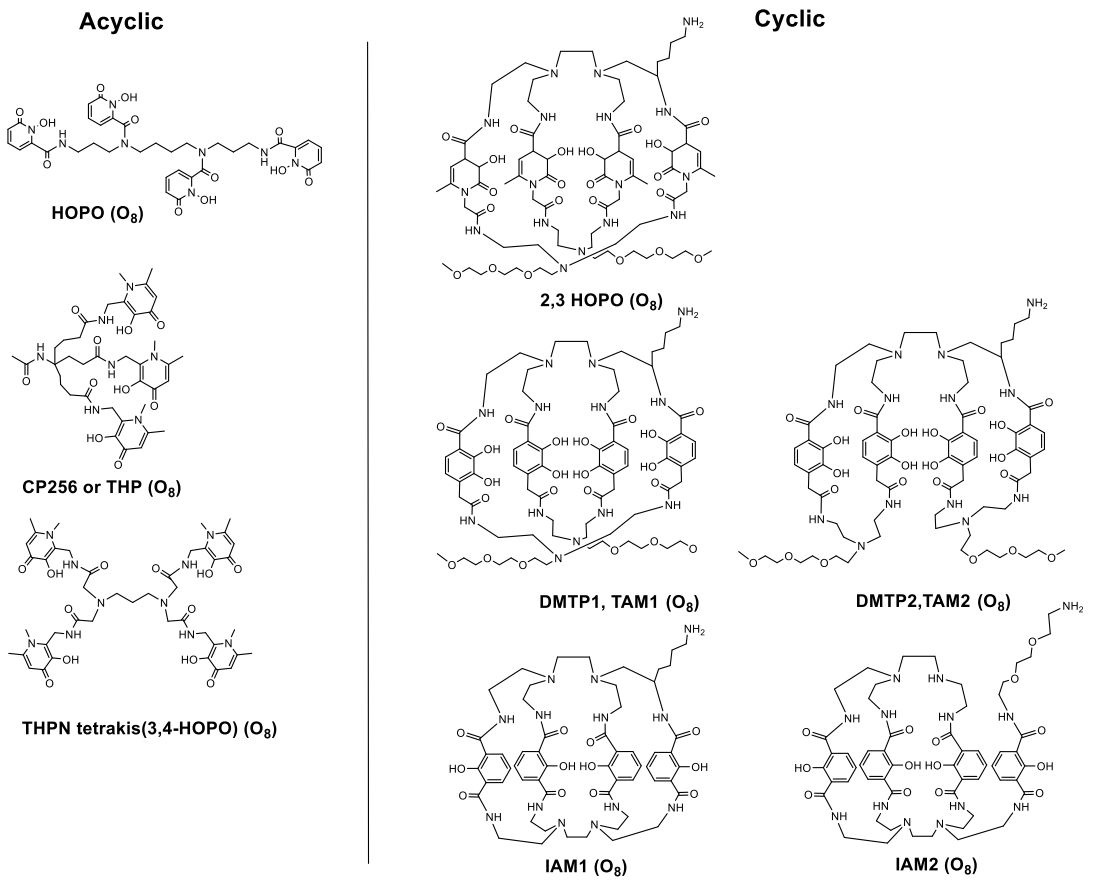

Figure 9. The structure of ^{89}Zr hyroxypyridinone-(HOPO)-based chelators used in radiopharmaceutical applications.

In an attempt to overcome the limits of CP256 and YM103 and completely satisfy the octa-dentate metal coordination sphere, Buchwalder *et al.* investigated a tetrapodal chelator based on four 3-hydroxy-4-pyridinone (3,4-HOPO) coordinating groups (THPN) [77].

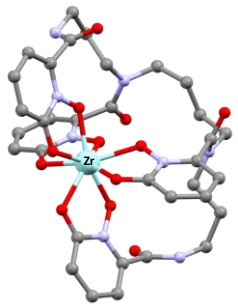

Figure 10. Crystal structure of Zr-HOPO

Computational studies and spectrometric analysis of the ^{nat}Zr-THPN complex show a 1:1 Zr-to-THPN stoichiometry, indicating that the coordination sphere around the metal ion is saturated by the octadentate THPN ligand. The thermodynamic stability of ^{na}tZr-THPN was measured in solution titration experiments. Data revealed one of the highest formation constants found for a Zr-chelate ($\log\beta_{ML}$ = 50.3; pM = 42.8) [78]. The closest reported value is for the ^{nat}Zr-(3,4,3-LI(1,2-HOPO) complex: $\log \beta_{ML}$ = 43.1, 7 orders of magnitude lower [79]; while the stability constant for the ^{nat}Zr-DFO system was $\log \beta_{MHL}$ =47.6 [80, 81]. At

the tracer level, quantitative formation of ^{89}Zr-THPN was achieved within 10 min at RT, with a concentration of 16.7 μM THPN. ^{89}Zr-THPN was stable in serum and exceed ^{89}Zr-DFO in the EDTA challenge, as well as in a direct competition study. Data from animal studies indicate that ^{89}Zr-THPN was rapidly excreted with no signs of demetalation or residual organ uptake. Encouraged by these preliminary results, authors further investigated the stability features of the Zr-chelate and produced the corresponding BFCA derivative (p-SCN-Bn-THPN). SCN-THPN derivative and SCN-DFO and SCN-DFO* were conjugated to the hyperbranched polyglycerol (HPG) carrier, to compare the stability of ^{89}Zr-complexes. The radiolabeling and the integrity of the radioconstructs were studied both *in vitro* and *in vivo* for several days. [78]. Although all three radioconjugates remained intact in HS over 5 days, the *in vivo* evaluation showed a lower physiological stability of ^{89}Zr-tagged bifunctional THPN conjugate than DFO and DFO* radiochelates, as shown by enhanced $^{89}Zr^{+4}$ bone uptake. This outcome is in contrast with the remarkably high thermodynamic stability of the chelate and suggests either kinetic or metabolic lability that could arise from coordinative changes, attributable to the covalent conjugation of the radiocomplex ^{89}Zr-THPN. Thus, a study aiming to increase the kinetic inertness of radiochelate is necessary [78].

Moving on macrocycle structures, Tinianow *et al.* described the preparation and evaluation of octadentate chelators containing 3-hydroxypyridin-2-one coordinating units in a di-macrocyclic motif (BPDETLysH22-2,3-HOPO) and its mAb derivative [82]. The "clam shell" design of this bi-macrocyclic ligand was selected as a compromise between a linear structure of DFO-like siderophores and a rigid macrocyclic arrangement to permit a fast complexation rate and enhanced stability of the resulting complex, which cannot be achieved by acyclic ligands. The incorporation of the pendant free amino group was conceived as the conjugation site for mAbs or other molecular vectors. Radiochemical tests revealed that 2,3-HOPO was quantitatively radiolabeled with ^{89}Zr within 15 min at RT, suggesting that this ligand exhibits ^{89}Zr-binding features that are similar to those of other HOPO and terepthalamide (TAM) chelators described in the literature [75, 83]. ^{89}Zr-2,3-HOPO was found more resistant to DTPA challenge than ^{89}Zr-DFO: 22% *vs* 59% transchelation respectively, during the 7-day study. While the stability of ^{89}Zr-2,3-HOPO was not as impressive as that of chelators reported with analogs coordinating motifs [75, 83].

Roy *et al.* newly reported the *in vitro* and *in vivo* comparison of 3,2-HOPO *vs* DFO-based chelation conjugated to antimesothelin mAb, anetumab (MSLN) in three different tumor xenografts (NCI-Meso16, NCI-Meso21, and HT29-MSLN) [84]. Radiolabeling was performed by incubating $^{89}Zr^{4+}$ and MSLN-conjugates at RT for 1 h. The RCY for ^{89}Zr-3,2-HOPO-MSLN was lower (80-85%) than for ^{89}Zr-3,2-DFO-MSLN (90–95%) thus PD10 purification was necessary to improve the RCP of the first one. Both ^{89}Zr-MSLN conjugates demonstrated a high binding affinity against MSLN target in pertinent cancer cell lines and their pharmacokinetic profiles were similar, except for tumor and femur. *Ex vivo* biodistribution and PET/CT imaging studies revealed that ^{89}Zr-3,2-DFO-MSLN displayed higher tumor uptake and low bone concentration than ^{89}Zr-3,2-HOPO-MSLN over 6 d. Furthermore, *in vitro* stability studies in HS indicated that ^{89}Zr-3,2-HOPO-MSLN was less stable than ^{89}Zr-3,2-DFO-MSLN, but the degradation products of the conjugates were not specifically identified [84].

Pandya *et al.* reported other di-macrocyclic chelators TAM1 and TAM2 that contain four TAM coordinating units to generate an eight-coordinate complex. [83]. These coordinating units are highly acidic and exist in

solution at neutral pH, as di-anions prompt to bind the Zr^{4+} cation with great avidity [72]. The ligand scaffold includes a pendant arm having a primary amine, suitable for conjugation to a variety of targeting ligands. The nonradioactive ^{Nat}Zr-TAM1 and ^{Nat}Zr-TAM2 complexes were easily prepared and ESI-MS analysis confirmed the 1:1 binding of $^{Nat}Zr^{4+}$ and the chelator. Data from DFT calculations indicate that the two complexes possess strikingly similar structures, despite differences in the connectivity of the ligands. TAM1 and TAM2 are coordinated with the metal center in an octa-coordinated mode by using the eight anionic oxygen atoms of the ligand. In both structures, the coordination environment of the Zr^{4+} ion is closest to a llll-edge antiprism. Despite the differences in rigidity, radiochemistry studies demonstrated that TAM1 and TAM2 were efficiently radiolabeled using the same conditions needed for ^{89}Zr-DFO, within 15 min at RT. Once formed ^{89}Zr-TAM1 and ^{89}Zr-TAM2 were more resistant to DTPA challenge than ^{89}Zr-DFO, and showed comparable stability in serum. Biodistribution studies carried out in healthy mice showed that the more rigid ^{89}Zr-TAM1 complex was cleared faster from all tissues and was more stable *in vivo* compared to ^{89}Zr-TAM2 consequently, very low bone accumulation was detected. These data seem to indicate that TAM1 may be considered a good candidate for further investigation.

Bhatt *et al.* reported a pair of macrocyclic chelators characterized by the presence of hydroxyisopthalamide (IAM) as coordinating units (Figure 9) [85]. Interest in these ligands was due to the fact that coordination motifs are similar to those used by bacteria for metal ion sequestration and have been successfully exploited as ligands for a variety of lanthanide metal cations [72]. Thus, IAM-based systems were assumed to chelate Zr in an octadentate fashion *via* a combination of phenolic and carbonyl oxygen atoms. Besides, the IAM framework can be easily modified to obtain a number of ligands with different chemical features. IAM1 was formulated as a rigid tri-macrocycle composed of 24 and 30 member rings, while the IMA2 ligand was designed as a more flexible bi-macrocycle composed of 24 and 27 member rings. These structural differences were found to affect their behavior *in vitro* and *in vivo*. Radiochemistry studies showed that both ligands can be labeled in very high yield with ^{89}Zr. However, the more rigid IAM1 chelator requires forcing reaction conditions (elevated reaction time and temperature), which are not suitable for radiolabeling of mAb conjugates. The more flexible IAM2 was quantitatively labeled at a lower temperature and reduced incubation time. Nevertheless, ^{89}Zr-IAM1 was more resistant to DTPA and serum challenge, demonstrating higher *in vivo* stability than the corresponding ^{89}Zr-IAM2. Upon ^{89}Zr-IAM1 administration animal retained less activity in hepatic, renal, and bone tissues than those treated with ^{89}Zr-IAM2, but their pharmacokinetic properties did not surpass those of ^{89}Zr-DFO [85].

4.3. Radiosynthesis

The zirconium-89 isotope, thanks to its long half-life (78 h) and decay mode, is an excellent radionuclide for immunoPET imaging with whole IgG antibodies. Unluckily, labeling these vectors may be a tricky process. Antibodies and their derivatives are often sensitive to pH and temperature, and the presence of different salts and buffers may generate aggregation and precipitation. Therefore, radiosynthesis must be performed under mild reaction conditions, in an adequate pH range (close to neutrality), at room temperature or 37 °C to avoid both irreversible aggregates formation and protein denaturation.

Additionally, the exploration of ^{89}Zr isotope in the immuno-imaging area has been limited by the complicate aqueous chemistry of Zr^{4+}, because under nonacid conditions it is possible to form multinuclear species or colloids [6] that are not suitable as starting materials for $^{89}Zr^{-}$complex formation [86-89]. Consequently, when radiolabeling with $^{89}Zr^{4+}$ in aqueous solutions it is necessary to prevent the formation of insoluble or polymeric ^{89}Zr-hydroxo species, as well as the control of pH and temperature.

Currently, different chelators for effective labeling with $^{89}Zr^{4+}$ have been investigated (*vide supra*). Table 1 summarizes the **^{89}Zr** tagging conditions and the labeling efficiency and effectiveness of the ligands mentioned above. In particular, most of the investigated chelators were originally proposed for other metals or radionuclides [90], thus the labeling could be inefficient and the complexes suffer from reduced stability.

Table 1. Tagging properties of the chelators for ^{89}Zr

Chelator	Amount	Molar Activity	Labeling conditions	RCY (%)	Stability over 7 d	note	Ref
Polyazacarboxylate							
DTPA			RT, pH 7, 60 min	0.10	Unstable		[91]
H_6Phospha			37 °C, pH 7, 60 min	12.0			[42]
DOTA	10 µg		$^{89}Zr(Ox)_2$ (~20 MBq in 100 µL) pH 7.2-7.5 with Na_2CO_3 (1 M), 99 °C, 2 h. $^{89}ZrCl_4$ (40 MBq in 100 µL), 0.5 M HEPES, 95 °C, pH 7.2, 1 h.	65 ± 9.6 99	Stable in HS, to transchelation with EDTA and biologically relevant metal ions challenge. Bone uptake 0.025 %ID/g.	Non suitable for temperature-sensitive molecules	[46]
TRITA	10-50 µg 18-24 µgg	0.89 GBq/µmol	$^{89}Zr(Ox)_2$ (~20 MBq in 100 µL) pH adjusted to 6.9−7.3 with HEPES (0.5 M, pH 7.1−7.3), 99 °C, 2 h. $^{89}ZrCl_4$ (40 MBq in 100 µL) 0.5 M HEPES, 180 °C microwave heating, pH 3.9-4.2, 1 h.	3 ± 1.3 80	~90% of the initial activity of ^{89}Zr-TRITA was transchelated to EDTA, 62% of the compound remain intact after transmetalation with biologically relevant metal ions.		[47]
NOTA **PCTA**	10-50 µg		$^{89}Zr(Ox)_2$, pH adjusted to 6.9−7.3 with HEPES (0.5 M pH 7.1−7.3), 99 °C, 2 h.	15 ± 5.7 35 ± 9.3	~35% of the activity initially of ^{89}Zr-NOTA was transchelated to EDTA. 88-99% of the compound remain intact after transmetalation with Ga^{3+} and Cu^{2+}. ^{89}Zr-PCTA stable in HS, to transchelation with excess EDTA and challenge of biologically relevant metal ions.		[47]
	15-20 µg	0.99 GBq/µmol 0.10 GBq/µmol	$^{89}ZrCl_4$ (40 MBq in 100 µL), HEPES (0.5 M), pH 3.9-4.2, 37 °C, 1 h.	99			
Hydroxamate Based (DFO analogs)							
DFO	1 mM	57 GBq/µmol	$^{89}Zr(Ox)_2$ (37–100 MBq, RT, pH 7, 10 min.	98	Transchelation with EDTA (47-60 %). Unstable. Bone uptake > 10 %ID/g	Gold standard	[76, 92]
DFO*	3 µM	5 - 6 GBq/µmol	$^{89}Zr(Ox)_2$ (37–100 MBq) neutralized with Na_2CO_3 (2 M), pH adjusted to 6.8−7.2 with HEPES (1 M, pH 7.1−7.3), RT, 2 h.	100	Stable	Suitable for PET	[52]
Oxo-DFO*	10 µM	---	$^{89}Zr(Ox)_2$(10–20 MBq) neutralized with Na_2CO_3 (2 M), pH adjusted to 6.8−7.2 with HEPES (0.5 M, pH 7.4), RT, 2 h.	99	Stable to transchelation at RT and pH 6 with an excess of DTPA (5 mM or 50 mM).	Suitable for PET	[55]
DFO-sq	---	---	$^{89}Zr(Ox)_2$ neutralized with Na_2CO_3 (2 M), pH adjusted to 6.8−7.2 with HEPES (0.5 M, pH 7.4), RT, 25 min.Purified on PD-10 size exclusion column	100	Quite stable: slight transchelation to EDTA (50 mM) at 24h, 50 °C	Suitable for PET	[58]
DFO-HOPO	3–8 µM	20 MBq/nmol	$^{89}Zr(Ox)_2$(20–45 MBq) neutralized with Na_2CO_3 (2 M),	99	Stable to transchelation with EDTA and DFO. Stable in mouse serum and PBS.	Suitable for PET	[63]

			pH adjusted to 7 with HEPES (0.5 M, pH 7), RT, 1 h.				
4HMS	7-8 nmol/ 205 ul	170 GBq/µmol	$^{89}Zr(Ox)_2$ (30 MBq) Na_2CO_3 (1 M)pH 7-7.5, RT, 10 min	99	Stable to transchelation with a 100-fold excess of DTPA, transferrin and biologically relevant ions. Stable in plasma and PBS. Bone uptake 0.2% ID/g	Suitable for PET No bioconj. version	[64]
Linear tetrahydroxamate n=5, L5	150 µM	0.96 MBq/nmol	$^{89}Zr(Ox)_2$, Na_2CO_3 (1 M), pH 7, 80 °C 30 min	87	Stable in HS and PBS. Unstable to transchelation with EDTA		[65, 66]
Linear tetrahydroxamate n=6, L6	150 µM	1.26 MBq/nmol	$^{89}Zr(Ox)_2$, Na_2CO_3 (1 M), pH 7, RT, 2 h	95	Stable in HS and PBS. Unstable to transchelation with EDTA		[65, 66]
Linear tetrahydroxamate n=7, L7	150 µM	1.31 MBq/nmol	$^{89}Zr(Ox)_2$, Na_2CO_3 (1 M), pH 7, RT, 2 h	99	Stable in HS, PBS and to transchelation with EDTA (79%)	Suitable for PET No bioconj. version	[65, 66]
Cyclic tetrahydroxamate n=5, C5	150 µM	0.30 MBq/nmol	$^{89}Zr(Ox)_2$, Na_2CO_3 (1 M), pH 7, 80 °C, 30 min	29	Stable in HS and PBS. Unstable to transchelation with EDTA.		[65, 66]
Cyclic tetrahydroxamate n=6, C6	150 µM	1.21 MBq/nmol	$^{89}Zr(Ox)_2$, Na_2CO_3 (1 M), pH 7, 50 °C, 30 min	92	Stable in HS and PBS. Unstable to transchelation with EDTA		[65, 66]
Cyclic tetrahydroxamate n=7, C7	150 µM	1.31 MBq/nmol	$^{89}Zr(Ox)_2$, Na_2CO_3 (1 M), pH 7, RT, 2 h	99	Stable in HS, PBS and stable to transchelation with EDTA (87%)	Suitable for PET No bioconj. version	[65, 66]
CTH36	0.6 µM (320 nmol)	8.4–9.2 GBq/µmo	$^{89}Zr(Ox)_2$ oxalate solution (0.1M ; 13.5-18.5 MBq in 10 µL) pH adjusted to 6.9−7.3 with HEPES (0.25 M), RT, pH 7, 30-60 min	95	Stable to 100-fold excess of EDTA	Need further validation	[67]
FSC	58 µM	25 GBq/µmol	$^{89}Zr(Ox)_2$(30 MBq) neutralized with Na_2CO_3 (1 M), pH adjusted to 6.8-7.2 with HEPES (0.5 M, pH 7), RT 90 min	100	Stable in HS, PBS, to transmetalation with DFO (40%) and to transchelation with 1000-fold excess of EDTA pH 7 (<6%).	Suitable for PET No Ab bioconj. version	[68]
Hy_3ADA^5	3.33 mM		$^{89}Zr(Ox)_2$(10-12 MBq) neutralized with Na_2CO_3 (2 M), pH adjusted 7 with HEPES (0.5 M, pH 7), RT 90 min. need of purification	82 - 89	Stable in PBS and HS	Need further evaluation	[70]
AAZTHAG	3.33 mM		$^{89}Zr(Ox)_2$ (37 MBq) neutralized with Na_2CO_3 (2 M), pH adjusted 7 with HEPES (0.5 M, pH 7), 37 °C, 30 min, purified by PD10	60	Stable in HS, PBS and *in vivo*, low bone accumulation	Need further evaluation	[71]
Hyroxypyridinone-(HOPO)-based							
HOPO	10 mM/10 µM		$^{89}Zr(Ox)_2$, Na_2CO_3 (1 M), pH 6.8-7.2, RT, 10 min/45 min[a]	100	Stable in HS, to transchelation with a 100-fold excess of EDTA in a wide pH range and to metal ions challenge Bone uptake 1 %ID/g.	Suitable for PET	[75]

CP256 **YM103**	1 mM/100 µM		$^{89}Zr(Ox)_2$, (500 kBq, 2.5 µL), ammonium acetate (0.1 M), pH 6.5, RT, 10 min. $^{89}Zr(Ox)_2$, (500 kBq, 2.5 µL), ammonium acetate (0.1 M), pH 6.5, RT, 60 min[a]	99 9	Stable to transmetalation with 10-fold excess of DFO, (7% dissociation). Vulnerable to transmetalation with 10-fold excess of (86% dissociation). Bone uptake 29 %ID/g.		[76]
THPN	16.7 µM		$^{89}Zr(Ox)_2$, Na_2CO_3 (0.1 M), pH 6-7, RT, 10 min [a]	100	Stable in HS; stable to transchelation with 100-fold excess of EDTA over a wide pH range and to metal ions challenge. Bone uptake 1 %ID/g.	BFCA version have lower stability over the corresponding DFO and DFO*	[77, 78]
2.3-HOPO	10 mM-10 µM	0.9 GBq/µmol	$^{89}Zr(Ox)_2$, (74-150 MBq/ 100 µL neutralized with Na_2CO_3 (2 M), pH adjusted 7 with HEPES (0.5 M, pH 7), RT, 15 min. Ab-conjugated version needof purification by PD10	100	Limited stability in mouse serum	Need further evaluation	[82]
DMTP1, TAM1 **DMTP2, TAM2**	60 µM 60 µM	0.99 GBq/µmol 0.98 GBq/µmol	$^{89}Zr(Ox)_2$ (22 MBq) Na_2CO_3 (1 M), pH 7-7.5, RT, 15 min	100 100	Stable in HS and to transchelation with DTPA (50 mM) at pH 7.	Need further evaluation	[83]
IAM1 **IAM2**	5±10 µL,(1.0 mg/mL in H_20)	0.7 GBq/µmol	$^{89}Zr(Ox)_2$,(22.2 Mbq) pH 7-7.5 by Na_2CO_3 (1 M), 95 °C, 2 h. $^{89}Zr(Ox)_2$,(22.2 Mbq) pH 7-7.5 by Na_2CO_3 (1 M), 50 °C, 1 h	100	Stable in HS and to transchelation with DTPA at pH 7. Only 15% and 28% of the complex transchelate after 1 and 7 d, respectively Unstable to transchelation with DTPA. 37% and 74% of complex transchelate after 1 and 7 d, respectively.	Non suitable for temperature-sensitive molecules Not stable enoght	[85]

[a] The lowering of the ligand amount caused the complexation time to increase. Note: by increasing the number of coordination sites, the resulting complex stability improved. $^{89}Zr(Ox)_2$ as [^{89}Zr]Zr-oxalate solution

Zirconium-89 is usually supplied in a 1 M oxalic acid solution [93], where it is accessible the formation of stable and soluble monomeric or low molecular weight $^{89}Zr^{4+}$species such as zirconium oxalate ($^{89}Zr(Ox)_2$) apt as precursors for ^{89}Zr-RPs preparation. Therefore, most radiosyntheses are based on ligand-substitution reactions of $^{89}Zr(Ox)_2$ intermediates (see Table 1). The presence of oxalic acid, as well as the pH (~ 4) of these reactions may have implications on radiolabeling efficiency that can be significantly reduced. The elimination of the excess of oxalic acid prior to ligand addition [93] or the replacement of $^{89}Zr(Ox)_2$ with $^{89}ZrCl_4$ as an alternative starting material significantly improves the radiochemical yield of the final ^{89}Zr-chelates [46, 47].$^{89}ZrCl_4$ can be easily produced by loading a $^{89}Zr(Ox)_2$ solution onto an activated Sep-Pak QMA anion exchange cartridge [46, 47]. Oxalic acid is removed by washing the cartridge with water (>50 ml). The activity can be completely eluted as $^{89}ZrCl_4$ by chloride ion exchange (1.0 M HCl_{aq}.). However, $^{89}ZrCl_4$ in aqueous solutions can rapidly undergo polymerization, due to the high dilution [94].

The ^{89}Zr solutions must be neutralized prior to use due to the sensitivity of antibodies to acid pH values. Hence, the use of buffer is necessary to adjust the reaction pH at 7–7.5; carbonate buffer (1-2 M), sodium acetate (0.25 M) and 0.9% saline solutions, as well as HEPES buffer (0.25-1 M, pH 6.8–7.4) and sodium

citrate (5 mM) with HEPES solution (0.5 M) are frequently used, while phosphate buffer should be avoided to prevent the formation of colloidal zirconium phosphate. Among these buffers, high concentrated carbonate is preferred because its tendency to form soluble complexes with zirconium can prevent metal precipitation, thus increasing the amount of $^{89}Zr^{4+}$ available in solution for radiolabeling. However, the concentration must be controlled and the solution should not exceed pH 9, to avoid the formation of insoluble mixed carbonate hydroxide complexes [95]

When $^{89}Zr(Ox)_2$ solutions are used as the starting material for the radiosyntheses, the oxalate concentration needs to be maintained high until zirconium has been chelated to minimize the formation of polymeric species. Vosjan e*t al.* strongly recommended that the total volume of $^{89}Zr(Ox)_2$ (37-185 MBq) to be neutralized should be at least 200 µL, whenever the required activity is lower than 200 µL, oxalic acid (1 M) has to be added to reach this volume. According to Vosjan method, the $^{89}Zr(Ox)_2$ solution can be neutralized by adding carbonate buffer (2 M, 90 µL,) followed by HEPES, (0.5 M pH 6.8–7.4; 300 µL) [96]. The free $^{89}Zr^{4+}$species and any unreacted small BFCA can be easily removed using a size-exclusion column such as desalting gravity flow columns (eg PD-10, NAP5) or spin columns with molecular weight cut-offs of 10 to 50 kDa, which also serves as a convenient method of exchange of the solution buffer into injectable formulations [97]. The addition of gentisic acid, as a stabilizer, is indicated to reduce radiolysis.

Looking at the labeling efficiency and effectiveness of the ligands presented in Table 1, it is clear that in general, linear chelators are able to quantitatively coordinate ^{89}Zr at room temperature in a reasonable time (30-60 min), excluding only DTPA, H_6Phospha, and L5. In contrast, macrocyclics often required heating, also at high temperature (99 °C), for extended times (30 min-2h), therefore, they are not suitable for the labeling of temperature sensitive molecules. Hence, despite the efforts to develop new chelators for coordination of $^{89}Zr^{4+}$, DFO and its acyclic derivatives seem to be the most suitable class of BFCAs so far, because radiolabeling of the corresponding immunoconjugates is rapid under mild conditions and the resulting radioimmunoconjugates are sufficiently stable *in vivo*.

Among the overall tested chelators, many are efficiently radiolabeled under mild reaction conditions and the resulting ^{89}Zr-complexes are adequately stable toward transchelation and transmetalation reactions as well as in sera. In spite of this, they need further investigation to validate the effective potential in immunoPET imaging applications.

5. ^{89}Zr-ImmunoPET studies

Therapy with monoclonal antibodies has proved a moderate safety profile due to their high specificity to antigens, consequently, the FDA has approved more than 95 mAbs and mAb-drug conjugates so far [98, 99].However, not all patients benefit from this kind of treatment because the response rate depends on the tumor antigen density, vascular penetration, and tissue distribution of each patient. To improve clinical benefit, it is necessary to select the drug with personalized dosing for the patient. ImmunoPET provides a direct reading of the antigen density and allows monitoring of mAb accumulation to improve mAb therapy. Therefore, this imaging technique is increasingly used in early-phase clinical trials today [100]. To obtain an optimal immunoPET image with low background retention that allows to correctly visualized and quantify

the concentration of the radiolabeled tracer, it is necessary to have a high specific uptake in the target tissue with minimal binding to the healthy organs and rapid clearance of the unbound tracer. Although generally high hepatic uptake has been found in healthy liver due to the normal hepatic catabolism of antibodies [98, 101].

^{89}Zr-immunoPET imaging has been mainly used to validate *in vivo* the target expression in cancer lesions and to study the biodistribution of biological drugs, such as cold therapeutic antibody, to improve drug delivery and consequently the clinical benefit for the patient [102]. Generally, ^{89}Zr-immunoPET studies are carried out labeling the intact mAbs directed against well-characterized antigens. Therefore, the goal of these studies is to select the patient for the therapy and predict his or her response to the treatment rather than target selection [99]. Usually, multiple time-point PET-imaging (from 1 to 7 days) is performed to optimize the acquisition protocols after a single tracer injection [1].

The first clinical trial with ^{89}Zr-immunoPET was reported in 2006 by Borjesson *et al.*, who treated patients with 74 MBq of ^{89}Zr-DFO-cmAb U36 to improve the detection of head and neck carcinoma [103]. The authors established that using ^{89}Zr-immunoPET it was possible to detect all primary tumors and most of the lymph node metastases, with a good performance comparable to those obtained with CT or MRI. Additionally, no adverse reactions were found. The effective dose calculated in women (0.66 +/- 0.03 mSv/MBq) and men (0.53 +/− 0.03 mSv/MBq) demonstrated that this ^{89}Zr-immunoPET agent can be safely used for tumor detection and for mAb-based therapy planning [104]. These encouraging results justify the growth of clinical studies based on ^{89}Zr-labeled mAbs [100].

Most of the ^{89}Zr-immunoPET agents have been developed by labeling FDA-approved mAbs, or that are currently being clinically studied for approval. The most important ^{89}Zr-agents used in clinical trials are listed below, and an overview of these agents can be found in Table 2, as well as the status of the antibody and the ^{89}Zr-immunoPET agent based on data from the clinicaltrial.gov website. Table2 also shows that all ^{89}Zr-agents were labeled using DFO as BFCA either via tetrafluorophenol-N-succinyldesferal (N-sucDFO) [105] or via p-isothiocyanatobenzyl-desferriox amine B (DFO-Bz-NCS) [106] that form, stable bonds with the lysine residues present in the proteins. The current radiolabeled strategy used in clinics relies on the reaction of the DFO derivatives with the ^{89}Zr-oxalate although, it has been suggested to replace it with ^{89}Zr-chloride since the latter has demonstrated to facilitate the synthesis of ^{89}Zr tracers for immunoPET with improved specific activity [107]. Radiolabeling of mAbs has been mainly done manually following the good-manufacturing-practice (GMP) guidelines production until now. However, a fully automated synthesis module for GMP-compliant production of ^{89}Zr-mAbs has been developed to minimize the radiation dose to the operator while increasing the robustness and capacity of production [108].

5.1. HER2 targeting

HER2 (human epidermal growth factor receptor-2) is an oncoprotein involved in the survival, proliferation, differentiation, angiogenesis, and metastasis of malignant cells. The overexpression of HER2 in many human tumors, including breast, ovarian, colon, stomach, and lung cancers, encourages the development of

anti-HER2 mAb to treat them [109]. Trastuzumab, the first humanized mAb approved by the FDA to target HER2-positive breast cancer, has significantly improved the patient's prognosis [8].

Dijker *et al.* performed a clinical trial in 14 patients with metastatic breast cancer using ^{89}Zr-trastuzumab and reported that it could detect previously known metastatic lesions and some that had been undetected earlier [110]. Authors found that the best time interval between the radiopharmaceutical administration and PET imaging was 4 to 5 days, and that the optimal dose to have a high tumor-to-background contrast was 50 mg (37 MBq) of ^{89}Zr-trastuzumab if the drug was used only for the PET imaging. They reported that the dose can be reduced to 10 mg for patients already on trastuzumab treatment, because the slow ^{89}Zr-trastuzumab hepatic elimination produced a higher blood concentration [110]. Lindstrom *et al.* reported that up to 15% of the patients with breast cancer experience a change in the HER2-expression during the period of tumor progression [111].Therefore, ^{89}Zr-trastuzumab imaging has demonstrated to be a useful tool to assess to distinguish HER2-positive from HER2-negative breast cancer, to characterize the HER2 status of the complete tumor burden in patients [112, 113], to support the clinical decision of anti-HER2 therapy and to guide individualized treatment [114].

Recently, Huisman *et al.* used mathematical modeling to determine the relation between target concentration and antibody tumor uptake. They found that initially, tumor

Table 2. Summary of ^{89}Zr-immunoPET agents used in oncologic clinical trials.

Target	Antibody	Trade Name	mAb Type	mAbs Status	^{89}Zr-immunoPET imaging agent	^{89}Zr-agent status	Tumor type	REF
CAI9.9	HuMab-5B1 (MVT-5873)	---	Human	Phase 1 and 2	^{89}Zr-DFO-HuMab-5B1	Phase 1	Pancreatic cancer	[115, 116]
Carbonic anhydrase-IX (CAIX)	Girentuxi-mab	Rencarex	Chimeric IgG1	FDA-approved	^{89}Zr-N-sucDFO-girentuximab	Phase 2 Phase 3	Renal Cell Carcinoma	[117-119]
CD20	Rituximab	MabThera Rituxan	Chimeric IgG1	FDA-approved	^{89}Zr-N-sucDFO-rituximab ^{89}Zr-DFO-BZ-NCS-rituximab	Phase 2 Phase 3	B cell lymphoma Orbital inflammatory disease Interstitial lung disease	[120-122] [123] [124, 125]
CD20	Ibritumomab-tiuxetan	Zevalin	Murine IgG1	FDA-approved	^{89}Zr-N-sucDFO-ibritumomab-tiuxetan	Complete	Non-hodgkins lymphoma	[91, 126]
CD44	RG7356 (RO5429083)	---	Humani-zed IgG1	Phase 1	^{89}Zr-N-sucDFO-RG7356	Phase 1	Solid tumors	[127, 128]
CD44v6	cmAb U36	---	Chimeric IgG1	---	^{89}Zr-N-sucDFO-cmAb U36	---	Head and neck cancer	[103, 104]
CD8	IAB22M2C	---	Minibody	Phase 1 and 2	^{89}Zr-DFO-BZ-NCS-IAB22M2C	Phase 2	Metastatic Solid Tumors	[129]
CEA/CD3	AMG 211	---	Bispecific T-cell engager (BiTE)	Phase 1	^{89}Zr-N-sucDFO-AMG 211	Phase 1	Gastrointestinal adenocarcinoma	[130]
EGFR	Cetuximab	Erbitux	Chimeric IgG1	FDA-approved	^{89}Zr-N-sucDFO-cetuximab	Phase 2	Head and neck Lung cancer Colorectal tumors	[131, 132] [132] [133-135]
EGFR	Panitumumab	Vectibix	Human IgG2	FDA-approved	^{89}Zr-DFO-BZ-NCS-panitumumab	Phase 1 Phase 2	Colorectal cancer	[136]

HER2	Pertuzumab	Omnitarg Perjecta	Humani-zed IgG1	FDA-approved	^{89}Zr-DFO-BZ-NCS-pertuzumab	Phase 1	Breast Cancer	[137, 138]
HER2	Trastuzumab	Herceptin	Humani-zed IgG1	FDA-approved	^{89}Zr-N-sucDFO-trastuzumab ^{89}Zr-DFO-BZ-NCS-trastuzumab	Phase 2	Breast Cancer Esophagogastric adenocarcinoma	[110, 112-114, 139, 140] [141]
HER3	GSK2849330	---	Humani-zed IgG1/IgG3	Phase 1	^{89}Zr-DFO-BZ-NCS-GSK2849330	Phase 1	Solid tumors	[142]
HER3	Lumretuzu-mab (RG7116)	---	Humani-zed IgG1	Phase 1	^{89}Zr-N-sucDFO-lumretuzumab	Phase 1	Multiple solid tumors	[143, 144]
Mesothelin	MMOT0530A	---	Humani-zed IgG1	---	^{89}Zr-N-sucDFO-MMOT0530A	Phase 1	Pancreatic cancer ovarian cancer	[145]
PD-1	Nivolumab	Opdivo	Human IgG4	FDA-approved	^{89}Zr-DFO-BZ-NCS-nivolumab	---	Non-small cell lung cancer	[146]
PD-L1	Atezolizumab	Tecentriq	Humani-zed IgG1	FDA-approved	^{89}Zr-N-sucDFO-atezolizumab	Not applicable	Breast cancer (triple-negative) Lung cancer (non-small cell) Bladder cancer	[147]
PSMA	huJ591	---	Humani-zed IgG1	Phase 2	^{89}Zr-DFO-BZ-NCS-huJ591	Phase 1 Phase 2	Prostate cancer	[148-150]
PSMA	IAB2M	---	Minibody	Phase 2	^{89}Zr-DFO-BZ-NCS-IAB2M	Phase 1 Phase 2	Prostate cancer Brain tumor	[151, 152] [153]
STEAP1	Vandortuzu-mab vedotin MSTP2109A	---	Humani-zed IgG1	---	^{89}Zr-N-sucDFO-MSTP2109A	Phase 1 Phase 2	Prostate cancer	[154, 155]
Growth factor-β (TGF-β)	Fresolimu-mab (GC1008)	---	Human IgG4	Phase 2	^{89}Zr-N-sucDFO-fresolimumab	Phase 2	High-grade Glioma	[156]
VEGF-A	Bevacizumab	Avastin	Humani-zed IgG1	FDA-approved	^{89}Zr-N-sucDFO-bevacizumab	Phase 1 Phase 2	Breast Cancer Neuroendocrine tumor Diffuse Intrinsic Pontine Glioma Von Hippel-Lindau Disease Non-small cell lung cancer Renal Cell Carcinoma	[157, 158] [159] [160, 161] [162] [163] [164, 165]

uptake increases with increasing target concentration, but at a high-administered mass dose of trastuzumab the value becomes constant. Based on this mathematical model, Huisman *et al.* concluded that false-positive findings differ in concordance with the cut-off used to define target positivity and the administered mass dose [166]. The first dosimetric study in adult women with positive HER2 breast cancer showed that about 12% of the injected dose of ^{89}Zr-trastuzumab is concentrated in the liver producing an absorbed dose of 1.54 mSv/MBq. However, because the effective dose produced by the administration of ^{89}Zr-trastuzumab was only 0.47 mSv/MBq and that no adverse effects were found, authors concluded that it can be considered a safe imaging agent [140]. Gaykema *et al.* also used ^{89}Zr-trastuzumab PET imaging to assess the alteration of HER2 expression in ten breast cancer (HER2+) patients after the anti-angiogenic application (inhibitor NVP-AUY922: HSP90), which can deplete client proteins like HER2 [158]. They found that the difference in ^{89}Zr-trastuzumab tumor uptake before and after HSP90 treatment can be used to monitor the modification of antigen expression and, consequently, to monitor the treatment response.

A Fab fragment of trastuzumab, which had been modified with the PASylation technology to increase its plasma half-life and consequently its tumor uptake, was labeled with ^{89}Zr to obtain molecular imaging of HER2+ tumors [167]. This first in-human study demonstrated that ^{89}Zr-HER2-Fab-PAS200 could identify lesions as early as 24 h post-injection due to its appropriate blood clearance, allowing sensitive visualization of small tumor lesions [167]. Trastuzumab has also been used to treat HER2-positive esophagogastric adenocarcinoma, but responses were poor due to the heterogeneity of HER2 expression and loss of HER2 expression while undergoing trastuzumab therapy. O'Donoghue *et al.*, assessed the HER2 status in 10 patients with primary and metastatic esophagogastric adenocarcinoma using ^{89}Zr-trastuzumab [141]. The authors found that ^{89}Zr-trastuzumab imaging was able to detect local and metastatic lesion in 80% of patients with optimal tumor visualization from 5 to 8 days after injection, demonstrating the feasibility of using this ^{89}Zr-agent to select patients with esophagogastric tumors who are likely to respond to HER2-directed treatment. Dosimetry studies of these patients indicted that the liver (1.37 mGy/MBq) and heart wall (1.12 mGy/MBq) received the highest doses, although no clinically significant toxicities were observed [141].

Pertuzumab is another mAb that targets HER2 but binds to a different site from that of trastuzumab. Ulaner conducted the first study of pertuzumab labeled with ^{89}Zr in six HER2-positive breast cancer patients to assess radiopharmaceutical safety [137]. ^{89}Zr-pertuzumab could detect multiple sites of malignancy, including HER2-positive brain metastases and lesion in patients who had previously received and were receiving HER2-targeted therapy, with optimal imaging from 5 to 8 days after administration. Dosimetry studies demonstrated an average effective dose of 0.54 mSv/MBq. Therefore, authors concluded that ^{89}Zr-pertuzumab is a safe agent for HER2-targeted imaging that could be employed in the clinic to evaluate the HER2 status of lesions. The same group recently demonstrated that ^{89}Zr-pertuzumab was helpful in successfully identifying metastases of breast cancer (HER2-positive) in cases where the primary tumor was HER2-negative [138].

5.2. EGFR targeting

Epidermal growth factor receptor (EGFR or HER1) is also implicated in the proliferation, differentiation, and survival of different cancer cell entities. EGFR was one of the first tyrosine kinase receptors for which the ligand binding mechanism was studied. Several antibodies have been developed as inhibitors of EGFR, including cetuximab and panitumumab [168].

Cetuximab is a chimeric EGFR mAb. Van Oordt *et al.* administered for the first time ^{89}Zr-cetuximab (10 mg, 37 Mbq) in ten patients with RAS wild type colorectal cancer after the first therapeutic dose of cetuximab, to evaluate the tumor uptake of the antibody by immunoPET imaging [135]. Authors found that ^{89}Zr-cetuximab had uptake in the tumor lesions in 6 out of 10 patients, of which 4 had positive response (^{89}Zr-cetuximab positive image in 3 of 4). However, Van Helden *et al.* reported that ^{89}Zr-cetuximab imaging unsuccessful predicted therapy benefit in cases of RAS wild-type colorectal cancer treated with cetuximab in the modality of monotherapy [134]. Dosimetric studies in seven patients with colorectal cancer, injected with ^{89}Zr-cetuximab after administration of a therapeutic dose showed an effective dose of 0.61 mGy/MBq

[133]. No toxicity was reported after the administration of up to 60 MBq of ^{89}Zr-cetuximab, even when high liver uptake was reported [132, 135]. ^{89}Zr-cetuximab was also used to predict the treatment response to cetuximab in 7 patients with locally advanced squamous cell carcinomas of neck and head (LAHNSCC). The results showed that ^{89}Zr-cetuximab uptake in LAHNSCC presented a wide interpatient variety. Nevertheless, the authors concluded that it could be used to predict treatment outcome [131].

Panitumumab, a fully-humanized mAb has also been labeled with ^{89}Zr-to calculate the maximum dosing for effective imaging in 3 patients with metastatic colon cancer [136]. Good-quality PET images were obtained after 5–7 days. Dosimetric studies after the injection of 37 MBq of ^{89}Zr-panitumumab showed that the organ with the highest absorbed dose was as usual the liver. However, ^{89}Zr-panitumumab showed a lower effective dose than ^{89}Zr-cetuximab [136].

5.3. HER3 targeting

HER3 has been described as a receptor with relatively weak kinase activity. HER3 is expressed in several carcinomas, its overexpression has been linked with a poor prognosis in multiple cancer subtypes, including breast, colorectal cancer, melanoma, cervical cancer, and ovarian cancer [169]. Consequently, HER3 has driven interest as a potential target for both imaging and therapy [142].

Lumretuzumab, also called RG7116, was the first humanized mAb reported to target HER3. This mAb was labeled with ^{89}Zr and administered in patients with HER3-positive metastatic and locally advanced solid tumors, to assess its kinetics and tumor uptake during lumretuzumab treatment [143]. ^{89}Zr-lumretuzumab demonstrated optimal PET imaging at 4 and 7 days after concomitant administration with 100 mg of unlabeled lumretuzumab [144]. Authors found specific uptake of labeled lumretuzumab in 19 of 20 patients with tumors. However, tumor tracer uptake decreased 4 days after injection, inter- and intra-patient heterogeneity was observed in lesions across the body and it was not possible to locate liver metastases due to high tracer uptake in the normal liver tissue [144].

GSK2849330, another anti-HER3 mAb, has been labeled by van Oordt *et al.* to study the biodistribution of ^{89}Zr-GSK2849330 and its dose-receptor occupancy relationship in 6 patients with advanced HER3-expressing solid tumors [142]. Authors demonstrated the utility of immunoPET to predict the therapeutic dose of GSK2849330 required for the saturation of HER3 receptor on tumor lesions in patients [142].

5.4. VEGF targeting

VEGFR (vascular endothelial growth factor receptor) and its ligand (VEGF) are involved in the regulation of many aspects of physiological and pathological angiogenesis. In particular, VEGF-A overexpression in some types of cancer has been related to the aggressiveness of the disease. Therefore, VEGF-A is considered an attractive target for angiogenic tumor therapy [8].

Bevacizumab is an FDA-approved mAb that targets all isoforms of VEGF-A. Gaykema *et al.* performed a pilot study in 23 patients using ^{89}Zr-bevacizumab imaging [157]. PET scans performed 4 days after the

radiopharmaceutical administration demonstrated ^{89}Zr-bevacizumab uptake in 25 of 26 breast tumors (range, 4–80 mm) showing high sensitivity (96%) for detecting primary breast cancer. The authors also found that the VEGF-A tumor expression was in agreement with the ^{89}Zr-bevacizumab tumor standard uptake value. Bahce *et al.* conducted another pilot study in seven patients to evaluate whether the VEGF-A tumor expression in NSCLC tumors could be quantified using ^{89}Zr-bevacizumab [163]. PET scanner performed on days 4 and 7 after ^{89}Zr-bevacizumab injection demonstrated that the radiopharmaceutical was uptake approximately four times more in tumor tissues than in healthy tissues. Additionally, Oosting *et al.* demonstrated that Hippel-Lindau disease (VHL) manifestations could be visualized using ^{89}Zr-bevacizumab, but with high heterogeneity in tracer accumulation [162]. Further studies carried out by Van Zanten *et al.* demonstrated that ^{89}Zr-bevacizumab tumor uptake was related with microvascular proliferation, therefore, it could be useful to identify intralesional heterogeneity [161].

Oosting *et al.* used ^{89}Zr-bevacizumab also to evaluate the therapeutic response of metastatic renal cell carcinoma after a bevacizumab/interferon antiangiogenic treatment [164]. The results demonstrated a high target tumor uptake with remarkable interpatient and intrapatient heterogeneity, which may reflect differences in vascular characteristics and tumor VEGF-A production. Jansen *et al.* used ^{89}Zr-bevacizumab imaging to investigate its uptake in children patients with glioma [160]. Results showed that ^{89}Zr-bevacizumab experienced uptake in 5 of 7 primary tumors, while no significant uptake was seen in the healthy brain. A considerable interpatient' heterogeneity was also found in drug delivery. ^{89}Zr-bevacizumab was predominantly concentrated within MRI contrast-enhanced areas. Authors reported a mean effective dose per patient of 0.9 mSv/MBq, and that 144 h after-injection was the optimal time to perform the PET-scan [160].

^{89}Zr-bevacizumab has also been used to study the effect of everolimus, an inhibitor that can reduce VEGF-A production, increasing the survival of patients with advanced neuroendocrine tumors (NETs) [159, 165]. PET scans demonstrated that ^{89}Zr-bevacizumab tumor uptake decreased in patients who received everolimus treatment [165].

5.5. CD20 targeting

B-cells overexpress CD20 in cases of hematopoietic malignant diseases, such as B-cell non-Hodgkin lymphoma (NHL), melanoma, and chronic lymphocytic leukemia. Therefore, several mAbs have been developed to treat B-cell-related malignancies and autoimmune disorders [99].

Radioimmunotherapy (RIT) is an option for the treatment of lymphomas due to their highly radiosensitive nature. ^{90}Y-ibritumomab tiuxetan is a monoclonal anti-CD20 for RIT of NHL (approved by the FDA). Since ^{90}Y is a pure β-emitter, a surrogate radionuclide must be used to predict the radiopharmaceutical biodistribution before ^{90}Y-ibritumomab tiuxetan treatment. Perk *et al.* labeled for the first time Zevalin (ibritumomab tiuxetan) with ^{89}Zr for the evaluation of ^{90}Y-Zevalin kinetics [91]. The results of their pilot study in a patient with NHL, showed clear uptake of ^{89}Zr-Zevalin in all tumor lesions detected by [^{18}F]FDG-PET imaging two weeks earlier. Therefore, the authors concluded that ^{89}Zr-Zevalin might be suitable for predicting ^{90}Y-Zevalin biodistribution in a myeloablative setting. Subsequently, Rizvi *et al.* used ^{89}Zr-

ibritumomab tiuxetan as theranostic pair of ^{90}Y-ibritumomab tiuxetan in seven patients with NHL. The authors concluded that ^{89}Zr-ibritumomab could be used to predict dose-limiting organ during radiotherapy [126].

A pilot study using ^{89}Zr-rituximab, another anti-CD20 mAb, was conducted in six patients with diffuse large B cell lymphoma expressing CD20 to assess the potential of this ^{89}Zr-mAb to target CD20 [122]. The results confirmed the ^{89}Zr-rituximab utility to guide personalized treatments. Muylle *et al.* performed dosimetric studies using ^{89}Zr-rituximab and PET/CT imaging showed that when ^{90}Y-rituximab was administered with unlabeled rituximab the radiation dose was similar for all patients, but when ^{90}Y-rituximab was administered alone, the dose in the spleen increased in two patients and consequently also increased the whole-body dose. These data suggest that the common practice of preloading with cold rituximab before RIT should be reconsidered [120].

In addition to hematological malignancies, ^{89}Zr-rituximab can be used to identify patients with rheumatoid arthritis who may respond to anti-B-cell therapies prior to treatment. Bruijnen *et al.* demonstrated that ^{89}Zr-rituximab is a promising agent for selecting and monitoring patients who respond to anti-B-cell therapies [121].

Adams *et al.* explored the possibility of visualizing CD20-expression in immune-mediated inflammatory lung diseases, as an early predictor of rituximab treatment response and demonstrated that ^{89}Zr-rituximab imaging in patients with therapy refractory interstitial pneumonitis is feasible, showing mediastinal lymph nodes and lung parenchyma uptake in some patients. However, lower uptake was found when 1000 mg rituximab preload was administered, suggesting that in the future studies should consider ^{89}Zr-rituximab imaging at low mAb dose before treatment with rituximab [124]. Adams group also used ^{89}Zr-rituximab imaging to explain why a one-third of patients with immune-mediated inflammatory disease with interstitial pneumonitis did not respond to rituximab therapy [125]. Clinical results showed that patients with no response presented a significantly greater splenic activity than did responding patients, suggesting a possible splenic mechanism in patients with immune-mediated inflammatory disease with interstitial pneumonitis that did not respond to rituximab treatment.

The potential of ^{89}Zr-rituximab PET/CT imaging for the diagnostic and therapeutic management of refractory orbital inflammation has also been evaluated by Laban *et al*, who demonstrated that this complex could be used to detect B cell-mediated disease within the orbital adnexal [123].

5.6. CD44 targeting

CD44 is another cell surface transmembrane glycoprotein overexpressed in many types of cancer and cancer stem cells. CD44 is an attractive therapeutic target because its overexpression has been associated with chemoresistance, tumor aggressiveness and metastatic potential, as well as tumor regrowth following standard therapy [170]. The v6 splice variant of CD44 (CD44v6), is predominantly expressed in squamous cell carcinoma. As already-mentioned, this was the first target used to detect primary tumors in the head and neck with ^{89}Zr-DFO-cmAb U36 by immunoPET [103]. Later, Van Oordt *et al.* label a recombinant anti-

CD44 IgG1 humanized mAb, called RG7356 with ^{89}Zr, to evaluate its biodistribution in 13 patients with solid tumors expressing CD44 [128]. The PET imaging showed that ^{89}Zr-RG7356 was efficiently accumulated in most lesions seen with FDG-PET, but also in the bone marrow, liver, and spleen, which could influence drug availability.

Target-mediated absorption in healthy tissues was assessed by Jauw *et al.* administering 1 mg of ^{89}Zr-RG7356 after a dose of unlabeled RG7356 (0 to 675 mg) to 13 patients with solid tumors expressing CD44 [127]. The authors calculated tracer uptake (tissue/blood relationship). They found that in a dose range from 1 to 450 mg, the tisuue/blood value decreased from organs such as the spleen, liver, bone marrow lung, and kidney indicating dose-dependent uptake. This demonstrated that immunoPET could be used to quantify, in healthy tissues, the dose-dependent uptake.

5.7. TGF-β targeting

Transforming growth factor–β (TGF-β) is a cytokine frequently expressed in malignant brain tumors that promote tumor growth, metastasis, angiogenesis, and immunosuppression inducing survival advantage of tumor cells [171]. Several types of TGF-β inhibitors have been developed as the fresolimumab mAb, which is capable of neutralizing all mammalian isoforms of TGF-β. Hollander *et al.* used for the first time ^{89}Zr-fresolimumab PET imaging to visualize and quantify fresolimumab uptake in twelve patients with glioma (high-grade, recurrent) [156]. PET imaging showed that ^{89}Zr-fresolimumab was capable to pass the blood–brain barrier and to reach the recurrent high-grade gliomas even though patients did not show benefit after fresolimumab treatment.

5.8. PSMA targeting

Prostate-specific membrane antigen (PSMA) is overexpressed in 95% of prostate cancers, up to 1,000 times more than in normal cells. It was reported that its expression levels increase in metastatic disease and in high-grade tumors [172]. Two PSMA mAbs have been developed so far, the 7E11, also known as capromab pendetide and the J591. 7E11 is a murine mAbs that binds to the intracellular domain of PSMA, exposed only after apoptosis or necrosis processes, so PET imaging of this antibody is not being studied. Instead, J591 is a humanized mAb also called huJ591.

Osborne *et al.* conducted the first pilot study in 11 patients to explore the feasibility of ^{89}Zr-huJ591 for locating prostate cancers [150]. They observed that intraprostate tumor foci could be identified using PET imaging, but only high-grade tumors were clearly visualized. The authors also found that there was a relationship between ^{89}Zr-huJ591 tumor uptake and tumor aggressiveness [150]. Pandit-Taskar *et al.* carried out a study in 10 patients with metastatic prostate cancer (mPC) to validate the use ^{89}Zr-huJ591 as an imaging biomarker for metastatic disease [148]. Patients were injected with 5 mCi of ^{89}Zr-huJ591 and scanned four times within 8 days to perform biodistribution and dosimetric studies. PET images showed higher accumulation of ^{89}Zr-huJ591 in bone and soft tissue lesions compared to conventional ^{99m}Tc-MDP and ^{18}FDG imaging modalities. Dosimetric studies demonstrated that the critical organs were liver and

kidney with an average absorbed dose of 7.7 and 3.5 cGy/mCi, respectively. A subsequent study of the same group in 50 patients with progressive metastatic castration resistant prostate cancers showed that ^{89}Zr-huJ591 was a superior target agent for bone lesions compared to ^{99m}Tc-MDP because, 491 osseous sites were detected *vs* 339 identified by bone scan. In contrast, the detection of soft-tissue lesions was suboptimal due to ^{89}Zr-huJ591 detected only 90 soft-tissue lesions vs 124 found by CT [149]. Authors reported that the best time for patient imaging was 7 days after injection [148].

Antibody fragments such as minibodies have been developed, to reduce the optimal detection time of lesions, from 6-7 days of the full antibody, to a few hours after injection. The genetically engineered 80-kDa minibody, IAB2M, obtained from the J591 antibody is an example. Pandit-Taskar *et al.* labeled IAB2M with ^{89}Zr and performed the first in human study, injecting 185 MBq of ^{89}Zr-IAB2M concomitant with cold IAB2M at total mass doses from 10 to 50 mg in 18 patients with mPC, to evaluate its biodistribution and kinetics [151]. They reported that ^{89}Zr-IAB2M showed favorable biokinetics and detection of metastases in soft-tissue and bone in patients with mPC. They a good lesion visualization within 48 h after ^{89}Zr-IAB2M injection. An increase in the dose of cold IAB2M caused slower serum clearance, but no significant reduction in liver uptake. Kinetic and dosimetric studies in 17 patients injected with 74MBq (10mg) ^{89}Zr-IAB2M indicated that the liver had the highest absorbed dose [152]. The mean biological half-life was 237 h and the average effective dose was 0.68 mSv/MBq.

PSMA expression has also been reported in the neovasculature endothelium of some tumors. Consequently, ^{89}Zr-IAB2M has been used in the imaging of other tumors, such as glioma and brain metastasis. [153].

5.9. STEAP1 targeting

The exact function of the six-transmembrane epithelial antigen of the prostate (STEAP1) has not been fully determined, it seems to be a transporter protein or an ion channel with specific functions in multiple biological processes such as intracellular communication, iron metabolism, and cell adhesion that allow tumor proliferation and invasiveness. STEAP1 is overexpressed in prostate cancer, so it has been proposed to use it as a biomarker for worse prognosis of prostate or for therapeutic intervention with mAbs or antibody-drug conjugates [75].

Carrasquillo *et al.* evaluated the possibility of detecting metastatic castration-resistant prostate cancer by PET/CT imaging in 19 patients using an ^{89}Zr-labeled STEAP1 mAb (MSTP2109A) [154]. The results showed that ^{89}Zr-DFO-MSTP2109A was specifically bound to numerous metastatic castration-resistant prostate cancers located in bone and soft tissue. However, there was no correlation between radiopharmaceutical uptake in the tumor and survival or STEAP1 expression determined by immunohistochemistry (IHC). Pharmacokinetic studies carried out in 6 patients showed a whole-body biological half-life of 469 h. Dosimetric assessments demonstrated that the radiation doses to normal organs were relatively high. However, the authors reported that by administering activities similar to those used in other studies (37 to 74 MBq) it would be possible to obtain adequate images by reducing the radiation dose to normal organs [155].

5.10. Mesothelin targeting

Mesothelin (MSLN) is a membrane surface glycoprotein overexpressed by epithelial tumors such as mesothelioma, ovarian cancer, and pancreatic carcinoma, while its expression is minimal in healthy cells including mesothelial cells lining pleura, peritoneum and pericardium surface [173, 174].

Lambert *et al.* labeled for the first time an MSLN antibody called MMOT0530A with ^{89}Zr and carried out a first-in-human study injecting it in patients with ovarian and pancreatic cancer [145]. The first two patients received ^{89}Zr-labeled antibody (37 MBq, 1mg) with no additional unlabeled antibody and were imaged on days 2, 4, and 7 post-injection. The next 9 patients received the same amount of labeled antibody concomitant with unlabeled MMOT0530A. The authors found that the biological half-life of ^{89}Zr-MMOT0530A in the first group was shorter than in the second group, because higher tracer concentrations reduce antibody blood clearance. Biodistribution studies demonstrated that ^{89}Zr-MMOT0530A was uptake in blood, kidneys, spleen, and intestine; however, the organ with the highest concentration was the liver in which unlike the other organs the uptake increased over time. PET scanning showed that most tumor lesions had maximum uptake 4 days after tracer injection, and that ^{89}Zr-MMOT0530A tumor uptake did not correlate with IHC determined MSLN expression.

5.11. PD-1 and PD-L1 targeting

Programmed death receptor (PD1) is localized in the T-cells and over-expressed upon programmed cell death, while its ligand 1 (PD-L1) is an inhibitor of the immunity [175]. The PD-1/PD-L1 complex allows evasion of immune response by cancer cells, acting as an inhibitor of the killing effect of T-cells. To block this checkpoint and produce a therapeutic effect, several mAbs against PD-L1 have newly been developed as durvalumab, atezolizumab and avelumab [99]. However, PD-L1 block therapy suffers from a low response rate, and the reason is still unclear [176].

Atezolizumab has been labeled with ^{89}Zr by Bensch *et al.* to assess the feasibility of predicting patients' response to PD-L1 block therapy using PET imaging [147]. These authors carried out a PET imaging study in humans with ^{89}Zr-atezolizumab in patients with three types of tumors, prior treatment with atezolizumab. They found that tumor uptake was heterogeneous but high, varying among patients and tumor entities. Furthermore, it was found that the PET signal was also high in lymphoid tissues and at sites of inflammation. Despite this, the results showed that patient's clinical responses and progression free survival were better correlated with the pretreatment PET signal than with IHC, showing that PET images could be used to assess the status of PD-L1 and predict clinical response.

It has also been proposed that the combination of anti-PD-L1 PET imaging with IHC of tumor biopsies could help quantify PD-1 levels [177]. Several mAbs against PD-1, such as nivolumab, cemiplimab and pembrolizumab, have also been developed, but among them only nivolumab has been labeled with ^{89}Zr. Niemeijer *et al.* used ^{89}Zr-nivolumab as a biomarker for the quantification of PD-1 in non-small cell lung cancer, prior to nivolumab treatment [146]. This first study in humans showed heterogeneous uptake of ^{89}Zr-

nivolumab in the tumors that correlates with the heterogeneity of PD-1 expression in lymphocytic aggregates determined by IHC. Therefore, ^{89}Zr-nivolumab proved to be a feasible and safe biomarker for non-invasive quantification of the PD-1 expression in humans. However, authors reported that more extensive studies are needed to validate these results.

5.12. CA19-9 targeting

Carbohydrate antigen 19–9 (CA19-9) is normally in blood circulation, however, its expression in the pancreatic tumor is several orders of magnitude greater. Consequently, CA19-9 is currently used for predicting pancreatic tumor stage, response to therapy and resectability, as well as overall survival. Hence, a fully human IgG1 mAb that specifically binds to the CA 19–9 antigen, called HuMab-5B1, was developed and labeled with ^{89}Zr. The first in human study, conducted by Lohrmann *et al*., in nine patients injected with 171 MBq of ^{89}Zr-HuMab-5B1, demonstrated that labeled-mAb was accumulated in known local recurrences, lymph node, lung, peritoneal and bone metastases from the second day after injection, increasing over time and reaching the best visualization on day 7 [115].^{89}Zr-HuMab-5B1 biodistribution was characterized by relatively high liver and spleen uptake, with very low concentration in other parenchymal tissues. However, it was found that increasing the mass of cold antibody concomitant administered can reduce liver and spleen uptake, with the consequent decrease in the dose absorbed by these organs [116]. Based on these results, authors concluded that ^{89}Zr-HuMab-5B1 PET/CT imaging demonstrated promising results for the detection of tumors expressing the CA 19-9 antigen. However, to evaluate the accuracy of this imaging modality, additional studies that correlate the imaging findings with histopathology should be performed [115].

5.13. CAIX targeting

Carbonic anhydrase IX (CAIX) is a cell surface antigen mainly associated to the hypoxia regulation. CAIX showed limited expression in normal tissue, but it is present in 95% of ccRCC (clear cell renal cell carcinoma)[178].

It has been demonstrated that girentuximab, a chimeric anti-CAIX mAb, can be labeled with ^{89}Zr to assess CAIX expression *in vivo*. Hekman *et al.* conducted the first clinical study using ^{89}Zr-girentuximab for the diagnosis of ccRCC. The authors found that PET imaging was useful to confirm suspected recurrent or metastatic ccRCC and to guide clinical decisions in 16 patients with localized disease [119]. They also realized that all resected PET-positive primary lesions were effectively ccRCC. Therefore, authors concluded that ^{89}Zr-girentuximab is useful to guide clinical decision in ccRCC cases. Additionally, Verhoeff, *et al.* reported that combined ^{89}Zr-girentuximab PET/CT and CT detected more lesions than the combined FDG-PET/CT scan, or CT scan alone (91% versus 84% and 56% respectively) [118]. Merkx *et al.* showed with a dosimetric study in 10 patients that it is possible to obtain a good quality PET/CT image for a quantitative evaluation of patients with suspected ccRCC by administration of 10 mg (37 Mbq) of ^{89}Zr-girentuximab, this radiopharmaceutical dose was safe and well-tolerated [117].

5.14. FAP targeting

Cancer-associated fibroblasts (CAF) are being widely studied as potential therapeutics aimed at inhibiting cancer progression and metastasis by reducing immunosuppression and remodeling the tumor microenvironment [179]. The subpopulation of particular interest is CAF-S1, the only one that expresses the fibroblast activation protein (FAP), which participates in the promotion of tumor invasiveness by degradation of the extracellular matrix, among other functions associated with the carcinogenesis. It has been reported that the main role of radiotracers directed molecularly at FAP is not to displace metabolic molecular imaging (FGD-PET), but to function as a complement for an adequate prognostic evaluation in different types of solid tumors [180].

The ^{89}Zr-DFO-mAb F19 (anti-FAP) complex has been reported as a potential radiotracer for immunoPET in the evaluation of metastatic castration-resistant prostate cancer (mCRPC), where the highest tumor uptake of ^{89}Zr-DFO-mAb F19 is reached at 3 days post-administration. Based on the reported results, the authors propose the combination of anti-FAP immunotherapy along with the application of cytotoxic drug conjugates as an alternative for the treatment of mCRPC [181, 182].

6. Antibody-drug conjugates

Antibody-drug conjugates (ADCs) use highly specific mAb to selectively deliver potent cytotoxic drugs to cancer cells with great effectiveness, therefore, it is one of the fastest growing cancer therapeutic techniques in the last decade [183]. However, to guarantee the efficacy of ADCs in targeting solid tumors, it is necessary to confirm the antigen expression in the tumor before the treatment [184]. Molecular imaging has proven to be a good option to predict ADCs efficacy, however, using this approach is necessary to radiolabel the ACD or the corresponding “naked” mAb, demonstrating that the radiolabeled antibody presents a similar biodistribution and metabolism than the studied ACDs. Only two ^{89}Zr-labeled agents have been used in the clinic to study ADC performance so far. Gebhart *et al.* used immunoPET imaging with ^{89}Zr-trastuzumab for the first time to determine the patient’s eligibility for T-DM1 breast cancer treatment. T-DM1 is a HER2-targeted ADC in which trastuzumab is used to deliver DM1 (emtansine), a very potent cytotoxin that induces the death of proliferating cells by inhibiting polymerization of tubulin [139]. They found that pretreatment imaging was useful in improving understanding of tumor heterogeneity, as well as in predicting patient response and selecting those who have the greatest potential to benefit from T-DM1 treatment. As was mentioned above, Lambert *et al*. were the first to label the MSLN antibody (MMOT0530A) with ^{89}Zr to predict the efficacy of DMOT4039A agent, which contains MMOT0530A bound to the cytotoxic agent MMAE [145]. They used the ^{89}Zr-MMOT0530A to study the mesothelin expression in patients with pancreatic and ovarian cancers, to determine whether there was any relationship between tumor uptake and response to DMOT4039A treatment. ^{89}Zr-MMOT0530A was useful to visualize 17 pancreatic and 20 ovarian cancer lesions, the results of the patient-based analysis showed that the IHC score correlated with the tumor uptake. However, no correlation was found between PET imaging and treatment response after 2 cycles of DMOT4039A evaluated by CT.

7. ^{89}Zr-nanoparticles

The use of nanoparticles (NPs) in medicine has grown exponentially, due to the development of new materials with advantageous properties, such as their large surfaces that can be multi-functionalized by reducing the toxicity and increasing the stability and bioavility of some drugs. NPs also offer the opportunity of specific drug delivery and selective tissues/organs targeting, taking advantage of the specific localization (ligand-mediated) and enhanced permeability and retention (EPR) effect, which allows the passive accumulation in solid tumors through fenestrated blood vessels derived from the physio-pathological tumor environment. Consequently, different type of NPs has been developed and functionalized to obtain active target nanomaterials. Figure 11 shows the simplified scheme of some of the most commonly used structures and their applications.

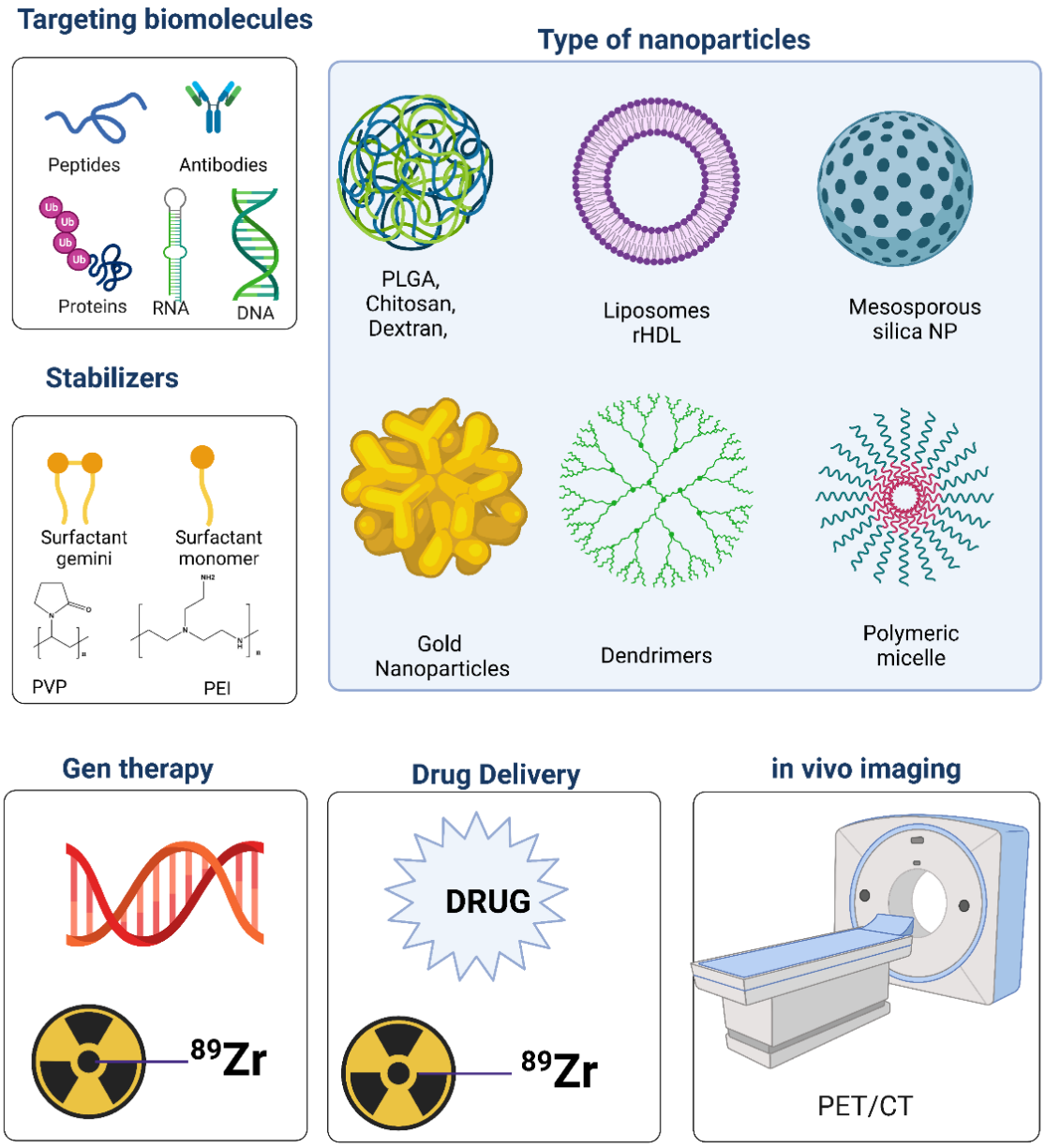

Figure 11. Simplified scheme of some of the most commonly used nanoparticle, delivery and applications

Most of these nanomaterials have been labeled with ^{89}Zr to be used in the field of imaging. Silica cores nanomaterials have been labeled primarily using chelator-free strategies, because it has been demonstrated that silica NPs can chelate a range of isotopes with good radiolabeling yields and short reaction times [185-187]. In this connection, Chen *et al* demonstrated that mesoporous silica nanoparticles (MNS) can be directly labeled with $^{89}Zr^{4+}$ exploiting the deprotonated silanol groups (-Si-O$^-$) and ^{89}Zr-MNS presented long stability *in vivo* (< 20 days) [188]. Other chelator-free radiolabeling methods such as modification of particle surface or binding $^{89}Zr^{4+}$ to the coating, physisorption, encapsulation, or radiochemical doping have also been successfully used to label NPs [189-191]. However, it was also found that the use of chelating agents could increase the labeling yield of nanoconstructs [189, 190]. DFO is the most common chelating agent used for the radiolabeling of NPs, although it is not to the most stable (see Table 3). Recently, intrinsically radiolabeled NPs (chelator free radiolabeling) have been used to overcome the shortcoming of ^{89}Zr-DFO instability this strategy was applied to MNS and manganese oxide NPs. ^{89}Zr-nanoconstructs proved to be useful for obtaining images of drug delivery and melanoma localization respectively [188, 213].

^{89}Zr-radiolabeled NPs such as ultra-small superparamagnetic iron-oxide nanoparticles (USPION), liposomes, high-density lipoproteins and polysaccharides as dextran, chitosan and Poly (lactic-co-glycolic acid) (PLGA) have been designed and enabled for macrophage imaging and quantification, as they allow the diagnosis of several disorders such as cancer, aortic aneurysm, atherosclerosis, or myocardial infarction [192, 199, 207-209, 215]. Macrophage imaging is possible due to ^{89}Zr-NPs being internalized by these cells by two main mechanisms, phagocytosis and receptor-mediated micropinocytosis. However, the disadvantage of using radiolabeled NPs for this application is the increase in the radiation dose to the bone marrow, due to the presence of macrophages in this tissue [215].

Nanoparticles can also be functionalized with specific biomolecules to reach a particular receptor on the membrane cell or a specific tissue/organ. Several molecules such as folic acid (FA) [185], octreotide [206], or RGD (Arg-Gly-Aspartic Acid) [186] have been attached to their surface for tumor targeting (see Table 3). In addition, the possibility of orthogonal functionalization of NPs allows the incorporation of two or more targeting molecules or drugs which makes possible the preparation of targeted multimodal theranostic nanostructures useful for imaging drug delivery. These multifunctional nanoplatforms are a convenient option in the treatment of tumor masses with a reduced antigen-protein expression on cancer cells, due to their multi-functionalization and high tumor retention (EPR effect) that increase the therapeutic effect produced by the traditional single target immunotherapy [216]. Similarly, the possibility of orthogonal functionalization of NPs allows the incorporation of fluorescent dyes to prepare multimodal-imaging nanoconstructs [208].

Table 3. Preclinical studies for ^{89}Zr-radiolabeled nanoparticles.

Imaging modality	NP type	Coating or targeting molecule	Radiolabeling (RL) procedure and labeling efficiency (LE)	Size (nm) and z potential (ζ)	Applications and phase	Ref.
PET/CT PET/OI	Liposomes ^{89}Zr-CLL, ^{89}Zr-SCL DiIC@^{89}Zr-SCL	PEG	*Click labeling* (L-DBCO + ^{89}Zr-PEG$_4$-DFO; overnight 30 °C); LE 14%. *Chelator based RL*; 1. DFO Surface conjugation; 2. Zr(Ox)$_2$ PBS, pH 7, 4h 40°C; LE 80%	106 108	Quantitative macrophage imaging. Preclinical: xenograft and orthotropic 4T1 breast cancer.	[192]
PET	Liposomes ^{89}Zr-DFO, ^{89}Zr-DFO-PEG1k ^{89}Zr-DFO-PEG2k		*Chelator based RL*: 1. DFO surface conjugation; 2. ^{89}Zr(Ox)$_2$, Na$_2$CO$_3$ (2 M), HEPES (0.5 M, pH 7.4), pH 7, RT, 1 h. LE > 68%.	116 114 120	Pharmacokinetics comparison. Preclinical: Her2(+) NDL neu deletion transgenic mice.	[193]
PET	Silica (S) NPs ^{89}Zr-STF-1 to ^{89}Zr-STF-5 T=TPP; F=FA	TPP FA	*Chelator-free RL*: Si-O$^-$ groups; ^{89}Zr(Ox)$_2$, HEPES (0.1 M, pH 7.5), 37 or 75 °C, 2 h. LE > 82%.	100-111	Tumor targeting. Preclinical: CT-26 murine colon carcinoma xenograft.	[185]
PET	^{89}Zr-Melanine NPs	Melanine	*Chelator-free RL*: melanine groups; ^{89}Zr(Ox)$_2$, pH 5, 37°C, 0.5 h; PD10 purification; LE 98%.	7 ~ 60 kDa	Iron overload therapy. Preclinical: iron overload mice; intra venous *iv* administration.	[194]
PET	Iron Oxide Nanoclusters ^{89}Zr-IONC@PEI ^{89}Zr-IONC@PVP	PEI PVP	*Chelator-free RL:* Hydrothermal reaction; ^{89}ZrCl$_4$, Na$_2$CO$_3$ (0.1 M), pH 7, 140 °C, 24 h. LE > 90%.	140	Tumor targeting. Preclinical: CT-26 tumor bearing mouse, *iv* administration.	[195]
PET	Dendrimers ^{89}Zr-DFO-DNPS, ^{89}Zr-DNPS	PAMAM Dendrimer No targeting molecule	*Chelator based RL:* ^{89}Zr-DFO-Bz-NCS surface conjugation; 37°C, 2 h. *Chelator-free RL:* ^{89}ZrCl$_4$, PBS, 37°C, 2 h. LE none	192.6 90.3	Scaffold for drug delivery and imaging. Preclinical: CT-26 and MDA-MB-231 human breast adenocarcinoma bearing mice; *iv* administration.	[196]
-	HA NPs ^{89}Zr@HA	HA	*Chelator-free RL:* ^{89}Zr sorption on HA, RT 0.5 h.	Length 100 Width: 25	*In vitro* evaluation as HA NPs as a promising ^{89}Zr carrier. Preclinical: *no in vivo studies*	[197]
PET	Cerium Oxide NPs ^{89}Zr-CONPs	DT10-NH$_2$, DT10-PEG, DT10-SB, PAA	*Chelator-free RL:* Intrinsic core radiolabeling (co-precipitation); ^{89}ZrCl$_4$, RT, 24 h.	60.2 81.9 80.5 80.0	For further design on NPs. Preclinical: healthy and colon tumor bearing C57BL/6 mice; *i.v.* administration.	[198]
PET/CT	Ab-Gold NPs [^{89}Zr]Zr-5B1-AuNP	5B1 Antibody	*Chelator based RL:* ^{89}Zr-DFO-Bz-NCS-Ab surface conjugation. LE 30-35%	34.86 (PDI: 0.27) ζ 21.3 mV	Pretreatment with clodronate liposomes to deplete macrophages; Preclinical: CA19.9(+) BxPC-3 ortothopic pancreatic tumor bearing mice.	[199]
PET	Chitosan NPs ^{89}Zr-loaded chitosan NPs	PTPP	*Chelator-free RL:* ^{89}Zr(Ox)$_2$, RT, 0.75 h. LE<70%	343 ζ 46 mV	Monitoring white blood migration, *in vivo* inflammation, infectious/inflammatory sites. Therapeutic strategy. Preclinical: human leukocyte cells	[200, 201]
PET/CT	Lipoplex NPs containing DNA	Gemini surfactant/DOPE	*Chelator based RL:* 1. DFO surfactant surface conjugation; 2. ^{89}Zr(Ox)$_2$, Na$_2$CO$_3$ (2 M), HEPES (3 M), pH 7, 37°C, 1 h. LE 95%.	111–117 nm ζ 31-33 mV	Radiolabeled DNA delivery system. Preclinical: A375 melanoma xenograph athymic CD-1 mice.	[202]

Imaging modality	NP type	Coating or targeting molecule	Radiolabeling (RL) procedure and labeling efficiency (LE)	Size (nm) and z potential (ζ)	Applications and phase	Ref.
PET/MRI	Superparamagnetic iron oxide NPs ^{89}Zr-DFO-Bz-NCS-Fe_3O_4@TiO2	-----	*Chelator based RL:* 1. DFO surface conjugation; 2. $^{89}Zr(Ox)_2$, pH 7, RT, 1 h. LE 95%.	50-89	Potential for photodynamic therapy and hyperthermia. Preclinical: *no in vivo studies*.	[203]
PET/MRI	USPIONs ^{89}Zr-DFO-Ferumoxytol ^{89}Zr-Ferumoxytol	Polyglucose sorbitol carboxymethylether	*Chelator based RL*: 1. DFO surface conjugation; 2.$^{89}Zr(Ox)_2$, pH 7, 37°C, 1 h. LE 95%. *Chelate free RL*: Heat-induced radiolabeling; $^{89}Zr(Ox)_2$/$^{89}ZrCl_4$ 120 °C 1h. LE 82-96%	17-31	Lymph node imaging. Preclinical: female healthy C57BL/6 and transgenic Hi-Myc mice with invasive prostate adenocarcinoma mouse colon cancer.	[204, 205]
PET/MRI	Gadolinium paramagnetic NPs ^{89}Zr-Gd-Pegylated liposome	PEG Octreotide	*Chelate free RL:* Heat-induced radiolabeling; $^{89}ZrCl_4$, 45 °C, 2h. LE none.	–	Tumor targeting. Preclinical model: C6 glioma bearing Nu/Nu mice	[206]
PET/MRI	^{89}Zr labeled dextran or hyaluronan NPs	Dextran	*Chelator based RL*: 1. DFO surface conjugation; 2. $^{89}Zr(Ox)_2$, Na_2CO_3 (2 M), pH 7, RT, 2 h. LE 95%.	13	Inflammation, macrophage detection in atherosclerotic plaques. Preclinical CT-26 colon xenograph mouse model	[207] [208]
PET	^{89}Zr-DFO-apoA-I@rHDL ^{89}Zr-DSPE-DFO@rHDL	Apo A-I	*Chelator based RL*: 1. DFO surface conjugation; 2. $^{89}Zr(Ox)_2$, Na_2CO_3 (1 M), pH 7, 37 °C, 2 h. LE 94% and 74%	8.9 8.6 MW~150 kDa	Quantitative tumor-associated macrophages. Preclinical mice bearing orthotropic 4T1 breast cancer.	[209]
PET	^{89}Zr-WS_2/WO_x (0.4) PEG nanodot	PEG	*Chelator Free RL*: Heat-induced radiolabeling, $^{89}Zr(Ox)_2$, HEPES (0.5 mM), pH 7, 75 °C 2h. LE 98%	15	Tumor imaging *in vivo* mapping of draining lymph nodes. Preclinical: 4T1 breast cancer bearing mice (*iv* and regional administration).	[210]
PET	AuNP-PPAA-Cetuximab-^{89}Zr ^{89}Zr-DFO-Bz-NCS-cetuximab	PPAA Cetuximab	*Chelator based RL*: ^{89}Zr-DFO-Bz-NCS-cetuximab surface conjugation.	31	EGFR targeting Potential theranostic purposes. Preclinical: A431epithelial carcinoma bearing mice.	[211]
PET	^{89}Zr-anti-CD105-AuNPs-PPAA	Anti-CD105 Ab PPAA	*Chelator based RL*: ^{89}Zr-DFO-Bz-NCS-antiCD105 Ab surface conjugation. LE 75%.	102	Antiangiogenic therapy Preclinical: B16F10-luc melanoma xerograph C57BL/6J mice.	[212]
PET	Mesosporus silica (MS) NPs	–	*Chelator Free RL*: Si-O^- groups; $^{89}Zr(Ox)_2$, HEPES , pH 7-8, 37 °C 2 h. LE 82%	~150 ζ 48.4 mV	Imaging, red blood cell trafficking, drug delivery. Preclinical CT-26 xerograph Balb/c mice, i.v. administration.	[188]
PET/MRI	Manganese Oxide NPs [^{89}Zr]Mn_3O_4@PEG	PEG	*Chelator Free RL*: Heat-induced radiolabeling; $^{89}Zr(Ox)_2$, HEPES (0.5 mM), pH 7-8, 75 °C 0.5 h. LE 78%.	10 ζ 3.7 mV	Lymph Node Mapping Preclinical: healthy Balb/c mice, *i.v.* and regional administration.	[213]

Imaging modality	NP type	Coating or targeting molecule	Radiolabeling (RL) procedure and labeling efficiency (LE)	Size (nm) and z potential (ζ)	Applications and phase	Ref.
PET/CT MRI	^{89}Zr-ferucarbotran ^{89}Zr-perimag-COOH	Dextran	*Chelator Free RL*: Heat-induced radiolabeling; $^{89}Zr(Ox)_2$, Na_2CO_3 (1 M), 100 °C, 1 h. LE none	127	Prolonged SPION half-life circulation time by means fucoidan. Preclinical: GL261 glioma bearing C57BL/6 mice, *i.v.* administration.	[214]
PET	Hollow Mesoporous silica Rm-^{89}Zr-HMSNs	CD47 of red blood cell membrane	*Chelator Free RL*: Si-O$^-$ groups; $^{89}Zr(Ox)_2$/$^{89}ZrCl_4$ HEPES pH 7.5, RT 24h. LE 96%	150 ζ−18.6 mV	Tumor imaging by avoiding phagocytosis; Preclinical: CT-26 tumor xenograph mice, *i.v.* administration.	[187]
PET/OI	^{89}Zr-cRGDY-PEG-C′dot ^{89}Zr-DFO-cRGDY-PEG-C′dot	PEG cRGDY	*Chelator Free RL*: Si-O$^-$ groups; $^{89}Zr(Ox)_2$, HEPES, pH 8, 75 °C, 1 h. LE 50% *Chelator based RL*: 1. DFO surface conjugation; 2. $^{89}Zr(Ox)_2$, HEPES, pH 8, 37 °C, 1 h. LE 98%.		Melanoma Imaging. Preclinical: M21 M21L melanoma xerograph mice, *i.v.* administration.	[186]

CLL (click-labeled liposomes); SCL (surface chelation liposomes); DiIC (1,1-diododedyl-3,3,3,3-tetramethyl-indodicarbocyanine-5,5-disulfonic acid, Dye Cy-5); DBCO (dibenzoazacyclooctyne); p-NCS-Bz-DFO (p-isothiocyanatobencyl-desferrioxamine B); dye DiIC12(5)-DS (1,1-diododecyl-3,3,3,3-tetramethyl-indodicarbocyanine-5,5-disulfonic acid); PEG (polyethylenglycol); PTPP (pentasodium tripolyphosphate); TPP (triphenylphosphonium);FA (folic acid); PEI (polyethyleneimine); PVP (polyvinilpirrolydone), D-DNPS (p-NCS-Bz-DFO-PAMAM Dendrimer); PAMAM (polyamidoamine); DNPS (PAMAM Dendrimer), HA, (hydroxyapatite, $Ca_{10}(PO_4)_6(OH)_2$); DT10-NH_2 (dextran T10 amine); DT10-PEG (dextran T10 polyethylene glycol); DT10-SB (dextran T10 sulfobetaine); rHDL (reconstituited high-density lipoprotein); PAA (polyacrilic acid); DOPE (1,2-dioleoyl-sn-glycerolo-3-phpsphoethanolamine); apoA-I (apolipoprotein A-I); PL (phospholipid); DSPE (1,2-distearoyl-sn-glycero-3-phosphoethanolamine-N–[carboxylic acid (polyethyleneglycol)-2000]); PPAA (plasma polymerized allylamine); cRGDY (cyclo(Arg-Gly-Asp-Dtyr-CyS) peptide.

Table 3 summarized the chemical-physical properties and the proposed applications of ^{89}Zr-tagged nanoparticles under preclinical evaluation. The clinical translation of zirconium radiolabeled NPs has just started as demonstrated by the first human imaging of high-density lipoprotein (HDL) labeled with ^{89}Zr to target SB-R1 (scavenger receptor B1) in esophageal cancer patients. The ^{89}Zr-HDL administration was safe and the tumor uptake was higher at 72 h [217].

However, it is important to note that despite the rapid advances in preclinical research in this field in recent years, due to the numerous functionalization possibilities of nanoconstructs labeled with ^{89}Zr, the clinical data reported are minimal because it is necessary to improve the reproducibility of the functionalization and labeling techniques used before they can be transferred to clinical research.

8. Cell tracking with ^{89}Zr

Over the last few years, cell-based immunotherapy has shown great potential for treating several diseases, such as diabetes and cancer. Despite their promising results, very few cellular products have been translated into clinical practice so far, because to obtain a successful cell therapy, it is necessary to better understand the precise dosage, time, and spatial distribution. Non-invasive imaging, such as nuclear imaging can help to achieve this goal, by real-time tracking *in vivo* the cells, to predict, monitor and evaluate the treatment [218, 219].

Cell-based immunotherapy approaches can be classified into two main groups, the first group does not need genetic engineering for its effectiveness such as the adoptive cell therapies using natural killer (NK) or T cells, stem cell therapies and tumor infiltrating lymphocytes. The second group fundamentally requires genetic engineering to be efficient such as the chimeric antigen receptor T (CAR T) cells and tumor-antigen-specific T cell receptors (TCR) [220].

8.1. Labeling of non-genetic engineering cells

Initially, only nongenetic engineering cells were radiolabeled with ^{89}Zr using ^{89}Zr(oxinate)$_4$, also called ^{89}Zr-oxine (Figure 12). This is a neutral and lipophilic compound formed by an eight-coordinated metal center in a distorted dodecahedral geometry [221]. Due to its high lipophilic character, Zr-oxine is capable of spreading freely through the cell membrane allowing a rapid cell accumulation (Figure 13) [222, 223]. Charoenphun *et al.* used for the first time ^{89}Zr-oxine to direct label human leukocytes and three cell lines (murine myeloma cells (eGFP-5 T33), breast cancer cells (MDA-MB-231), and murine macrophages (J774)). The labeling efficiency obtained ranged from 40 % to 61%, cell retention of ^{89}Zr was from 91% at 24 h and cell viability was higher than 90% [222].

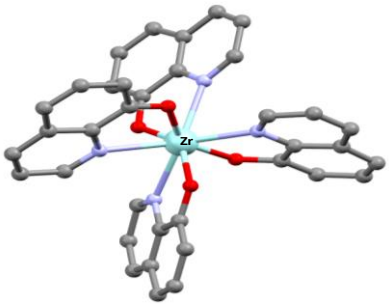

Figure 12. Crystal structure of Zr-oxine

Sato *et al.* labeled activated cytotoxic T lymphocytes and dendritic cells by incubation with ^{89}Zr-oxine [224]. Authors found lower labeling efficiency than Charoenphun *et al.* (from 13% to 44%), but similar high stability with 83% of ^{89}Zr retention in the cells after 5 days. In this study, it was also demonstrated that radioactivity concentration up to 555 kBq/5x10^6 cells enabled extended cell tracking for 7 days in mice using a MicroPET/CT scanner, without affecting their viability or functionality. Man *et al.* used also ^{89}Zr-oxine to label and track *in vivo* Gammadelta-T (γδ-T) cells, one of the best options in oncology for adoptive immunotherapy due to their tumor infiltration abilities, cytotoxicity, and antigen presenting properties [225]. *In vitro* studies demonstrated that ^{89}Zr-labeled γδ-T cells, with a radioactivity concentration up to 20 mBq/cell, retained their proliferative capacity, viability, as well as anti-cancer cytotoxicity and showed minimal DNA damage. Preclinical *in vivo* studies in breast cancer demonstrated that ^{89}Zr-γδ-T cells were able to target the tumors, moreover when tumor antigen expression was increased also the ^{89}Zr signal in the tumors significantly improved. The authors proved that it was possible to track ^{89}Zr-tagged cells over a week by PET imaging [225]. Sato *et al.* also used ^{89}Zr-oxine to label the adoptive NK cells to track their biodistribution in rhesus macaques by PET imaging [226]. The authors did not report the labeling efficiency or cell radioactivity concentrations but showed that ^{89}Zr-labeled NK cells retained enough radioactivity to be tracked and quantified *in vivo* for 7 days. They confirmed that the labeling procedure did not alter cellular phenotype, viability, or function. Additionally, authors reported low organ radio-exposures and no clinical side effects observed in treated animals. Consequently, they concluded that this tagging method could be used to develop new techniques to improve the location of immune cells in tumor microenvironments, which could be easily translated to humans [226].

Bansal *et al.* used for the first time ^{89}Zr-deferoxamine-NCS (^{89}Zr-DFO-NCS) to label directly 3 different kinds of cells (mouse-derived melanoma, dendritic cells and human mesenchymal stem cells) and demonstrated that radioactivity concentrations up to 0.5 MBq/10^6 cells do not affect the cellular viability or proliferation. Label cells showed high stability *in vitro* and *in vivo*, no efflux was observed for over 7 days post labeling, however, the cell labeling efficiency obtained was low to moderate (from 30% to 50%) depending on cell type [218].

Very recently, Friberger *et al.* optimized the synthesis of both ^{89}Zr-DFO-NCS and ^{89}Zr-oxine radiotracers and performed a direct comparison of the cell labeling efficiency, although the two complexes present different cell tagging mechanisms (Figure 13) [227]. ^{89}Zr-DFO-NCS binds to the protein lysine on the cell membrane surface and was not internalized by the cells in contrast, ^{89}Zr-oxine complex forms a hydrophobic sphere that can passively diffuse across the cell membrane, where the oxine molecules liberate ^{89}Zr, which

unspecific binding to the cytoplasmic components. The authors found that optimization of radiotracer syntheses resulted in an increase cell labeling efficiency of ^{89}Zr-DFO-NCS and ^{89}Zr-oxine to 70% and 64% respectively, which confirmed that ^{89}Zr-labeling in both cases not significantly affected the cell viability or proliferation rate. They concluded that ^{89}Zr-oxine was a better agent for cell labeling due to its higher stability, greater cellular retention, and minimal variation between cell types [227]. Lechermann *et al.* labeled T cells by incubation with different concentrations of ^{89}Zr-oxine to estimate the limit for PET imaging detection [228]. They seeded labeled cell suspensions into 6-well plates and scanned them (PET/CT and PET/MRI), using a specific activity of 27.8 kBq/10^6 cells. Results using this *in vitro* model showed that 6.8×10^4 was the minimal number of labeled cells needed to obtain PET imaging.

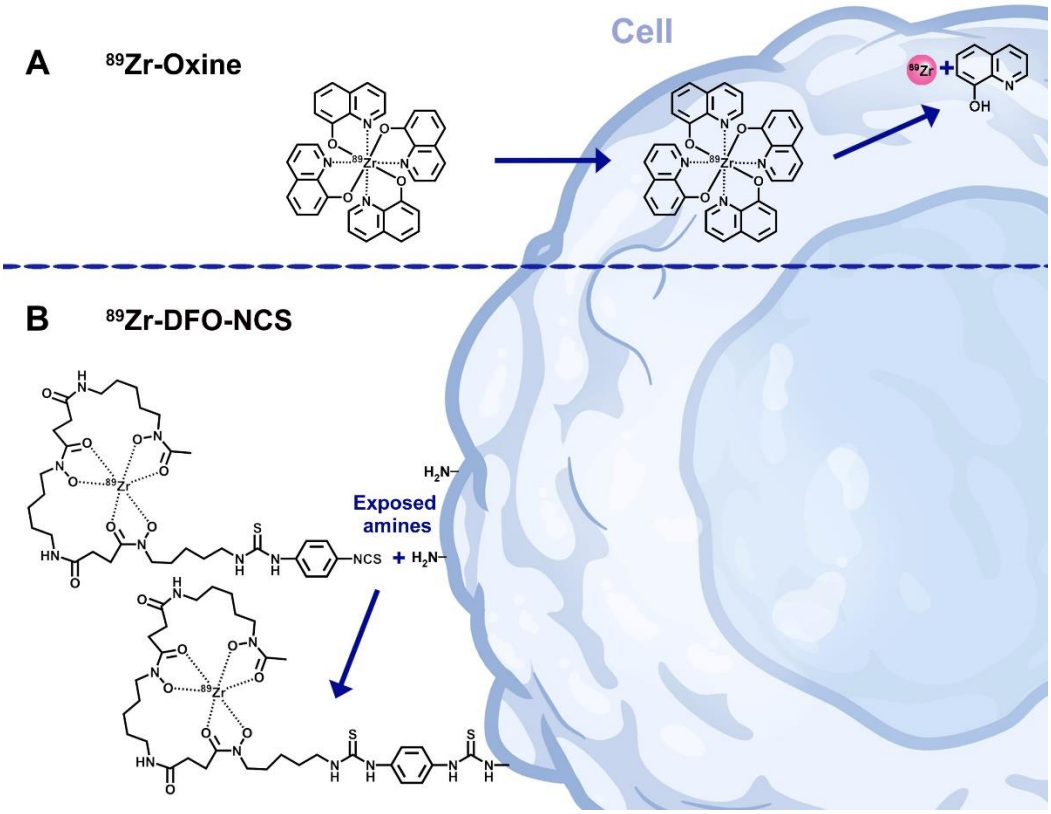

Figure 13. Cell labeling mechanisms. A) labeling with ^{89}Zr-oxine, which passively diffuse across the cell membrane and B) shows the schematic representation of extracellular labeling with ^{89}Zr-deferoxamine-NCS that binds to protein lysine on the cell membrane.

The technique of specific labeling with antibodies has also been used to obtain labeled cells. Nobashi *et al.* used as a target the costimulatory molecule OX40, which participates in eliminating cancer cells and is mainly expressed in activated effector T cells [229]. A mAb against OX40 was labeled by incubation with ^{89}Zr-DFO for 60 min at 37 °C, afterward the product was purified. Then ^{89}Zr-DFO-OX40 was injected into mice bearing glioma with activated T cells to quantify and track the response to immunotherapy by PET imaging. These results demonstrated that immunoPET imaging of ^{89}Zr-labeled OX40 was useful to monitor T-cell activation with high specificity [229]. CD8-positive T cells, which are important for initiating and mediating a response to checkpoint inhibitors such as anti-PD-1/PD-L1, were also site-specifically-labeled

with antibodies. Pandit-Taskar *et al.* used the IAB22M2C minibody with high affinity for human CD8, to label *in vivo* CD8-positive T cells [129]. In this first-in-humans prospective study, six cancer patients received 111 MBq of ^{89}Zr-IAB22M2C with different minibody mass doses (range from 0.2 to 10 mg). Results proved that the radiolabeled antibody was well tolerated, and no side effects were observed. The PET images of the patients showed that the spleen had always the highest radioactive uptake, however, the biodistribution in other organs changed depending on the mass of the administered minibody. The uptake in tumor lesions was observed in images from 2 h after administration, attesting that ^{89}Zr-IAB22M2C has a favorable kinetics for early imaging of CD8-positive T cell–rich tissues. However, authors state that it was impossible to establish the differences in lesion uptake among minibody mass doses due to the small number of patients and the variability in tumor types [129].

8.2. Labeling of genetic engineering cells

Immune cells obtained from genetic engineering, such as CAR T and TCR, have also been radiolabeled to be tracked. CAR T cell therapy is a promising clinical approach that combines the intracellular signaling components of the T cell receptor with the target specificity of antibodies [230]. Thanks to their successful results reducing tumor progression, CAR T were the first commercially approved engineered cellular products for the hematologic malignancies treatment [231]. However, the safety of this cell therapy has always been a concern due to its severe adverse effects as it requires a dynamic quantitative tracking to improve the understanding of cellular behavior after adoptive transfer, as well as the optimization of infusion time and dose to avoid potential lethal systemic toxicity [219]. Weist *et al.* were the first to assess radioactivity retention, viability, and functionality of human-derivate CAR T cells labeled with ^{89}Zr-oxine [230]. *In vitro* studies demonstrated a high labeling efficiency (75%) with more than 60% of ^{89}Zr retained in the cell after 6 d. *In vivo* tracking of two CAR T cell lines (interleukin-13 receptor α2-targeted and PSCA-targeted) labeled with ^{89}Zr (specific activity of 70 kBq/10^6 cells), in tumor mouse models, demonstrated that cells maintained their cytokine production, migration, and tumor cytotoxicity. Based on these results, the authors concluded that ^{89}Zr-oxine was a clinically translatable platform for the assessment of cell therapies [230]. Maria *et al.* labeled huLym-1-A-BB3z-CAR T cells to be used in Raji lymphoma [232] using the method reported by Weist *et al.* [230] obtaining a high labeling efficiency but lower ^{89}Zr cell retention (33.5%). To explain this result, authors suggested that different CAR constructs could produce differences in label retention [232]. Intravenous administration of escalating doses of CAR T cells results in a dose dependent. Simultaneous PET/MRI imaging at different time points after administration of labeled CAR T-cells in tumor bearing mice showed that CAR T cells are confined in the lung (3–5 h) and after cells move to the liver and spleen (2-3 d). These data could be the cause of cell inactivation before targeting tumors, a low tumor accumulation of CAR T cells, and no tumor regression [232]. Wu *et al.* labeled CD19 CAR T with ^{89}Zr-oxine to study the pharmacokinetic and pharmacodynamic in human leukemic xenograft mouse models [233]. Their results were quite like those previously reported, CAR T cells were successfully labeled without affecting their viability and proliferation and showed high ^{89}Zr retention (>80%). No visual differences were found between radiolabeled CAR T cell uptake in CD19 positive and negative tumors, although Patlak's modelling analysis revealed higher specific uptake in CD19-positive cells that result in tumor suppression

after CD19 CAR T treatment. Authors report that this cell tracking method has the limit that it can only reveal the migration, distribution, and homing of parental cells *in vivo*, and cannot be used to see cell activation, proliferation, or death [233]. To facilitate the translation of PET images for cell tracking in clinical diagnosis and cell-based therapy, Man *et al.* [234] developed the first single-step kit formulation for a rapid, stable, high-performance cell labeling using ^{89}Zr-oxine and Massicano *et al.* [235] described a detailed production of ^{89}Zr-oxine to label cells under US Pharmacopeia standard.

Lee *et al.* labeled Jurkat/CAR and human peripheral blood mononuclear CAR T-cells using ^{89}Zr-desferrioxamine-NCS with a specific activity of 103.6 kBq/10^6 cells, reaching a labeling efficiency of up to 79% [236]. The *in vitro* test demonstrated cell viability higher than 95% and no significant decrease in cell proliferation after labeling. However, PET imaging and *ex-vivo* studies did not show a significant accumulation of radioactivity in tumors, labeled cells were first confined in the lung and progressively cells moved to the spleen-liver, very similar results to those previously reported by Maria *et al.* [232].

Simonetta *et al.* selected a costimulatory molecule up-regulated during T-cell activation (ICOS) as the target to label CD19 CAR T cells with an antibody-based method [233]. Anti-ICOS mAb labeled with ^{89}Zr-DFO was intravenously injected 5 days after T-cell administration in lymphoma tumor-bearing mice, to track CAR T-cell *in vivo*. The authors found that at tracer doses, ICOS-targeting antibody did not interfere with CAR T-cell function. However, the high uptake of ^{89}Zr-DFO-Anti-ICOS in vascularized organs as the heart, liver, and spleen, limited the sensitivity of this method to detect tumor sites, so it was not possible to differentiate between mice treated with CAR T cells and mice not treated by PET/CT images. The authors state that this limitation could be solved using smaller vectors such as antibody fragments, minidodies, or nanobodies; consequently, they concluded that this molecular imaging approach could easily be applicable to the clinical setting because it does not require the *ex vivo* labeling [237].

The use of CAR T cell therapy for solid tumors is more difficult because detect only surface tumor-associated antigens [220]. Additionally, the high variability in density and antigen presentation, as well as the difficulty for cells to migrate inside the tumors, help to evade CAR T cells. To expand the number of potential tumor-specific antigens, constructs encoding a TCR that recognizes the major histocompatibility antigen (MHC–antigen) complexes have been developed and introduced into T cells [231]. These TCR T cells also present the advantage of producing lower maximum cytokine levels with high antigen density, compared with some CAR T cells that produce high cytokine levels that may even be life-threatening.

Mall *et al.* developed the ^{89}Zr-aTCRmu-F(ab')2 radiotracer with high stability and immunoreactivity. ^{89}Zr-aTCRmu-F(ab')2 targets a murine sequence introduced in the human TCR (TCRmu) [238, 239]. It was demonstrated that the radiolabeled antibody could directly target TCR without any effect on the functionality of transgenic T cells. PET-imaging in a human myeloid sarcoma model revealed high sensitivity within the tumor [238].

9. Perspectives and conclusions

Tumors are pathological structures constituted of cancer cells and the tumor microenvironment. The latter includes cells communicated through dynamic networks regulated by acellular factors, such as inflammatory enzymes, cytokines, chemokines, growth factors, and extracellular matrix components. The vital role of cells and proteins associated with the tumor stroma and cancer cells is receiving extensive attention in the field of cancer biology. Thus, current anticancer therapies are focused on inhibiting cancer progression, metastasis, and therapeutic resistance by reducing immunosuppression and remodeling the tumor microenvironment. In particular, the immunotherapeutic pathway has been used with distinct agents, such as radioimmunoconjugates, oncolytic viruses, vaccines, and nanoparticles. In this context, ^{89}Zr has demonstrated, for most immunotherapeutic modalities, its usefulness to form stable ^{89}Zr-immune-complexes able to detect, in time and space, changes in the phenotype of different cancer entities. Such changes are essential for defining patients' treatment based on the expression or suppression of proteins involved in the disease. Therefore, the future of ^{89}Zr-immune-complexes, particularly those based on Zr-DFO analogs, holds promise for PET imaging of a broad class of immunotherapeutics directed against specific and dynamic molecular targets. For example, fibroblasts associated with colon, ovarian, breast, pancreatic, and lung cancer express the programmed death ligand (PD-L1), which bind to the receptor PD-1 expressed by T cells to inhibit their activity and reduce antitumor immunity. On the other hand, cancer-associated fibroblasts (FAP+) are a significant source of CXCL12 secretion, which induces immunosuppression. Therefore, the administration of an inhibitor of CXCR4 (a CXCL12 receptor) could improve the accumulation of T cells and act synergistically with anti-FAP and anti-PD-L1 immunotherapies to slow down the progression of cancer, where ^{89}Zr-DFO-anti-FAP and ^{89}Zr-DFO-anti-PD-L1 immunoPET could follow-up the molecular processes associated with the prognosis, treatment definition, and response to the combined therapy.

In the paper, we have hoped to provide a detailed overview on the recent achievements in ^{89}Zr-based PET imaging field, with studies ranging from radionuclide production to basic metal coordination chemistry, from ongoing clinical trials to new application trends. However, despite the many successes, much work has to be done and emphasis should be placed on three main points. The synthesis and evaluation of novel chelators that allow a fast coordination kinetics, under mild reaction condition suitable to label biomolecules with high thermodynamic/kinetic stability, in order to minimize the *in vivo* release of the $^{89}Zr^{4+}$ and its bone accumulation. In fact, although a number of acyclic and cyclic BFCA have been recently investigated, DFO still remains the most used chelator for ^{89}Zr-based PET imaging. It is currently utilized to tag different vectors with ^{89}Zr including protein derivatives, nanoconstructs, and live cells. The development of mild and site-specific strategies for the bioconjugation of BFCA to targeting vector. In this connection, the utilization of enzymatic methods is promising. The extension of ^{89}Zr-PET imaging from antibodies to other targeting vectors with suitable pharmacokinetics (e.g. NPs and live cells) to involve new application in medical areas.

Aknoledgements Authors thanks the International Atomic Energy Agency (CRP 2223

F22071) and Associazione Italiana per la Ricerca sul Cancro (AIRC) IG 2020 ID 24528.

Conflicts of Interest: “The authors declare no conflict of interest.”

References

[1] J. Boers, E.F.J. de Vries, A. Glaudemans, G.A.P. Hospers, C.P. Schroder, Application of PET Tracers in Molecular Imaging for Breast Cancer, Current Oncology Reports, 22 (2020) 16.

[2] F. Cortezon-Tamarit, A. Baryzewska, M. Lledos, S.I. Pascu, Zirconium-89 radio-nanochemistry and its applications towards the bioimaging of prostate cancer, Inorg. Chim. Acta, 496 (2019).

[3] L. Melendez-Alafort, P.C. Muzzio, A. Rosato, Optical and Multimodal Peptide-Based Probes for In Vivo Molecular Imaging, Anti-Cancer Agents in Medicinal Chemistry, 12 (2012) 476-499.

[4] E.T. Sarcan, M. Silindir-Gunay, A.Y. Ozer, N. Hartman, Zr-89 as a promising radionuclide and it's applications for effective cancer imaging, J. Radioanal. Nucl. Chem., 14.

[5] B.A. Gulec, F. Yurt, Radiopharmaceuticals developed for Zr-89-Immuno-PET, J. Radioanal. Nucl. Chem., 13.

[6] L.E. McInnes, S.E. Rudd, P.S. Donnelly, Copper, gallium and zirconium positron emission tomography imaging agents: The importance of metal ion speciation, Coord. Chem. Rev., 352 (2017) 499-516.

[7] M.M. Alauddin, L.A. Khawli, Advances in Immuno-PET for the Detection of Cancer and Assessment of Response to Therapy, Curr. Med. Chem., 28 (2021) 647-672.

[8] Y.W.S. Jauw, C.W. Menke-van der Houven van Oordt, O.S. Hoekstra, N.H. Hendrikse, D.J. Vugts, J.M. Zijlstra, M.C. Huisman, G. van Dongen, Immuno-Positron Emission Tomography with Zirconium-89-Labeled Monoclonal Antibodies in Oncology: What Can We Learn from Initial Clinical Trials?, Front. Pharmacol., 7 (2016) 15.

[9] R. Mikolajczak, N.P. van der Meulen, S.E. Lapi, Radiometals for imaging and theranostics, current production, and future perspectives, J. Label. Compd. Radiopharm., 62 (2019) 615-634.

[10] J. Notni, H.J. Wester, Re-thinking the role of radiometal isotopes: Towards a future concept for theranostic radiopharmaceuticals, J. Label. Compd. Radiopharm., 61 (2018) 141-153.

[11] ICRP 2008. Nuclear Decay Data for Dosimetric Calculations, ICRP Publication 107, 38 (2008).

[12] T.K. Nayak, M.W. Brechbiel, Radioimmunoimaging with Longer-Lived Positron-Emitting Radionuclides: Potentials and Challenges, Bioconjugate Chem., 20 (2009) 825-841.

[13] M. Conti, L. Eriksson, Physics of pure and non-pure positron emitters for PET: a review and a discussion, EJNMMI Phys., 3 (2016) 17.

[14] J.P. Holland, Y.C. Sheh, J.S. Lewis, Standardized methods for the production of high specific-activity zirconium-89, Nucl. Med. Biol., 36 (2009) 729-739.

[15] IAEA, Production of Zirconium-89 and the Development of Zr-89 Radiopharmaceuticals, https://www.iaea.org/projects/crp/f22071, (Accessed January 17, 2022).

[16] S.A. Kandil, I. Spahn, B. Scholten, Z.A. Saleh, S.M.M. Saad, H.H. Coenen, S.M. Qaim, Excitation functions of (alpha,xn) reactions on Rb-nat and Sr-nat from threshold up to 26 MeV: Possibility of production of Y-87, Y-88 and Zr-89, Appl. Radiat. Isot., 65 (2007) 561-568.

[17] M. Sadeghi, M. Enferadi, M. Bakhtiari, Accelerator production of the positron emitter zirconium-89, Ann. Nucl. Energy, 41 (2012) 97-103.

[18] F.T. Tarkanyi, A.V. Ignatyuk, A. Hermanne, R. Capote, B.V. Carlson, J.W. Engle, M.A. Kellett, T. Kibedi, G.N. Kim, F.G. Kondev, M. Hussain, O. Lebeda, A. Luca, Y. Nagai, H. Naik, A.L. Nichols, F.M. Nortier, S.V. Suryanarayana, S. Takacs, M. Verpelli, Recommended nuclear data for medical radioisotope production: diagnostic positron emitters, J. Radioanal. Nucl. Chem., 319 (2019) 533-666.

[19] IAEA Nuclear Data Sevices: Medical Radioisotopes Production, https://www-nds.iaea.org/relnsd/vcharthtml/MEDVChart.html, (Accessed February 11, 2022).

[20] N. Amjed, A.M. Wajid, N. Ahmad, M. Ishaq, M.N. Aslam, M. Hussain, S.M. Qaim, Evaluation of nuclear reaction cross sections for optimization of production of the important non-standard positron emitting radionuclide Zr-89 using proton and deuteron induced reactions on Y-89 target, Appl. Radiat. Isot., 165 (2020) 9.

[21] M.G. Mustafa, H.I. West Jr, H. Obrien, R.G. Lanier, M. Benhamou, T. Tamura, Measurements and a direct-reaction plus hauser-feshbach analysis of Y89(p,n)89Zr, Y89(p,2n)88, and Y89(p,pn)88Y reactions up to 40 MeV, Physical Review C, 38 (1988) 1624-1637.

[22] H.M. Omara, K.F. Hassan, S.A. Kandil, F.E. Hegazy, Z.A. Saleh, Proton induced reactions on Y-89 with particular reference to the production of the medically interesting radionuclide Zr-89, Radiochim. Acta, 97 (2009) 467-471.

[23] S. Manenti, F. Haddad, F. Groppi, New excitation functions measurement of nuclear reactions induced by deuteron beams on yttrium with particular reference to the production of Zr-89, Nucl. Instrum. Methods Phys. Res. Sect. B-Beam Interact. Mater. Atoms, 458 (2019) 57-60.

[24] J. Zweit, S. Downey, H.L. Sharma, PRODUCTION OF NO-CARRIER-ADDED ZIRCONIUM-89 FOR POSITRON EMISSION TOMOGRAPHY, Appl. Radiat. Isot., 42 (1991) 199-201.

[25] Y. Tang, S.T. Li, Y.Y. Yang, W. Chen, H.Y. Wei, G.Q. Wang, J.J. Yang, J.L. Liao, S.Z. Luo, N. Liu, A simple and convenient method for production of Zr-89 with high purity, Appl. Radiat. Isot., 118 (2016) 326-330.

[26] A. Kasbollah, P. Eu, S. Cowell, P. Deb, Review on production of 89Zr in a medical cyclotron for PET radiopharmaceuticals, Journal of Nuclear Medicine Technology, 41 (2013) 35-41.

[27] S.L. Queern, T.A. Aweda, A.V.F. Massicano, N.A. Clanton, R. El Sayed, J.A. Sader, A. Zyuzin, S.E. Lapi, Production of Zr-89 using sputtered yttrium coin targets, Nucl. Med. Biol., 50 (2017) 11-16.

[28] H. Skliarova, S. Cisternino, G. Cicoria, M. Marengo, E. Cazzola, G. Gorgoni, V. Palmieri, Medical cyclotron solid target preparation by ultrathick film magnetron sputtering deposition, Instruments, 3 (2019).

[29] S. Cisternino, E. Cazzola, H. Skliarova, J. Amico, M. Malachini, G. Gorgoni, U. Anselmi-Tamburini, J. Esposito, Target manufacturing by Spark Plasma Sintering for efficient 89Zr production, Nucl. Med. Biol., 104-105 (2022) 38-46.

[30] G.M. Dias, C.F. Ramogida, J. Rousseau, N.A. Zacchia, C. Hoehr, P. Schaffer, K.S. Lin, F. Bénard, 89Zr for antibody labeling and in vivo studies – A comparison between liquid and solid target production, Nucl. Med. Biol., 58 (2018) 1-7.

[31] M.K. Pandey, T.R. Degrado, Cyclotron Production of PET Radiometals in Liquid Targets: Aspects and Prospects, Current Radiopharmaceuticals, 14 (2021) 325-339.

[32] M.K. Pandey, A. Bansal, H.P. Engelbrecht, J.F. Byrne, A.B. Packard, T.R. DeGrado, Improved production and processing of 89Zr using a solution target, Nucl. Med. Biol., 43 (2016) 97-100.

[33] M.K. Pandey, H.P. Engelbrecht, J.F. Byrne, A.B. Packard, T.R. DeGrado, Production of Zr-89 via the Y-89(p,n) Zr-89 reaction in aqueous solution: Effect of solution composition on in-target chemistry, Nucl. Med. Biol., 41 (2014) 309-316.

[34] M.V. Zheltonozhskaya, V.A. Zheltonozhsky, E.N. Lykova, A.P. Chernyaev, V.N. Iatsenko, Production of Zirconium-89 by photonuclear reactions, Nucl. Instrum. Methods Phys. Res. Sect. B-Beam Interact. Mater. Atoms, 470 (2020) 38-41.

[35] B.I. Intorre, A.E. Martell, Zirconium Complexes in Aqueous Solution. I. Reaction with Multidentate Ligands, Journal of the American Chemical Society, 82 (1960) 358-364.

[36] B.J. Intorre, A.E. Martell, Aqueous Zirconium Complexes. II. Mixed Chelates, Journal of the American Chemical Society, 83 (1961) 3618-3623.

[37] E.W. Price, C. Orvig, The Chemistry of Inorganic Nuclides (86Y, 68Ga, 64Cu, 89Zr, 124I), in: L. John Wiley & Sons (Ed.) The Chemistry of Molecular Imaging, 2014, pp. pp. 105–135, ISBN 978-101-118-85475-85474.

[38] N.B. Bhatt, D.N. Pandya, T.J. Wadas, Recent Advances in Zirconium-89 Chelator Development, Molecules, 23 (2018).

[39] P.J. Blower, A nuclear chocolate box: The periodic table of nuclear medicine, Dalton Transactions, 44 (2015) 4819-4844.

[40] D. Brasse, A. Nonat, Radiometals: Towards a new success story in nuclear imaging?, Dalton Transactions, 44 (2015) 4845-4858.

[41] S. Heskamp, R. Raave, O. Boerman, M. Rijpkema, V. Goncalves, F. Denat, Zr-89-Immuno-Positron Emission Tomography in Oncology: State-of the-Art Zr-89 Radiochemistry, Bioconjugate Chem., 28 (2017) 2211-2223.

[42] E.W. Price, B.M. Zeglis, J.S. Lewis, M.J. Adam, C. Orvig, H6phospa-trastuzumab: Bifunctional methylenephosphonate-based chelator with 89Zr, 111In and 177Lu, Journal of the Chemical Society. Dalton Transactions, 43 (2014) 119-131.

[43] T.I. Kostelnik, C. Orvig, Radioactive Main Group and Rare Earth Metals for Imaging and Therapy, Chem. Rev., 119 (2019) 902-956.

[44] A.I. Pozhidaev, M.A. Porai-Koshits, T.N. Polynova, Crystal structure of zirconium ethylenediaminetetraacetate tetrahydrate, Journal of Structural Chemistry, 15 (1974) 548-553.

[45] A.B. Ilyukhin, R.L. Davidovich, I.N. Samsonova, L.V. Teplukhina, Eightfold-coordinated diethylenetriaminepentaacetates: Crystal structures of K[M(Dtpa)] · 3H2O (M = Zr, Hf) and NH4[Sn(Dtpa)] · H2O, Kristallografiya, 45 (2000) 45-49.

[46] D.N. Pandya, N. Bhatt, H. Yuan, C.S. Day, B.M. Ehrmann, M. Wright, U. Bierbach, T.J. Wadas, Zirconium tetraazamacrocycle complexes display extraordinary stability and provide a new strategy for zirconium-89-based radiopharmaceutical development, Chemical Science, 8 (2017) 2309-2314.

[47] D.N. Pandya, K.E. Henry, C.S. Day, S.A. Graves, V.L. Nagle, T.R. Dilling, A. Sinha, B.M. Ehrmann, N.B. Bhatt, Y. Menda, J.S. Lewis, T.J. Wadas, Polyazamacrocycle Ligands Facilitate Zr-89 Radiochemistry and Yield Zr-89 Complexes with Remarkable Stability, Inorg. Chem., 59 (2020) 17473-17487.

[48] C. Bolzati, B. Spolaore, Enzymatic Methods for the Site-Specific Radiolabeling of Targeting Proteins, Molecules, 26 (2021).

[49] J.P. Holland, Predicting the Thermodynamic Stability of Zirconium Radiotracers, Inorg. Chem., 59 (2020) 2070-2082.

[50] R. Imura, H. Ida, I. Sasaki, N.S. Ishioka, S. Watanabe, Re-Evaluations of Zr-DFO Complex Coordination Chemistry for the Estimation of Radiochemical Yields and Chelator-to-Antibody Ratios of Zr-89 Immune-PET Tracers, Molecules, 26 (2021) 13.

[51] K.L. Summers, E.K. Sarbisheh, A. Zimmerling, J.J.H. Cotelesage, I.J. Pickering, G.N. George, E.W. Price, Structural Characterization of the Solution Chemistry of Zirconium(IV) Desferrioxamine: A Coordination Sphere Completed by Hydroxides, Inorg. Chem., 59 (2020) 17443-17452.

[52] M. Patra, A. Bauman, C. Mari, C.A. Fischer, D. Häussinger, G. Gasser, T.L. Mindt, An octadentate bifunctional chelating agent for the development of stable zirconium-89 based molecular imaging probes, Chemical Communications, 50 (2014) 11523-11525.

[53] H. Cho, N. Al-Saden, H. Lam, J. Mobus, R.M. Reilly, M.A. Winnik, A comparison of DFO and DFO* conjugated to trastuzumab-DM1 for complexing Zr-89 - In vitro stability and in vivo microPET/CT imaging studies in NOD/SCID mice with HER2-positive SK-OV-3 human ovarian cancer xenografts, Nucl. Med. Biol., 84-85 (2020) 11-19.

[54] T. Richardson-Sanchez, W. Tieu, M.P. Gotsbacher, T.J. Telfer, R. Codd, Exploiting the biosynthetic machinery of Streptomyces pilosus to engineer a water-soluble zirconium(IV) chelator, Organic & Biomolecular Chemistry, 15 (2017) 5719-5730.

[55] M. Brandt, J. Cowell, M.L. Aulsebrook, G. Gasser, T.L. Mindt, Radiolabelling of the octadentate chelators DFO* and oxoDFO* with zirconium-89 and gallium-68, Journal of Biological Inorganic Chemistry, 25 (2020) 789-796.

[56] M. Briand, M.L. Aulsebrook, T.L. Mindt, G. Gasser, A solid phase-assisted approach for the facile synthesis of a highly water-soluble zirconium-89 chelator for radiopharmaceutical development, Dalton Transactions, 46 (2017) 16387-16389.

[57] C.J.M. Brown, M.P. Gotsbacher, R. Codd, Improved Access to Linear Tetrameric Hydroxamic Acids with Potential as Radiochemical Ligands for Zirconium(iv)-89 PET Imaging, Australian Journal of Chemistry, 73 (2020) 969-978.

[58] S.E. Rudd, P. Roselt, C. Cullinane, R.J. Hicks, P.S. Donnelly, A desferrioxamine B squaramide ester for the incorporation of zirconium-89 into antibodies, Chemical Communications, 52 (2016) 11889-11892.

[59] A. Noor, J.K. Van Zuylekom, S.E. Rudd, P.D. Roselt, M.B. Haskali, E.D. Yan, M. Wheatcroft, R.J. Hicks, C. Cullinane, P.S. Donnelly, Imaging Somatostatin Positive Tumors with Tyr(3)-Octreotate/Octreotide Conjugated to Desferrioxamine B Squaramide Radiolabeled with either Zirconium-89 or Gallium-68, Bioconjugate Chem., 32 (2021) 1192-1203.

[60] M. Chomet, M. Schreurs, M.J. Bolijn, M. Verlaan, W. Beaino, K. Brown, A.J. Poot, A.D. Windhorst, H. Gill, J. Marik, S. Williams, J. Cowell, G. Gasser, T.L. Mindt, G. van Dongen, D.J. Vugts, Head-to-head comparison of DFO* and DFO chelators: selection of the best candidate for clinical(89)Zr-immuno-PET, Eur. J. Nucl. Med. Mol. Imaging, 48 (2021) 694-707.

[61] E. Berg, H. Gill, J. Marik, A. Ogasawara, S. Williams, G. van Dongen, D. Vugts, S.R. Cherry, A.F. Tarantal, Total-Body PET and Highly Stable Chelators Together Enable Meaningful Zr-89-Antibody PET Studies up to 30 Days After Injection, J. Nucl. Med., 61 (2020) 453-460.

[62] D.L. White, P.W. Durbin, N. Jeung, K.N. Raymond, Specific sequestering agents for the actinides. 16. synthesis and initial biological testing of polydentate oxohydroxypyridinecarboxylate ligansd, Journal of Medicinal Chemistry, 31 (1988) 11-18.

[63] L. Allott, C. Da Pieve, J. Meyers, T. Spinks, D.M. Ciobota, G. Kramer-Marek, G. Smith, Evaluation of DFO-HOPO as an octadentate chelator for zirconium-89, Chemical Communications, 53 (2017) 8529-8532.

[64] A.H. Alnahwi, S. Ait-Mohand, V. Dumulon-Perreault, Y.L. Dory, B. Guérin, Promising Performance of 4HMS, a New Zirconium-89 Octadendate Chelator, ACS Omega, 5 (2020) 10731-10739.

[65] F. Guerard, Y.S. Lee, R. Tripier, L.P. Szajek, J.R. Deschamps, M.W. Brechbiel, Investigation of Zr(IV) and Zr-89(IV) complexation with hydroxamates: progress towards designing a better chelator than desferrioxamine B for immuno-PET imaging, Chemical Communications, 49 (2013) 1002-1004.

[66] F. Guerard, Y.S. Lee, M.W. Brechbiel, Rational Design, Synthesis, and Evaluation of Tetrahydroxamic Acid Chelators for Stable Complexation of Zirconium(IV), Chemistry-a European Journal, 20 (2014) 5584-5591.

[67] U. Seibold, B. Wängler, C. Wängler, Rational Design, Development, and Stability Assessment of a Macrocyclic Four-Hydroxamate-Bearing Bifunctional Chelating Agent for 89Zr, ChemMedChem, 12 (2017) 1555-1571.

[68] C. Zhai, D. Summer, C. Rangger, G.M. Franssen, P. Laverman, H. Haas, M. Petrik, R. Haubner, C. Decristoforo, Novel bifunctional cyclic chelator for 89Zr labeling-radiolabeling and targeting properties of RGD conjugates, Mol. Pharm., 12 (2015) 2142-2150.

[69] C. Zhai, S. He, Y. Ye, C. Rangger, P. Kaeopookum, D. Summer, H. Haas, L. Kremser, H. Lindner, J. Foster, J. Sosabowski, C. Decristoforo, Rational design, synthesis and preliminary evaluation of novel fusarinine C-based chelators for radiolabeling with Zirconium-89, Biomolecules, 9 (2019).

[70] B. Klasen, D. Lemcke, T.L. Mindt, G. Gasser, F. Rosch, Development and in vitro evaluation of new bifunctional Zr-89-chelators based on the 6-amino-1,4-diazepane scaffold for immuno-PET applications, Nucl. Med. Biol., 102 (2021) 12-23.

[71] L. Russelli, F. De Rose, L. Leone, S. Reder, M. Schwaiger, C. D'Alessandria, L. Tei, A Semi Rigid Novel Hydroxamate AMPED-Based Ligand for Zr-89 PET Imaging, Molecules, 26 (2021).

[72] A.E.V. Gorden, J. Xu, K.N. Raymond, P. Durbin, Rational design of sequestering agents for plutonium and other actinides, Chem. Rev., 103 (2003) 4207-4282.

[73] N. Bhupathiraju, A. Younes, M.H. Cao, J. Ali, H.T. Cicek, K.M. Tully, S. Ponnala, J.W. Babich, M.A. Deri, J.S. Lewis, L.C. Francesconi, C.M. Drain, Improved synthesis of the bifunctional chelator p-SCN-Bn-HOPO, Organic & Biomolecular Chemistry, 17 (2019) 6866-6871.

[74] M.A. Deri, S. Ponnala, P. Kozlowski, B.P. Burton-Pye, H.T. Cicek, C. Hu, J.S. Lewis, L.C. Francesconi, P-SCN-Bn-HOPO: A Superior Bifunctional Chelator for 89Zr ImmunoPET, Bioconjugate Chem., 26 (2015) 2579-2591.

[75] M.A. Deri, S. Ponnala, B.M. Zeglis, G. Pohl, J.J. Dannenberg, J.S. Lewis, L.C. Francesconi, Alternative chelator for 89Zr radiopharmaceuticals: Radiolabeling and evaluation of 3,4,3-(LI-1,2-HOPO), Journal of Medicinal Chemistry, 57 (2014) 4849-4860.

[76] M.T. Ma, L.K. Meszaros, B.M. Paterson, D.J. Berry, M.S. Cooper, Y. Ma, R.C. Hider, P.J. Blower, Tripodal tris(hydroxypyridinone) ligands for immunoconjugate PET imaging with 89Zr4+: Comparison with desferrioxamine-B, Dalton Transactions, 44 (2015) 4884-4900.

[77] C. Buchwalder, C. Rodríguez-Rodríguez, P. Schaffer, S.K. Karagiozov, K. Saatchi, U.O. Häfeli, A new tetrapodal 3-hydroxy-4-pyridinone ligand for complexation of 89zirconium for positron emission tomography (PET) imaging, Dalton Transactions, 46 (2017) 9654-9663.

[78] C. Buchwalder, M.D.G. Jaraquemada-Peláez, J. Rousseau, H. Merkens, C. Rodríguez-Rodríguez, C. Orvig, F. Bénard, P. Schaffer, K. Saatchi, U.O. Häfeli, Evaluation of the Tetrakis(3-Hydroxy-4-Pyridinone) Ligand THPN with Zirconium(IV): Thermodynamic Solution Studies, Bifunctionalization, and in Vivo Assessment of Macromolecular 89Zr-THPN-Conjugates, Inorg. Chem., 58 (2019) 14667-14681.

[79] M. Sturzbecher-Hoehne, T.A. Choi, R.J. Abergel, Hydroxypyridinonate complex stability of group (IV) metals and tetravalent f-block elements: The key to the next generation of chelating agents for radiopharmaceuticals, Inorg. Chem., 54 (2015) 3462-3468.

[80] M. Savastano, C. Bazzicalupi, G. Ferraro, E. Fratini, P. Gratteri, A. Bianchi, Tales of the unexpected: The case of zirconium(IV) complexes with desferrioxamine, Molecules, 24 (2019).

[81] Y. Toporivska, E. Gumienna-Kontecka, The solution thermodynamic stability of desferrioxamine B (DFO) with Zr(IV), Journal of Inorganic Biochemistry, 198 (2019).

[82] J.N. Tinianow, D.N. Pandya, S.L. Pailloux, A. Ogasawara, A.N. Vanderbilt, H.S. Gill, S.P. Williams, T.J. Wadas, D. Magda, J. Marik, Evaluation of a 3-hydroxypyridin-2-one (2,3-HOPO) based macrocyclic chelator for 89Zr4+ and its use for immunoPET imaging of HER2 positive model of ovarian carcinoma in mice, Theranostics, 6 (2016) 511-521.

[83] D.N. Pandya, S. Pailloux, D. Tatum, D. Magda, T.J. Wadas, Di-macrocyclic terephthalamide ligands as chelators for the PET radionuclide zirconium-89, Chemical Communications, 51 (2015) 2301-2303.

[84] J. Roy, E.M. Jagoda, F. Basuli, O. Vasalatiy, T.E. Phelps, K. Wong, A.T. Ton, U.B. Hagemann, A.S. Cuthbertson, P.E. Cole, R. Hassan, P.L. Choyke, F.I. Lin, In Vitro and In Vivo Comparison of 3,2-HOPO Versus Deferoxamine-Based Chelation of Zirconium-89 to the Antimesothelin Antibody Anetumab, Cancer Biother. Radiopharm., 36 (2021) 316-325.

[85] N.B. Bhatt, D.N. Pandya, J. Xu, D. Tatum, D. Magda, T.J. Wadas, Evaluation of macrocyclic hydroxyisophthalamide ligands as chelators for zirconium-89, PLoS One, 12 (2017).

[86] M.A. Deri, B.M. Zeglis, L.C. Francesconi, J.S. Lewis, PET imaging with 89Zr: From radiochemistry to the clinic, Nucl. Med. Biol., 40 (2013) 3-14.

[87] C. Ekberg, G. Källvenius, Y. Albinsson, P.L. Brown, Studies on the hydrolytic behavior of zirconium(IV), Journal of Solution Chemistry, 33 (2004) 47-79.

[88] A. Singhal, L.M. Toth, J.S. Lin, K. Affholter, Zirconium(IV) tetramer/octamer hydrolysis equilibrium in aqueous hydrochloric acid solution, Journal of the American Chemical Society, 118 (1996) 11529-11534.

[89] A. Veyland, L. Dupont, J.C. Pierrard, J. Rimbault, M. Aplincourt, Thermodynamic stability of zirconium(IV) complexes with hydroxy ions, European Journal of Inorganic Chemistry, (1998) 1765-1770.

[90] E.W. Price, C. Orvig, Matching chelators to radiometals for radiopharmaceuticals, Chem. Soc. Rev., 43 (2014) 260-290.

[91] L.R. Perk, O.J. Visser, M.S.V. Walsum, M. Vosjan, G.W.M. Visser, J.M. Zijlstra, P.C. Huijgens, G. van Dongen, Preparation and evaluation of Zr-89-Zevalin for monitoring of Y-90-Zevalin biodistribution with positron emission tomography, Eur. J. Nucl. Med. Mol. Imaging, 33 (2006) 1337-1345.

[92] J.P. Holland, V. Divilov, N.H. Bander, P.M. Smith-Jones, S.M. Larson, J.S. Lewis, Zr-89-DFO-J591 for ImmunoPET of Prostate-Specific Membrane Antigen Expression In Vivo, J. Nucl. Med., 51 (2010) 1293-1300.

[93] W.E. Meijs, J.D.M. Herscheid, H.J. Haisma, R. Wijbrandts, F. van Langevelde, P.J. Van Leuffen, R. Mooy, H.M. Pinedo, Production of highly pure no-carrier added 89Zr for the labelling of antibodies with a positron emitter, Appl. Radiat. Isot., 45 (1994) 1143-1147.

[94] J.P. Holland, Y. Sheh, J.S. Lewis, Standardized methods for the production of high specific-activity zirconium-89, Nucl. Med. Biol., 36 (2009) 729-739.

[95] A. Veyland, L. Dupont, J. Rimbault, J.C. Pierrard, M. Aplincourt, Aqueous chemistry of zirconium(IV) in carbonate media, Helvetica Chimica Acta, 83 (2000) 414-427.

[96] M.J.W.D. Vosjan, L.R. Perk, G.W.M. Visser, M. Budde, P. Jurek, G.E. Kiefer, G.A.M.S. Van Dongen, Conjugation and radiolabeling of monoclonal antibodies with zirconium-89 for PET imaging using the bifunctional chelate p-isothiocyanatobenzyl-desferrioxamine, Nature Protocols, 5 (2010) 739-743.

[97] S. Molavipordanjani, V. Tolmachev, S.J. Hosseinimehr, Basic and practical concepts of radiopharmaceutical purification methods, Drug Discovery Today, 24 (2019) 315-324.

[98] M. Chomet, G. van Dongen, D.J. Vugts, State of the Art in Radiolabeling of Antibodies with Common and Uncommon Radiometals for Preclinical and Clinical Immuno-PET, Bioconjugate Chem., 32 (2021) 1315-1330.

[99] J.K. Yoon, B.N. Park, E.K. Ryu, Y.S. An, S.J. Lee, Current Perspectives on(89)Zr-PET Imaging, Int. J. Mol. Sci., 21 (2020) 18.

[100] B.N. McKnight, N.T. Viola-Villegas, Zr-89-ImmunoPET companion diagnostics and their impact in clinical drug development, J. Label. Compd. Radiopharm., 61 (2018) 727-738.

[101] W.J. Wei, Z.T. Rosenkrans, J.J. Liu, G. Huang, Q.Y. Luo, W.B. Cai, ImmunoPET: Concept, Design, and Applications, Chem. Rev., 120 (2020) 3787-3851.

[102] G. van Dongen, W. Beaino, A.D. Windhorst, G.J.C. Zwezerijnen, D.E. Oprea-Lager, N.H. Hendrikse, C. van Kuijk, R. Boellaard, M.C. Huisman, D.J. Vugts, The Role of(89)Zr-Immuno-PET in Navigating and Derisking the Development of Biopharmaceuticals, J. Nucl. Med., 62 (2021) 438-445.

[103] P.K.E. Borjesson, Y.W.S. Jauw, R. Boellaard, R. de Bree, E.F.I. Comans, J.C. Roos, J.A. Castelijns, M. Vosjan, J.A. Kummer, C.R. Leemans, A.A. Lammertsma, G. van Dongen, Performance of immuno-positron emission tomography with zirconium-89-labeled chimeric monoclonal antibody U36 in the detection of lymph node metastases in head and neck cancer patients, Clin. Cancer Res., 12 (2006) 2133-2140.

[104] P.K.E. Borjesson, Y.W.S. Jauw, R. de Bree, J.C. Roos, J.A. Castelijns, C.R. Leemans, G. van Dongen, R. Boellaard, Radiation Dosimetry of Zr-89-Labeled Chimeric Monoclonal Antibody U36 as Used for Immuno-PET in Head and Neck Cancer Patients, J. Nucl. Med., 50 (2009) 1828-1836.

[105] I. Verel, G.W.M. Visser, R. Boellaard, M. Stigter-van Walsum, G.B. Snow, G. van Dongen, Zr-89 immuno-PET: Comprehensive procedures for the production of Zr-89-labeled monoclonal antibodies, J. Nucl. Med., 44 (2003) 1271-1281.

[106] L.R. Perk, M. Vosjan, G.W.M. Visser, M. Budde, P. Jurek, G.E. Kiefer, G. van Dongen, p-Isothiocyanatobenzyl-desferrioxamine: a new bifunctional chelate for facile radiolabeling of monoclonal antibodies with zirconium-89 for immuno-PET imaging, Eur. J. Nucl. Med. Mol. Imaging, 37 (2010) 250-259.

[107] D.N. Pandya, N.B. Bhatt, F. Almaguel, S. Rideout-Danner, H.D. Gage, K.K.S. Sai, T.J. Wadas, Zr-89-Chloride Can Be Used for Immuno-PET Radiochemistry Without Loss of Antigen Reactivity In Vivo, J. Nucl. Med., 60 (2019) 696-701.

[108] A.J. Poot, K.W.A. Adamzek, A.D. Windhorst, M. Vosjan, S. Kropf, H.J. Wester, G. van Dongen, D.J. Vugts, Fully Automated Zr-89 Labeling and Purification of Antibodies, J. Nucl. Med., 60 (2019) 691-695.

[109] P.M.R. Pereira, A. Ragupathi, S. Shmuel, K. Mandleywala, N.T. Viola, J.S. Lewis, HER2-Targeted PET Imaging and Therapy of Hyaluronan-Masked HER2-Overexpressing Breast Cancer, Mol. Pharm., 17 (2020) 327-337.

[110] E.C. Dijkers, T.H.O. Munnink, J.G. Kosterink, A.H. Brouwers, P.L. Jager, J.R. de Jong, G.A. van Dongen, C.P. Schroder, M.N. Lub-de Hooge, E.G. de Vries, Biodistribution of Zr-89-trastuzumab and PET Imaging of HER2-Positive Lesions in Patients With Metastatic Breast Cancer, Clin. Pharmacol. Ther., 87 (2010) 586-592.

[111] L.S. Lindstrom, E. Karlsson, U.M. Wilking, U. Johansson, J. Hartman, E.K. Lidbrink, T. Hatschek, L. Skoog, J. Bergh, Clinically Used Breast Cancer Markers Such As Estrogen Receptor, Progesterone Receptor, and Human Epidermal Growth Factor Receptor 2 Are Unstable Throughout Tumor Progression, J. Clin. Oncol., 30 (2012) 2601-2608.

[112] G.A. Ulaner, D.M. Hyman, S.K. Lyashchenko, J.S. Lewis, J.A. Carrasquillo, 89Zr-Trastuzumab PET/CT for Detection of Human Epidermal Growth Factor Receptor 2-Positive Metastases in Patients With Human Epidermal Growth Factor Receptor 2-Negative Primary Breast Cancer, Clin. Nucl. Med., 42 (2017) 912-917.

[113] F. Dehdashti, N.Y. Wu, R. Bose, M.J. Naughton, C.X. Ma, B.V. Marquez-Nostra, P. Diebolder, C. Mpoy, B.E. Rogers, S.E. Lapi, R. Laforest, B.A. Siegel, Evaluation of Zr-89 trastuzumab-PET/CT in differentiating HER2-positive from HER2-negative breast cancer, Breast Cancer Res. Treat., 169 (2018) 523-530.

[114] F. Bensch, A.H. Brouwers, M.N. Lub-de Hooge, J.R. de Jong, B. van der Vegt, S. Sleijfer, E.G.E. de Vries, C.P. Schroder, Zr-89-trastuzumab PET supports clinical decision making in breast cancer patients, when HER2 status cannot be determined by standard work up, Eur. J. Nucl. Med. Mol. Imaging, 45 (2018) 2300-2306.

[115] C. Lohrmann, E. O'Reilly, J. Odonoghue, K.H. Yu, N. Pandit-Taskar, S. Lyashchenko, S. Ruan, J. Wu, P. DeNoble, J. Carrasquillo, C. Schmidtlein, R. Teng, M.A. Lowery, A. Varghese, H. Estrella, W. Scholz, P. Maffuid, J. Lewis, W. Weber, First-

in-Human Study of Zr-89-DFO-HuMab-5B1 (MVT-2163) PET/CT imaging with and without HuMab-5B1 (MVT-5873) in patients with pancreatic cancer and other CA 19-9 positive malignancies, J. Nucl. Med., 58 (2017).

[116] J. O'Donoghue, C. Lohrmann, E. O'Reilly, K. Yu, M. Lowery, S. Lyashchenko, N. Pandit-Taskar, S. Ruan, L. Wu, R. Teng, C. Schmidtlein, J. Carrasquillo, W. Scholz, P. Maffuid, J. Lewis, W. Weber, Biodistribution and radiation rose estimates for Zr-89-DFO-HuMab-5B1 (MVT-2163) in CA19-9 positive cancer: first-in-man results, J. Nucl. Med., 58 (2017).

[117] R.I.J. Merkx, D. Lobeek, M. Konijnenberg, L.D. Jimenez-Franco, A. Kluge, E. Oosterwijk, P.F.A. Mulders, M. Rijpkema, Phase I study to assess safety, biodistribution and radiation dosimetry for Zr-89-girentuximab in patients with renal cell carcinoma, Eur. J. Nucl. Med. Mol. Imaging, 48 (2021) 3277-3285.

[118] S.R. Verhoeff, S.C. van Es, E. Boon, E. van Helden, L. Angus, S.G. Elias, S.F. Oosting, E.H. Aarntzen, A.H. Brouwers, T.C. Kwee, S. Heskamp, O.S. Hoekstra, H. Verheul, A.A.M. van der Veldt, E.G.E. de Vries, O.C. Boerman, W.T.A. van der Graaf, W.J.G. Oyen, C.M.L. van Herpen, Lesion detection by Zr-89 Zr-DFO-girentuximab and F-18 FDG-PET/CT in patients with newly diagnosed metastatic renal cell carcinoma, Eur. J. Nucl. Med. Mol. Imaging, 46 (2019) 1931-1939.

[119] M.C.H. Hekman, M. Rijpkema, E.H. Aarntzen, S.F. Mulder, J.F. Langenhuijsen, E. Oosterwijk, O.C. Boerman, W.J.G. Oyen, P.F.A. Mulders, Positron Emission Tomography/Computed Tomography with Zr-89-girentuximab Can Aid in Diagnostic Dilemmas of Clear Cell Renal Cell Carcinoma Suspicion, European Urology, 74 (2018) 257-260.

[120] K. Muylle, P. Flamen, D. Vugts, T. Guiot, G. Ghanem, N. Meuleman, P. Bourgeois, B. Vanderlinden, G. van Dongen, H. Everaert, M. Vaes, D. Bron, Tumour targeting and radiation dose of radioimmunotherapy with Y-90-rituximab in CD20+B-cell lymphoma as predicted by Zr-89-rituximab immuno-PET: impact of preloading with unlabelled rituximab, Eur. J. Nucl. Med. Mol. Imaging, 42 (2015) 1304-1314.

[121] S. Bruijnen, M. Tsang-A-Sjoe, H. Raterman, T. Ramwadhdoebe, D. Vugts, G. van Dongen, M. Huisman, O. Hoekstra, P.P. Tak, A. Voskuyl, C. van der Laken, B-cell imaging with zirconium-89 labelled rituximab PET-CT at baseline is associated with therapeutic response 24 weeks after initiation of rituximab treatment in rheumatoid arthritis patients, Arthritis Res. Ther., 18 (2016) 8.

[122] Y.W.S. Jauw, J.M. Zijlstra, D. de Jong, D.J. Vugts, S. Zweegman, O.S. Hoekstra, G. van Dongen, M.C. Huisman, Performance of Zr-89-Labeled-Rituximab-PET as an Imaging Biomarker to Assess CD20 Targeting: A Pilot Study in Patients with Relapsed/Refractory Diffuse Large B Cell Lymphoma, PLoS One, 12 (2017) 12.

[123] K.G. Laban, R. Kalmann, R.J. Leguit, B. de Keizer, Zirconium-89-labelled rituximab PET-CT in orbital inflammatory disease, EJNMMI Res., 9 (2019).

[124] H. Adams, E.M.W. van de Garde, C.H.M. van Moorsel, D.J. Vugts, G. van Dongen, J.C. Grutters, R.G. Keijsers, Zr-89 Zr-rituximab PET/CT activity in patients with therapy refractory interstitial pneumonitis: a feasibility study, Am. J. Nucl. Med. Molec. Imaging, 9 (2019) 296-308.

[125] H. Adams, B. Meek, E.M.W. van de Garde, C.H.M. van Moorsel, D.J. Vugts, R.G. Keijsers, J.C. Grutters, Altered splenic Zr-89 Zr-rituximab uptake in patients with interstitial lung disease not responding to rituximab: could this indicate a splenic immune-mediated mechanism?, Am. J. Nucl. Med. Molec. Imaging, 10 (2020) 168-+.

[126] S.N.F. Rizvi, O.J. Visser, M. Vosjan, A. van Lingen, O.S. Hoekstra, J.M. Zijlstra, P.C. Huijgens, G. van Dongen, M. Lubberink, Biodistribution, radiation dosimetry and scouting of Y-90-ibritumomab tiuxetan therapy in patients with relapsed B-cell non-Hodgkin's lymphoma using Zr-89-ibritumomab tiuxetan and PET, Eur. J. Nucl. Med. Mol. Imaging, 39 (2012) 512-520.

[127] Y.W.S. Jauw, M.C. Huisman, T.K. Nayak, D.J. Vugts, R. Christen, V.M. Naegelen, D. Ruettinger, F. Heil, A.A. Lammertsma, H.M.W. Verheul, O.S. Hoekstra, G. van Dongen, C. van Oordt, Assessment of target-mediated uptake with immuno-PET: analysis of a phase I clinical trial with an anti-CD44 antibody, EJNMMI Res., 8 (2018) 9.

[128] C. van Oordt, C. Gomez-Roca, C. van Herpen, A.L. Coveler, D. Mahalingam, H.M.W. Verheul, W.T.A. van der Graaf, R. Christen, D. Ruttinger, S. Weigand, M.A. Cannarile, F. Heil, M. Brewster, A.C. Walz, T.K. Nayak, E. Guarin, V. Meresse, C. Le Tourneau, First-in-human phase I clinical trial of RG7356, an anti-CD44 humanized antibody, in patients with advanced, CD44-expressing solid tumors, Oncotarget, 7 (2016) 80046-80058.

[129] N. Pandit-Taskar, M.A. Postow, M.D. Hellmann, J.J. Harding, C.A. Barker, J.A. O'Donoghue, M. Ziolkowska, S.T. Ruan, S.K. Lyashchenko, F. Tsai, M. Farwell, T.C. Mitchell, R. Korn, W. Le, J.S. Lewis, W.A. Weber, D. Behera, I. Wilson, M. Gordon, A.M. Wu, J.D. Wolchok, First-in-Humans Imaging with Zr-89-Df-IAB22M2C Anti-CD8 Minibody in Patients with Solid Malignancies: Preliminary Pharmacokinetics, Biodistribution, and Lesion Targeting, J. Nucl. Med., 61 (2020) 512-519.

[130] K.L. Moek, S.J.H. Waaijer, I.C. Kok, F.V. Suurs, A.H. Brouwers, C. van Oordt, T.T. Wind, J.A. Gietema, C.P. Schroder, S.V.K. Mahesh, A. Jorritsma-Smit, M.N. Lub-de Hooge, R.S.N. Fehrmann, D.J.A. de Groot, E.G.E. de Vries, Zr-89-labeled Bispecific T-cell Engager AMG 211 PET Shows AMG 211 Accumulation in CD3-rich Tissues and Clear, Heterogeneous Tumor Uptake, Clin. Cancer Res., 25 (2019) 3517-3527.

[131] A.J.G. Even, O. Hamming-Vrieze, W. van Elmpt, V.J.L. Winnepenninckx, J. Heukelom, M.E.T. Tesselaar, W.V. Vogel, A. Hoeben, C.M.L. Zegers, D.J. Vugts, G. van Dongen, H. Bartelink, F.M. Mottaghy, F. Hoebers, P. Lambin, Quantitative assessment of Zirconium-89 labeled cetuximab using PET/CT imaging in patients with advanced head and neck cancer: a theragnostic approach, Oncotarget, 8 (2017) 3870-3880.

[132] J. van Loon, A.J.G. Even, H. Aerts, M. Ollers, F. Hoebers, W. van Elmpt, L. Dubois, A.M.C. Dingemans, R.I. Lalisang, P. Kempers, B. Brans, V. Winnepenninckx, E.J. Speel, E. Thunnissen, K.M. Smits, R. Boellaard, D.J. Vugts, D. De Ruysscher, P. Lambin, PET imaging of zirconium-89 labelled cetuximab: A phase I trial in patients with head and neck and lung cancer, Radiother. Oncol., 122 (2017) 267-273.

[133] N.E. Makris, R. Boellaard, A. van Lingen, A.A. Lammertsma, G. van Dongen, H.M. Verheul, C.W. Menke, M.C. Huisman, PET/CT-Derived Whole-Body and Bone Marrow Dosimetry of Zr-89-Cetuximab, J. Nucl. Med., 56 (2015) 249-254.

[134] E.J. van Helden, S.G. Elias, S.L. Gerritse, S.C. van Es, E. Boon, M.C. Huisman, N.C.T. van Grieken, H. Dekker, G. van Dongen, D.J. Vugts, R. Boellaard, C.M.L. van Herpen, E.G.E. de Vries, W.J.G. Oyen, A.H. Brouwers, H.M.W. Verheul, O.S. Hoekstra, C.W.M. van Oordt, Zr-89 Zr-cetuximab PET/CT as biomarker for cetuximab monotherapy in patients with RAS wild-type advanced colorectal cancer, Eur. J. Nucl. Med. Mol. Imaging, 47 (2020) 849-859.

[135] C.W.M. van Oordt, E.C. Gootjes, M.C. Huisman, D.J. Vugts, C. Roth, A.M. Luik, E.R. Mulder, R.C. Schuit, R. Boellaard, O.S. Hoekstra, G. van Dongen, H.M.W. Verheul, Zr-89-cetuximab PET imaging in patients with advanced colorectal cancer, Oncotarget, 6 (2015) 30384-30393.

[136] L. Lindenberg, S. Adler, I.B. Turkbey, F. Mertan, A. Ton, K. Do, S. Kummar, E.M. Gonzalez, S. Bhattacharyya, P.M. Jacobs, P. Choyke, Dosimetry and first human experience with Zr-89-panitumumab, Am. J. Nucl. Med. Molec. Imaging, 7 (2017) 195-203.

[137] G.A. Ulaner, S.K. Lyashchenko, C. Riedl, S. Ruan, P.B. Zanzonico, D. Lake, K. Jhaveri, B. Zeglis, J.S. Lewis, J.A. O'Donoghue, First-in-Human Human Epidermal Growth Factor Receptor 2-Targeted Imaging Using Zr-89-Pertuzumab PET/CT: Dosimetry and Clinical Application in Patients with Breast Cancer, J. Nucl. Med., 59 (2018) 900-906.

[138] G.A. Ulaner, J.A. Carrasquillo, C.C. Riedl, R. Yeh, V. Hatzoglou, D.S. Ross, K. Jhaveri, S. Chandarlapaty, D.M. Hyman, B.M. Zeglis, S.K. Lyashchenko, J.S. Lewis, Identification of HER2-Positive Metastases in Patients with HER2-Negative Primary Breast Cancer by Using HER2-targeted Zr-89-Pertuzumab PET/CT, Radiology, 296 (2020) 370-378.

[139] G. Gebhart, L.E. Lamberts, Z. Wimana, C. Garcia, P. Emonts, L. Ameye, S. Stroobants, M. Huizing, P. Aftimos, J. Tol, W.J.G. Oyen, D.J. Vugts, O.S. Hoekstra, C.P. Schroder, C. van Oordt, T. Guiot, A.H. Brouwers, A. Awada, E.G.E. de Vries, P. Flamen, Molecular imaging as a tool to investigate heterogeneity of advanced HER2-positive breast cancer and to predict patient outcome under trastuzumab emtansine (T-DM1): the ZEPHIR trial, Annals of Oncology, 27 (2016) 619-624.

[140] R. Laforest, S.E. Lapi, R. Oyama, R. Bose, A. Tabchy, B.V. Marquez-Nostra, J. Burkemper, B.D. Wright, J. Frye, S. Frye, B.A. Siegel, F. Dehdashti, Zr-89 Trastuzumab: Evaluation of Radiation Dosimetry, Safety, and Optimal Imaging Parameters in Women with HER2-Positive Breast Cancer, Mol. Imaging. Biol., 18 (2016) 952-959.

[141] J.A. O'Donoghue, J.S. Lewis, N. Pandit-Taskar, S.E. Fleming, H. Schoder, S.M. Larson, V. Beylergil, S. Ruan, S.K. Lyashchenko, P.B. Zanzonico, W.A. Weber, J.A. Carrasquillo, Y.Y. Janjigian, Pharmacokinetics, Biodistribution, and Radiation Dosimetry for Zr-89-Trastuzumab in Patients with Esophagogastric Cancer, J. Nucl. Med., 59 (2018) 161-166.

[142] C. van Oordt, A. McGeoch, M. Bergstrom, I. McSherry, D.A. Smith, M. Cleveland, W. Al-Azzam, L.F. Chen, H. Verheul, O.S. Hoekstra, D.J. Vugts, I. Freedman, M. Huisman, C. Matheny, G. van Dongen, S. Zhang, Immuno-PET Imaging to Assess Target Engagement: Experience from Zr-89-Anti-HER3 mAb (GSK2849330) in Patients with Solid Tumors, J. Nucl. Med., 60 (2019) 902-909.

[143] F. Bensch, L.E. Lamberts, M.N. Lub-De Hooge, A. van Scheltinga, J.R. de Jong, J.A. Gietema, C.P. Schroder, M.M. Smeenk, W. Jacob, K. Abiraj, M. Wolf, C. Adessi, G. Meneses-Lorente, M. Zajac, M. Weisser, A.H. Brouwers, E. De Vries, Phase I imaging study of the HER3 antibody RG7116 using Zr-89-RG7116-PET in patients with metastatic or locally advanced HER3-positive solid tumors, J. Clin. Oncol., 32 (2014) 1.

[144] F. Bensch, L.E. Lamberts, M.M. Smeenk, A. Jorritsma-Smit, M.N. Lub-de Hooge, A. van Scheltinga, J.R. de Jong, J.A. Gietema, C.P. Schroder, M. Thomas, W. Jacob, K. Abiraj, C. Adessi, G. Meneses-Lorente, I. James, M. Weisser, A.H. Brouwers, E.G.E. de Vries, Zr-89-Lumretuzumab PET Imaging before and during HER3 Antibody Lumretuzumab Treatment in Patients with Solid Tumors, Clin. Cancer Res., 23 (2017) 6128-6137.

[145] L.E. Lamberts, C. van Oordt, E.J. ter Weele, F. Bensch, M.M. Smeenk, J. Voortman, O.S. Hoekstra, S.P. Williams, B.M. Fine, D. Maslyar, J.R. de Jong, J.A. Gietema, C.P. Schroder, A.H.H. Bongaerts, M.N. Lub-de Hooge, H.M.W. Verheul, S.M.S. Bohorquez, A. Glaudemans, E.G.E. de Vries, ImmunoPET with Anti-Mesothelin Antibody in Patients with Pancreatic and Ovarian Cancer before Anti-Mesothelin Antibody-Drug Conjugate Treatment, Clin. Cancer Res., 22 (2016) 1642-1652.

[146] A.N. Niemeijer, D. Leung, M.C. Huisman, I. Bahce, O.S. Hoekstra, G. van Dongen, R. Boellaard, S. Du, W. Hayes, R. Smith, A.D. Windhorst, N.H. Hendrikse, A. Poot, D.J. Vugts, E. Thunnissen, P. Morin, D. Lipovsek, D.J. Donnelly, S.J. Bonacorsi, L.M. Velasquez, T.D. de Gruijl, E.F. Smit, A.J. de Langen, Whole body PD-1 and PD-L1 positron emission tomography in patients with non-small-cell lung cancer, Nat. Commun., 9 (2018) 5.

[147] F. Bensch, E.L. van der Veen, M.N. Lub-de Hooge, A. Jorritsma-Smit, R. Boellaard, I.C. Kok, S.F. Oosting, C.P. Schroder, T.J.N. Hiltermann, A.J. van der Wekken, H.J.M. Groen, T.C. Kwee, S.G. Elias, J.A. Gietema, S.S. Bohorquez, A. de Crespigny, S.P. Williams, C. Mancao, A.H. Brouwers, B.M. Fine, E.G.E. de Vries, Zr-89-atezolizumab imaging as a non-invasive approach to assess clinical response to PD-L1 blockade in cancer, Nat. Med., 24 (2018) 1852-+.

[148] N. Pandit-Taskar, J.A. O'Donoghue, V. Beylergil, S. Lyashchenko, S.T. Ruan, S.B. Solomon, J.C. Durack, J.A. Carrasquillo, R.A. Lefkowitz, M. Gonen, J.S. Lewis, J.P. Holland, S.M. Cheal, V.E. Reuter, J.R. Osborne, M.F. Loda, P.M. Smith-Jones, W.A. Weber, N.H. Bander, H.I. Scher, M.J. Morris, S.M. Larson, Zr-89-huJ591 immuno-PET imaging in patients with advanced metastatic prostate cancer, Eur. J. Nucl. Med. Mol. Imaging, 41 (2014) 2093-2105.

[149] N. Pandit-Taskar, J.A. O'Donoghue, J.C. Durack, S.K. Lyashchenko, S.M. Cheal, V. Beylergil, R.A. Lefkowitz, J.A. Carrasquillo, D.F. Martinez, A.M. Fung, S.B. Solomon, M. Gonen, G. Heller, M. Loda, D.M. Nanus, S.T. Tagawa, J.L. Feldman, J.R. Osborne, J.S. Lewis, V.E. Reuter, W.A. Weber, N.H. Bander, H.I. Scher, S.M. Larson, M.J. Morris, A Phase I/II Study for Analytic Validation of Zr-89-J591 ImmunoPET as a Molecular Imaging Agent for Metastatic Prostate Cancer, Clin. Cancer Res., 21 (2015) 5277-5285.

[150] J.R. Osborne, D.A. Green, D.E. Spratt, S. Lyashchenko, S.B. Fareedy, B.D. Robinson, B.J. Beattie, M. Jain, J.S. Lewis, P. Christos, S.M. Larson, N.H. Bander, D.S. Scherr, A Prospective Pilot Study of Zr-89-J591/Prostate Specific Membrane Antigen Positron Emission Tomography in Men with Localized Prostate Cancer Undergoing Radical Prostatectomy, J. Urol., 191 (2014) 1439-1445.

[151] N. Pandit-Taskar, J.A. O'Donoghue, S.T. Ruan, S.K. Lyashchenko, J.A. Carrasquillo, G. Heller, D.F. Martinez, S.M. Cheal, J.S. Lewis, M. Fleisher, J.S. Keppler, R.E. Reiter, A.M. Wu, W.A. Weber, H.I. Scher, S.M. Larson, M.J. Morris, First-in-Human Imaging with Zr-89-Df-IAB2M Anti-PSMA Minibody in Patients with Metastatic Prostate Cancer: Pharmacokinetics, Biodistribution, Dosimetry, and Lesion Uptake, J. Nucl. Med., 57 (2016) 1858-1864.

[152] A. Joraku, K. Hatano, K. Kawai, S. Kandori, T. Kojima, N. Fukumitsu, T. Isobe, Y. Mori, M. Sakata, T. Hara, K. Nasu, M. Minami, Y. Iizumi, H. Nishiyama, Phase I/IIa PET imaging study with (89)zirconium labeled anti-PSMA minibody for urological malignancies, Ann. Nucl. Med., 33 (2019) 119-127.

[153] M. Matsuda, E. Ishikawa, T. Yamamoto, K. Hatano, A. Joraku, Y. Iizumi, Y. Masuda, H. Nishiyama, A. Matsumura, Potential use of prostate specific membrane antigen (PSMA) for detecting the tumor neovasculature of brain tumors by PET imaging with Zr-89-Df-IAB2M anti-PSMA minibody, J. Neuro-Oncol., 138 (2018) 581-589.

[154] J.A. Carrasquillo, B.M. Fine, N. Pandit-Taskar, S.M. Larson, S.E. Fleming, J.J. Fox, S.M. Cheal, J.A. O'Donoghue, S. Ruan, G. Ragupathi, S.K. Lyashchenko, J.L. Humm, H.I. Scher, M. Gonen, S.P. Williams, D.C. Danila, M.J. Morris, Imaging Patients with Metastatic Castration-Resistant Prostate Cancer Using Zr-89-DFO-MSTP2109A Anti-STEAP1 Antibody, J. Nucl. Med., 60 (2019) 1517-1523.

[155] J.A. O'Donoghue, D.C. Danila, N. Pandit-Taskar, V. Beylergil, S.M. Cheal, S.E. Fleming, J.J. Fox, S.T. Ruan, P.B. Zanzonico, G. Ragupathi, S.K. Lyashchenko, S.P. Williams, H.I. Scher, B.M. Fine, J.L. Humm, S.M. Larson, M.J. Morris, J.A. Carrasquillo, Pharmacokinetics and Biodistribution of a Zr-89 Zr-DFO-MSTP2109A Anti-STEAP1 Antibody in Metastatic Castration-Resistant Prostate Cancer Patients, Mol. Pharm., 16 (2019) 3083-3090.

[156] M.W. den Hollander, F. Bensch, A. Glaudemans, T.H.O. Munnink, R.H. Enting, W.F.A. den Dunnen, M. Heesters, F.A.E. Kruyt, M.N. Lub-de Hooge, J.C. de Groot, J. Pearlberg, J.A. Gietema, E.G.E. de Vries, A.M.E. Walenkamp, TGF-beta Antibody Uptake in Recurrent High-Grade Glioma Imaged with Zr-89-Fresolimumab PET, J. Nucl. Med., 56 (2015) 1310-1314.

[157] S.B.M. Gaykema, A.H. Brouwers, M.N. Lub-de Hooge, R.G. Pleijhuis, H. Timmer-Bosscha, L. Pot, G.M. van Dam, S.B. van der Meulen, J.R. de Jong, J. Bart, J. de Vries, L. Jansen, E.G.E. de Vries, C.P. Schroder, Zr-89- Bevacizumab PET Imaging in Primary Breast Cancer, J. Nucl. Med., 54 (2013) 1014-1018.

[158] S.B.M. Gaykema, C.P. Schroder, J. Vitfell-Rasmussen, S. Chua, T.H.O. Munnink, A.H. Brouwers, A.H.H. Bongaerts, M. Akimov, C. Fernandez-Ibarra, M.N. Lub-de Hooge, E.G.E. de Vries, C. Swanton, U. Banerji, Zr-89-trastuzumab and Zr-89-bevacizumab PET to Evaluate the Effect of the HSP90 Inhibitor NVP-AUY922 in Metastatic Breast Cancer Patients, Clin. Cancer Res., 20 (2014) 3945-3954.

[159] S.J. van Asselt, S.F. Oosting, A.H. Brouwers, A.H.H. Bongaerts, J.R. de Jong, M.N. Lub-de Hooge, T.H.O. Munnink, H.B. Fiebrich, W.J. Sluiter, T.P. Links, A.M.E. Walenkamp, E.G.E. de Vries, Everolimus Reduces Zr-89-Bevacizumab Tumor Uptake in Patients with Neuroendocrine Tumors, J. Nucl. Med., 55 (2014) 1087-1092.

[160] M.H. Jansen, S. van Zanten, D.G. van Vuurden, M.C. Huisman, D.J. Vugts, O.S. Hoekstra, G.A. van Dongen, G.J.L. Kaspers, Molecular Drug Imaging: Zr-89-Bevacizumab PET in Children with Diffuse Intrinsic Pontine Glioma, J. Nucl. Med., 58 (2017) 711-716.

[161] S. van Zanten, A.C.P. Sewing, A. van Lingen, O.S. Hoekstra, P. Wesseling, M.H. Meel, D.G. van Vuurden, G.J.L. Kaspers, E. Hulleman, M. Bugiani, Multiregional Tumor Drug-Uptake Imaging by PET and Microvascular Morphology in End-Stage Diffuse Intrinsic Pontine Glioma, J. Nucl. Med., 59 (2018) 612-615.

[162] S.F. Oosting, S.J. van Asselt, A.H. Brouwers, A.H.H. Bongaerts, J.D.J. Steinberg, J.R. de Jong, M.N. Lub-de Hooge, A.N.A. van der Horst-Schrivers, A.M.E. Walenkamp, E.W. Hoving, W.J. Sluiter, B.A. Zonnenberg, E.G.E. de Vries, T.P. Links, Zr-89-Bevacizumab PET Visualizes Disease Manifestations in Patients with von Hippel-Lindau Disease, J. Nucl. Med., 57 (2016) 1244-1250.

[163] I. Bahce, M.C. Huisman, E.E. Verwer, R. Ooijevaar, F. Boutkourt, D.J. Vugts, G. van Dongen, R. Boellaard, E.F. Smit, Pilot study of Zr-89-bevacizumab positron emission tomography in patients with advanced non-small cell lung cancer, EJNMMI Res., 4 (2014) 7.

[164] S.F. Oosting, A.H. Brouwers, S.C. van Es, W.B. Nagengast, T.H.O. Munnink, M.N. Lub-de Hooge, H. Hollema, J.R. de Jong, I.J. de Jong, S. de Haas, S.J. Scherer, W.J. Sluiter, R.A. Dierckx, A.H.H. Bongaerts, J.A. Gietema, E.G.E. de Vries, Zr-89-Bevacizumab PET Visualizes Heterogeneous Tracer Accumulation in Tumor Lesions of Renal Cell Carcinoma Patients and Differential Effects of Antiangiogenic Treatment, J. Nucl. Med., 56 (2015) 63-69.

[165] S.C. van Es, A.H. Brouwers, S.V.K. Mahesh, A.M. Leliveld-Kors, I.J. de Jong, M.N. Lub-de Hooge, E.G.E. de Vries, J.A. Gietema, S.F. Oosting, Zr-89-Bevacizumab PET: Potential Early Indicator of Everolimus Efficacy in Patients with Metastatic Renal Cell Carcinoma, J. Nucl. Med., 58 (2017) 905-910.

[166] M.C. Huisman, C. Van Oordt, J.M. Zijlstra, O.S. Hoekstra, R. Boellaard, G. van Dongen, D.K. Shah, Y.W.S. Jauw, Potential and pitfalls of Zr-89-immuno-PET to assess target status: Zr-89-trastuzumab as an example, EJNMMI Res., 11 (2021) 7.

[167] A. Richter, K. Knorr, M. Schlapschy, S. Robu, V. Morath, C. Mendler, H.Y. Yen, K. Steiger, M. Kiechle, W. Weber, A. Skerra, M. Schwaiger, First In-Human Medical Imaging with a PASylated Zr-89-Labeled Anti-HER2 Fab-Fragment in a Patient with Metastatic Breast Cancer, Nucl. Med. Molec. Imag., 54 (2020) 114-119.

[168] W.J. Wei, D.L. Ni, E.B. Ehlerding, Q.Y. Luo, W.B. Cai, PET Imaging of Receptor Tyrosine Kinases in Cancer, Molecular Cancer Therapeutics, 17 (2018) 1625-1636.

[169] K.E. Henry, G.A. Ulaner, J.S. Lewis, Clinical Potential of Human Epidermal Growth Factor Receptor 2 and Human Epidermal Growth Factor Receptor 3 Imaging in Breast Cancer, Pet Clinics, 13 (2018) 423-+.

[170] P. Diebolder, C. Mpoy, J. Scott, T.T. Huynh, R. Fields, D. Spitzer, N. Bandara, B.E. Rogers, Preclinical Evaluation of an Engineered Single-Chain Fragment Variable-Fragment Crystallizable Targeting Human CD44, J. Nucl. Med., 62 (2021) 137-143.

[171] A. Wesolowska, A. Kwiatkowska, L. Slomnicki, M. Dembinski, A. Master, M. Sliwa, K. Franciszkiewicz, S. Chouaib, B. Kaminska, Microglia-derived TGF-beta as an important regulator of glioblastoma invasion - an inhibition of TGF-beta-dependent effects by shRNA against human TGF-beta type II receptor, Oncogene, 27 (2008) 918-930.

[172] D. Carpanese, G. Ferro-Flores, B. Ocampo-Garcia, C. Santos-Cuevas, N. Salvarese, M. Figini, G. Fracasso, L. De Nardo, C. Bolzati, A. Rosato, L. Melendez-Alafort, Development of Lu-177-scFvD2B as a Potential Immunotheranostic Agent for Tumors Overexpressing the Prostate Specific Membrane Antigen, Sci Rep, 10 (2020).

[173] E.J. ter Weele, A. van Scheltinga, J.G.W. Kosterink, L. Pot, S.R. Vedelaar, L.E. Lamberts, S.P. Williams, M.N. Lub-de Hooge, E.G.E. de Vries, Imaging the distribution of an antibody-drug conjugate constituent targeting mesothelin with Zr-89 and IRDye 800CW in mice bearing human pancreatic tumor xenografts, Oncotarget, 6 (2015) 42081-42090.

[174] M. Conte, V. Frantellizzi, A. Matto, G. De Vincentis, New insight and future perspective of mesothelin-targeted agents in nuclear medicine, Clin. Transl. Imaging, 8 (2020) 265-278.

[175] M.L. Thibult, E. Mamessier, J. Gertner-Dardenne, S. Pastor, S. Just-Landi, L. Xerri, B. Chetaille, D. Olive, PD-1 is a novel regulator of human B-cell activation, International Immunology, 25 (2013) 129-+.

[176] J.Y. Ren, M.X. Xu, J.Y. Chen, J. Ding, P.P. Wang, L. Huo, F. Li, Z.B. Liu, PET imaging facilitates antibody screening for synergistic radioimmunotherapy with a Lu-177-labeled alpha PD-L1 antibody, Theranostics, 11 (2021) 304-315.

[177] K. Mandleywala, S. Shmuel, P.M.R. Pereira, J.S. Lewis, Antibody-Targeted Imaging of Gastric Cancer, Molecules, 25 (2020) 12.

[178] T. van Oostenbrugge, P. Mulders, Targeted PET/CT imaging for clear cell renal cell carcinoma with radiolabeled antibodies: recent developments using girentuximab, Curr. Opin. Urol., 31 (2021) 249-254.

[179] A. Altmann, U. Haberkorn, J. Siveke, The latest developments in imaging of fibroblast activation protein, Journal of Nuclear Medicine, 62 (2021) 160-167.

[180] P. Vallejo-Armenta, G. Ferro-Flores, C. Santos-Cuevas, F.O. García-Pérez, P. Casanova-Triviño, B. Sandoval-Bonilla, B. Ocampo-García, E. Azorín-Vega, M. Luna-Gutiérrez, [99mTc] Tc-iFAP/SPECT Tumor Stroma Imaging: Acquisition and Analysis of Clinical Images in Six Different Cancer Entities, Pharmaceuticals, 15 (2022) 729.

[181] D.N. Pandya, A. Sinha, H. Yuan, L. Mutkus, K. Stumpf, F.C. Marini, T.J. Wadas, Imaging of fibroblast activation protein alpha expression in a preclinical mouse model of glioma using positron emission tomography, Molecules, 25 (2020) 3672.

[182] H.M. Hintz, J.P. Gallant, D.J. Vander Griend, I.M. Coleman, P.S. Nelson, A.M. LeBeau, Imaging Fibroblast Activation Protein Alpha Improves Diagnosis of Metastatic Prostate Cancer with Positron Emission TomographyImaging FAP in Prostate Cancer, Clinical Cancer Research, 26 (2020) 4882-4891.

[183] K.S. Carmon, A. Azhdarinia, Application of Immuno-PET in Antibody-Drug Conjugate Development, Molecular Imaging, 17 (2018) 10.

[184] S.P. Williams, A. Ogasawara, J.N. Tinianow, J.E. Flores, D. Kan, J. Lau, M. Go, A.N. Vanderbilt, H.S. Gill, L. Miao, J. Goldsmith, B. Rubinfeld, W.G. Mao, R. Firestein, S.F. Yu, J. Marik, A. van Scheltinga, ImmunoPET helps predicting the efficacy of antibody-drug conjugates targeting TENB2 and STEAP1, Oncotarget, 7 (2016) 25103-25112.

[185] G.G. Kim, J.Y. Lee, P.S. Choi, S.W. Kim, J.H. Park, Tumor targeting effect of triphenylphosphonium cations and folic acid coated with Zr-89-labeled silica nanoparticles, Molecules, 25 (2020) 2922.

[186] F. Chen, K. Ma, L. Zhang, B. Madajewski, P. Zanzonico, S. Sequeira, M. Gonen, U. Wiesner, M.S. Bradbury, Target-or-clear zirconium-89 labeled silica nanoparticles for enhanced cancer-directed uptake in melanoma: a comparison of radiolabeling strategies, Chemistry of Materials, 29 (2017) 8269-8281.

[187] J.Y. Lee, C.K. Vyas, G.G. Kim, P.S. Choi, M.G. Hur, S.D. Yang, Y.B. Kong, E.J. Lee, J.H. Park, Red Blood Cell Membrane Bioengineered Zr-89 Labelled Hollow Mesoporous Silica Nanosphere for Overcoming Phagocytosis, Scientific Reports, 9 (2019) 7419.

[188] F. Chen, S. Goel, H.F. Valdovinos, H. Luo, R. Hernandez, T.E. Barnhart, W. Cai, In vivo integrity and biological fate of chelator-free zirconium-89-labeled mesoporous silica nanoparticles, ACS nano, 9 (2015) 7950-7959.

[189] D.L. Ni, D.W. Jiang, E.B. Ehlerding, P. Huang, W.B. Cai, Radiolabeling Silica-Based Nanoparticles via Coordination Chemistry: Basic Principles, Strategies, and Applications, Accounts of Chemical Research, 51 (2018) 778-788.

[190] F.R. Ai, C.A. Ferreira, F. Chen, W.B. Cai, Engineering of radiolabeled iron oxide nanoparticles for dual-modality imaging, Wiley Interdiscip. Rev.-Nanomed. Nanobiotechnol., 8 (2016) 619-630.

[191] S.X. Shi, B.C. Fliss, Z. Gu, Y.A. Zhu, H. Hong, H.F. Valdovinos, R. Hernandez, S. Goel, H.M. Luo, F. Chen, T.E. Barnhart, R.J. Nickles, Z.P. Xu, W.B. Cai, Chelator-Free Labeling of Layered Double Hydroxide Nanoparticles for in Vivo PET Imaging, Sci Rep, 5 (2015).

[192] C. Pérez-Medina, D. Abdel-Atti, Y. Zhang, V.A. Longo, C.P. Irwin, T. Binderup, J. Ruiz-Cabello, Z.A. Fayad, J.S. Lewis, W.J. Mulder, A modular labeling strategy for in vivo PET and near-infrared fluorescence imaging of nanoparticle tumor targeting, Journal of Nuclear Medicine, 55 (2014) 1706-1711.

[193] J.W. Seo, L.M. Mahakian, S. Tam, S. Qin, E.S. Ingham, C.F. Meares, K.W. Ferrara, The pharmacokinetics of Zr-89 labeled liposomes over extended periods in a murine tumor model, Nuclear medicine and biology, 42 (2015) 155-163.

[194] P. Zhang, Y. Yue, D. Pan, R. Yang, Y. Xu, L. Wang, J. Yan, X. Li, M. Yang, Pharmacokinetics study of Zr-89-labeled melanin nanoparticle in iron-overload mice, Nuclear Medicine and Biology, 43 (2016) 529-533.

[195] P.S. Choi, J.Y. Lee, S.D. Yang, J.H. Park, Biological behavior of nanoparticles with Zr-89 for cancer targeting based on their distinct surface composition, Journal of Materials Chemistry B, 9 (2021) 8237-8245.

[196] J.H. Lee, G.G. Kim, S.W. Kim, J.-H. Park, Zr-89 Labeled PAMAM Dendrimers 5G without a Chelator for a Cancer Diagnostic Agent, Journal of the Korean Physical Society, 77 (2020) 409-413.

[197] A.G. Kazakov, A.V. Severin, Sorption of 89Zr on hydroxyapatite nanoparticles as carriers for nuclear medicine, Journal of Radioanalytical and Nuclear Chemistry, 325 (2020) 199-205.

[198] P.R. McDonagh, G. Sundaresan, L. Yang, M. Sun, R. Mikkelsen, J. Zweit, Biodistribution and PET imaging of 89-zirconium labeled cerium oxide nanoparticles synthesized with several surface coatings, Nanomedicine: Nanotechnology, Biology and Medicine, 14 (2018) 1429-1440.

[199] N.B. Sobol, J.A. Korsen, A. Younes, K.J. Edwards, J.S. Lewis, ImmunoPET Imaging of Pancreatic Tumors with 89Zr-Labeled Gold Nanoparticle–Antibody Conjugates, Molecular imaging and biology, 23 (2021) 84-94.

[200] M. Fairclough, B. Ellis, H. Boutin, A. Jones, A. McMahon, S. Alzabin, A. Gennari, C. Prenant, Development of a method for the preparation of zirconium-89 radiolabelled chitosan nanoparticles as an application for leukocyte trafficking with positron emission tomography, Applied Radiation and Isotopes, 130 (2017) 7-12.

[201] M. Fairclough, C. Prenant, B. Ellis, H. Boutin, A. McMahon, G. Brown, P. Locatelli, A. Jones, A new technique for the radiolabelling of mixed leukocytes with zirconium-89 for inflammation imaging with positron emission tomography, Journal of Labelled Compounds and Radiopharmaceuticals, 59 (2016) 270-276.

[202] I. Hajdu, A. Makhlouf, V.R. Solomon, D. Michel, M. Al-Dulaymi, K.M. Wasan, H. Fonge, I. Badea, A 89Zr-labeled lipoplex nanosystem for image-guided gene delivery: design, evaluation of stability and in vivo behavior, International journal of nanomedicine, 13 (2018) 7801.

[203] P. Unak, V. Tekin, O.K. Guldu, O. Aras, 89Zr Labeled Fe3O4@ TiO2 nanoparticles: In vitro afffinities with breast and prostate cancer cells, Applied Organometallic Chemistry, 34 (2020) e5616.

[204] D.L. Thorek, D. Ulmert, N.-F.M. Diop, M.E. Lupu, M.G. Doran, R. Huang, D.S. Abou, S.M. Larson, J. Grimm, Non-invasive mapping of deep-tissue lymph nodes in live animals using a multimodal PET/MRI nanoparticle, Nature communications, 5 (2014) 1-9.

[205] E. Boros, A.M. Bowen, L. Josephson, N. Vasdev, J.P. Holland, Chelate-free metal ion binding and heat-induced radiolabeling of iron oxide nanoparticles, Chemical science, 6 (2015) 225-236.

[206] D.S. Abou, D.L.J. Thorek, N.N. Ramos, M.W.H. Pinkse, H.T. Wolterbeek, S.D. Carlin, B.J. Beattie, J.S. Lewis, 89Zr-Labeled Paramagnetic Octreotide-Liposomes for PET-MR Imaging of Cancer, Pharmaceutical Research, 30 (2013) 878-888.

[207] E.J. Keliher, J. Yoo, M. Nahrendorf, J.S. Lewis, B. Marinelli, A. Newton, M.J. Pittet, R. Weissleder, 89Zr-labeled dextran nanoparticles allow in vivo macrophage imaging, Bioconjugate chemistry, 22 (2011) 2383-2389.

[208] M.D. Majmudar, J. Yoo, E.J. Keliher, J.J. Truelove, Y. Iwamoto, B. Sena, P. Dutta, A. Borodovsky, K. Fitzgerald, M.F. Di Carli, Polymeric nanoparticle PET/MR imaging allows macrophage detection in atherosclerotic plaques, Circulation research, 112 (2013) 755-761.

[209] C. Pérez-Medina, J. Tang, D. Abdel-Atti, B. Hogstad, M. Merad, E.A. Fisher, Z.A. Fayad, J.S. Lewis, W.J. Mulder, T. Reiner, PET imaging of tumor-associated macrophages with 89Zr-labeled high-density lipoprotein nanoparticles, Journal of nuclear medicine, 56 (2015) 1272-1277.

[210] L. Cheng, A. Kamkaew, S. Shen, H.F. Valdovinos, H. Sun, R. Hernandez, S. Goel, T. Liu, C.R. Thompson, T.E. Barnhart, Facile preparation of multifunctional WS2/WOx nanodots for chelator-free 89Zr-labeling and in vivo PET imaging, Small, 12 (2016) 5750-5758.

[211] L. Karmani, D. Labar, V. Valembois, V. Bouchat, P.G. Nagaswaran, A. Bol, J. Gillart, P. Levêque, C. Bouzin, D. Bonifazi, Antibody-functionalized nanoparticles for imaging cancer: influence of conjugation to gold nanoparticles on the biodistribution of 89Zr-labeled cetuximab in mice, Contrast media & molecular imaging, 8 (2013) 402-408.

[212] L. Karmani, V. Bouchat, C. Bouzin, P. Levêque, D. Labar, A. Bol, G. Deumer, R. Marega, D. Bonifazi, V. Haufroid, 89Zr-labeled anti-endoglin antibody-targeted gold nanoparticles for imaging cancer: implications for future cancer therapy, Nanomedicine, 9 (2014) 1923-1937.

[213] Y. Zhan, E.B. Ehlerding, S. Shi, S.A. Graves, S. Goel, J.W. Engle, J. Liang, W. Cai, Intrinsically zirconium-89-labeled manganese oxide nanoparticles for in vivo dual-modality positron emission tomography and magnetic resonance imaging, Journal of biomedical nanotechnology, 14 (2018) 900-909.

[214] M.R.A. Abdollah, T.J. Carter, C. Jones, T.L. Kalber, V. Rajkumar, B. Tolner, C. Gruettner, M. Zaw-Thin, J. Baguña Torres, M. Ellis, M. Robson, R.B. Pedley, P. Mulholland, R. T. M. de Rosales, K.A. Chester, Fucoidan Prolongs the Circulation Time of Dextran-Coated Iron Oxide Nanoparticles, ACS Nano, 12 (2018) 1156-1169.

[215] R. Weissleder, M. Nahrendorf, M.J. Pittet, Imaging macrophages with nanoparticles, Nature materials, 13 (2014) 125-138.

[216] B. Gibbens-Bandala, E. Morales-Avila, G. Ferro-Flores, C. Santos-Cuevas, L. Melendez-Alafort, M. Trujillo-Nolasco, B. Ocampo-Garcia, Lu-177-Bombesin-PLGA (paclitaxel): A targeted controlled-release nanomedicine for bimodal therapy of breast cancer, Mater. Sci. Eng. C-Mater. Biol. Appl., 105 (2019).

[217] K.H. Zheng, J. Kroon, J. Schoormans, O. Gurney-Champion, S. Meijer, S. Gisbertz, M. Hulshof, D. Vugts, G.A. van Dongen, B. Coolen, 89Zr-labeled High-Density Lipoprotein Nanoparticle PET imaging reveals tumor uptake in patients with esophageal cancer, Journal of Nuclear Medicine, (2022).

[218] A. Bansal, M.K. Pandey, Y.E. Demirhan, J.J. Nesbitt, R.J. Crespo-Diaz, A. Terzic, A. Behfar, T.R. DeGrado, Novel Zr-89 cell labeling approach for PET-based cell trafficking studies, EJNMMI Res., 5 (2015) 11.

[219] F.Q. Shao, Y. Long, H. Ji, D.W. Jiang, P. Lei, X.L. Lan, Radionuclide-based molecular imaging allows CAR-T cellular visualization and therapeutic monitoring, Theranostics, 11 (2021) 6800-6817.

[220] C. Ashmore-Harris, M. Iafrate, A. Saleem, G.O. Fruhwirth, Non-invasive Reporter Gene Imaging of Cell Therapies, including T Cells and Stem Cells, Mol. Ther., 28 (2020) 1392-1416.

[221] P. Kathirgamanathan, S. Surendrakumar, J. Antipan-Lara, S. Ravichandran, V.R. Reddy, S. Ganeshamurugan, M. Kumaraverl, V. Arkley, A.J. Blake, D. Bailey, Discovery of two new phases of zirconium tetrakis(8-hydroxyquinolinolate): synthesis, crystal structure and their electron transporting characteristics in organic light emitting diodes (OLEDs), Journal of Materials Chemistry, 21 (2011) 1762-1771.

[222] P. Charoenphun, L.K. Meszaros, K. Chuamsaamarkkee, E. Sharif-Paghaleh, J.R. Ballinger, T.J. Ferris, M.J. Went, G.E.D. Mullen, P.J. Blower, Zr-89 Oxinate(4) for long-term in vivo cell tracking by positron emission tomography, Eur. J. Nucl. Med. Mol. Imaging, 42 (2015) 278-287.

[223] T.J. Ferris, P. Charoenphun, L.K. Meszaros, G.E.D. Mullen, P.J. Blower, M.J. Went, Synthesis and characterisation of zirconium complexes for cell tracking with Zr-89 by positron emission tomography, Dalton Transactions, 43 (2014) 14851-14857.

[224] N. Sato, H.T. Wu, K.O. Asiedu, L.P. Szajek, G.L. Griffiths, P.L. Choyke, Zr-89-Oxine Complex PET Cell Imaging in Monitoring Cell-based Therapies, Radiology, 275 (2015) 490-500.

[225] F. Man, L. Lim, A. Volpe, A. Gabizon, H. Shmeeda, B. Draper, A.C. Parente-Pereira, J. Maher, P.J. Blower, G.O. Fruhwirth, R.T.M. de Rosales, In Vivo PET Tracking of Zr-89-Labeled V gamma 9V delta 2 T Cells to Mouse Xenograft Breast Tumors Activated with Liposomal Alendronate, Mol. Ther., 27 (2019) 219-229.

[226] N. Sato, K. Stringaris, J.K. Davidson-Moncada, R. Reger, S.S. Adler, C. Dunbar, P.L. Choyke, R.W. Childs, In Vivo Tracking of Adoptively Transferred Natural Killer Cells in Rhesus Macaques Using (89)Zirconium-Oxine Cell Labeling and PET Imaging, Clin. Cancer Res., 26 (2020) 2573-2581.

[227] I. Friberger, E. Jussing, J.M. Han, J. Goos, J. Siikanen, H. Kaipe, M. Lambert, R.A. Harris, E. Samen, M. Carlsten, S. Holmin, T.A. Tran, Optimisation of the Synthesis and Cell Labelling Conditions for Zr-89 Zr-oxine and Zr-89 Zr-DFO-NCS: a Direct In Vitro Comparison in Cell Types with Distinct Therapeutic Applications, Mol. Imaging. Biol., 23 (2021) 952-962.

[228] L.M. Lechermann, R. Manavaki, B. Attili, D. Lau, L.B. Jarvis, T.D. Fryer, N. Bird, L. Aloj, N. Patel, B. Basu, M. Cleveland, F.I. Aigbirhio, J.L. Jones, F.A. Gallagher, Detection limit of Zr-89-labeled T cells for cellular tracking: an in vitro imaging approach using clinical PET/CT and PET/MRI, EJNMMI Res., 10 (2020) 12.

[229] T.W. Nobashi, A.T. Mayer, Z.Y. Xiao, C.T. Chan, A.M. Chaney, M.L. James, S.S. Gambhir, Whole-body PET Imaging of T-cell Response to Glioblastoma, Clin. Cancer Res., 27 (2021) 6445-6456.

[230] M.R. Weist, R. Starr, B. Aguilar, J. Chea, J.K. Miles, E. Poku, E. Gerdts, X. Yang, S.J. Priceman, S.J. Forman, D. Colcher, C.E. Brown, J.E. Shively, PET of Adoptively Transferred Chimeric Antigen Receptor T Cells with Zr-89-Oxine, J. Nucl. Med., 59 (2018) 1531-1537.

[231] U. Greenbaum, E.I. Dumbrava, A.B. Biter, C.L. Haymaker, D.S. Hong, Engineered T-cell Receptor T Cells for Cancer Immunotherapy, Cancer Immunol. Res., 9 (2021) 1252-1261.

[232] N.S.S. Maria, L.A. Khawli, V. Pachipulusu, S.W. Lin, L. Zheng, D. Cohrs, X.D. Liu, P.S. Hu, A.L. Epstein, R.E. Jacobs, Spatio-temporal biodistribution of Zr-89-oxine labeled huLym-1-A-BB3z-CAR T-cells by PET imaging in a preclinical tumor model, Sci Rep, 11 (2021) 13.

[233] Q. Wu, Y. Wang, X.Y. Wang, N.X. Liang, J.J. Liu, D.H. Pan, Y.P. Xu, L.Z. Wang, J.J. Yan, G.J. Wang, L.Y. Miao, M. Yang, Pharmacokinetic and pharmacodynamic studies of CD19 CAR T cell in human leukaemic xenograft models with dual-modality imaging, J. Cell. Mol. Med., 25 (2021) 7451-7461.

[234] F. Man, A.A. Khan, A. Carrascal-Minino, P.J. Blower, R.T.M. de Rosales, A kit formulation for the preparation of Zr-89 Zr(oxinate)(4) for PET cell tracking: White blood cell labelling and comparison with In-111 In(oxinate)(3), Nucl. Med. Biol., 90-91 (2020) 31-40.

[235] A.V.F. Massicano, J.L. Bartels, C.D. Jeffers, B.K. Crenshaw, H. Houson, C. Mueller, J.W. Younger, P. Knapp, J.E. McConathy, S.E. Lapi, Production of Zr-89 Oxinate(4) and cell radiolabeling for human use, J. Label. Compd. Radiopharm., 64 (2021) 209-216.

[236] S.H. Lee, H. Soh, J.H. Chung, E.H. Cho, S.J. Lee, J.M. Ju, J.H. Sheen, H. Kim, S.J. Oh, S.J. Lee, J. Chung, K. Choi, S.Y. Kim, J.S. Ryu, Feasibility of real-time in vivo Zr-89-DFO-labeled CAR T-cell trafficking using PET imaging, PLoS One, 15 (2020) 21.

[237] F. Simonetta, I.S. Alam, J.K. Lohmeyer, B. Sahaf, Z. Good, W.Y. Chen, Z.Y. Xiao, T. Hirai, L. Scheller, P. Engels, O. Vermesh, E. Robinson, T. Haywood, A. Sathirachinda, J. Baker, M.B. Malipatlolla, L.M. Schultz, J.Y. Spiegel, J.T. Lee, D.B. Miklos, C.L. Mackall, S.S. Gambhir, R.S. Negrin, Molecular Imaging of Chimeric Antigen Receptor T Cells by ICOS-ImmunoPET, Clin. Cancer Res., 27 (2021) 1058-1068.

[238] S. Mall, N. Yusufi, R. Wagner, R. Klar, H. Bianchi, K. Steiger, M. Straub, S. Audehm, I. Laitinen, M. Aichler, C. Peschel, S. Ziegler, M. Mustafa, M. Schwaiger, C. D'Alessandria, A.M. Krackhardt, Immuno-PET Imaging of Engineered Human T Cells in Tumors, Cancer Res., 76 (2016) 4113-4123.

[239] N. Yusufi, S. Mall, H.D. Bianchi, K. Steiger, S. Reder, R. Klar, S. Audehm, M. Mustafa, S. Nekolla, C. Peschel, M. Schwaiger, A.M. Krackhardt, C. D' Alessandria, In-depth Characterization of a TCR-specific Tracer for Sensitive Detection of Tumor-directed Transgenic T Cells by Immuno-PET, Theranostics, 7 (2017) 2402-2416.